Extension of the FVM Method to Subsonic Speeds

Janine Versteegh

A dissertation submitted to the Faculty of Engineering and the Built Environment, University of the Witwatersrand, Johannesburg, in fulfilment of the requirements for the degree of Master of Science in Engineering.

Johannesburg, June 2015

Declaration

I declare that this dissertation is my own, unaided work, except where otherwise acknowledged. It is being submitted for the degree of Master of Science in Engineering at the University of the Witwatersrand, Johannesburg. It has not been submitted before for any degree or examination at any other university.

Signed this ____ day of _____ 20__

_____

Janine Versteegh

Acknowledgements

Firstly I would like to thank my supervisors Sean Tuling and Laurent Dala for all their guidance and sternness that helped me persevere.

I would like to thank the CSIR, in particular Mauro Morelli, Kaven Naidoo and Gen. Des Barker for the funding and provision of resources required to complete this MSc. as well as their kind words of encouragement when I needed it. Thank you to Robert Mokwebo and Cannon Mkhwanazi for all their assistance during the wind tunnel testing.

To Bhavya for her assistance in submitting the dissertation and to the rest of my CSIR colleagues, family and friends, for their support throughout the course of this project.

Finally to Stefan, for his endless support, patience and understanding.

Abstract

An engineering level method, the free vortex model (FVM) method, which was developed for supersonic flow has been extended to subsonic incompressible Mach numbers. The method was applied to predict lee side flow features for a tangent ogive missile with very low aspect ratio wings in the '+' orientation. Simulations were carried out for three different span to body diameter ratios, namely 1.25, 1.50 and 1.75. Prediction results were validated by comparing aerodynamic loads and vortex positions to validated CFD data as well as another established engineering method namely the discrete vortex model (DVM) method. The normal force was well predicted while the centre-of-pressure position predictions were reasonable. The vortex positions were not predicted with the acceptable level of accuracy and is therefore a limitation of the method at incompressible speeds. It was shown that the FVM method is less suitable for span to body diameter ratios above 1.25 for which the DVM method is more suitable.

Published Work

Aspects of this dissertation have been published in the following conference references:

1. Versteegh, J., Tuling, S., Dala, L. "The Applicability of CFD for Simulating Flows Over Tangent Ogive Circular Slender Bodies at Incompressible Speeds." *Proceedings of the International Aerospace Symposium of South Africa,* September 2013, Somerset West.
2. Versteegh, J., "Lee-Side Floe Simulations of Cruciform Wing-Body Configurations at Incompressible Mach Numbers." *Proceedings of the 29th Congress of the International Council of the Aeronautical Sciences,* 2014, St. Petersburg, Russia.

Nomenclature

AR	Aspect ratio
a	Body radius (m)
c	Speed of sound (m/s)
c_{d_c}	Section drag coefficient
C_{CL}	Centroid of the planform area coefficient
C_D	Drag coefficient
C_{Dc}	Crossflow drag coefficient
C_L	Lift coefficient
$\left(C_{L_\alpha}\right)_W$	Lift-curve slope of the wing at zero angle of attack
C_m	Pitching moment coefficient about the nose
C_N	Normal force coefficient
$C_{N_{B_{forebody}}}$	Normal force coefficient due to forebody
$C_{N_{B_{aftbody}}}$	Normal force coefficient due to aftbody
$C_{N_{B+W}}$	Normal force coefficient due to wing-body section
C_p	Loss in nondimensional maximum mainstream dynamic head
C_{VL}	Volume coefficient
D	Body diameter (m)
f	Fineness ratio, l/D_{max}
F	Force (N)
k_B	Body carryover factor for wing deflection

k_W	Wing deflection factor
$K_{B(W)}$	Ratio of body lift to wing alone lift
K_C	Factor relating the lift of the wing alone and wing-body combination
K_n	Ratio of nose lift to wing alone lift
$K_{W(B)}$	Ratio of wing lift (in the presence of body) to wing alone lift
K_ϕ	Sideslip interference factor
l_f	Forebody length (m)
l	Total body length (m)
L	Lift (N)
L_C	Lift of wing-body combination (N)
L_W	Lift of wing alone (N)
M	Mach number
q	Dynamic pressure (Pa)
r_o	Circle radius in the ν–plane
Re	Reynolds number
Re_D	Reynolds number based on body diameter
s	Span (m)
s_m	Semi-span (m)
S	Reference area (m^2)
S_b	Base area (m^2)
S_p	Planform area (m^2)
V	Velocity (m/s)

x	Distance in x-direction (m)
x_m	Distance from the nose tip to the moment reference centre (m)
x_p	Distance from the nose tip to the centroid of the planform area (m)
X_{C_p}	Centre-of-pressure position (calibers)
y	Distance in y-direction (m)
z	Distance in z-direction (m)

Greek Symbols

α	Angle of attack (degrees/°)
α_c	Angle between the body axis and the wind velocity vector
α_{eq}	Equivalent angle of attack (degrees/°)
$\left(\Delta\alpha_{eq}\right)_v$	Induced change in angle due to vortex interaction
$\Delta\alpha_V$	Change in local upwash due to the vortex field
β	Sideslip angle (degrees/°)
δ	Wing deflection angle (degrees/°)
γ	Ratio of specific heats
Γ	Vortex strength
η	Crosflow proportionality factor
λ	Taper ratio
Λ	Leading edge sweep angle (degrees/°)
ν	Circle complex crossflow plane, $\tau + i\lambda$

ν_r	Complex distance between the vortex and its image vortex
ρ	Density (kg/m^3)
σ	Physical complex crossflow plane, $y + iz$
ϕ	Velocity potential
ϕ_x	Roll angle

Subscripts

B	Relating to the body
n	Relating to the nose
N	Normal to surface
t	Relating to time
T	Relating to the tail
W	Relating to the wing
x	Relating to the x-direction
y	Relating to the y-direction
z	Relating to the z-direction
∞	Relating to free stream

Contents

List of Figures

List of Tables

1. Introduction

Often in practice a given set of specifications should be met when designing a missile. It is then essential for an engineer to be able to predict the outcome of a design to a certain level of accuracy before further study. Therefore, the prediction of flow around missiles of varying types has extensively been studied since the early 1930's. The large variety of missile configurations has developed a need for prediction methods that are widely applicable to different geometries as well as flow regimes.

The method relevant to this study is the Free Vortex Model (FVM) method developed by Tuling [1] [2] in 2013. The FVM method was developed to predict the centre-of-pressure, normal force and vortex positions of a slender body with low aspect ratio wings. The method was restricted to body-wing combinations in the "+" orientation and was previously applied to the supersonic flow regime. The extension of the FVM method to subsonic flow is the topic of this study as will be described in the subsequent sections.

The FVM method is based in the two-dimensional (2-D) slender body theory (SBT) [1], which is known to be an incompressible formulation [3]. The successful extension of the FVM method to subsonic flow for configurations with very low aspect ratio wings (strakes), will increase the preliminary design capabilities, which are essential in the missile design phase. The application to incompressible flow, which is of particular interest in this study, will allow for the assessment of the base theory from which the method derived. This will provide a platform for the extension of the method to larger subsonic to transonic speeds, as the limitations of the theoretical

assumptions, inherent in SBT method will have been assessed. It was recommended [1] that the applicability of the FVM method to subsonic Mach numbers as well as non-zero roll angles be assessed.

Most engineering level codes have been developed using largely slender body theory and often these codes involve empirical data. Some codes require initial values for certain flow aspects, such as the crossflow drag coefficient or initial vortex positions and strengths which are obtained from experimental data, in order to solve a series of partial differential equations (PDE's). A few examples of existing engineering codes are Missile Datcom [4] [5], MISSILE I, II and III [6] [7], MISSILE (ONERA) [8], ESDU [9] [10] [11], NSWC & APC [12] [13], AERODYN [14] [15] and NASA W-B-T [16]. The advantages of using these engineering codes include low computational cost for reasonable accuracy (error below 20%). However the licenses for these codes are only available to a select amount of countries outside of the USA. Thus it is beneficial to continue developing "in-house" semi-empirical methods that may be applied using computing languages (such as Matlab, C++ etc.

Of particular interest in predictive methods is the calculation of the influence of the wing-body section, which includes the loads due to vortex shedding. Primarily, two main methods of determining the influence of wing vortices have been used in the past. The first type of method determines the load component due to the wing vortex by modelling the vortex as a single concentrated vortex (SCV) [17]. The second method defines the wing vortex as multiple discrete vortices [18] [2] instead of a single rolled up vortex. The FVM method, which is investigated in this study, models the vortex as a SCV.

In this study a wing-body combination is considered with constant body diameter and wings of very low aspect ratio. The terms “very low aspect ratio wings” and “strakes” will be used interchangeably in this dissertation. Three configurations with varying span to body diameter ratios (s/D) are considered:

1. s/D = 1.25, AR = 0.011
2. s/D = 1.5, AR = 0.022
3. s/D = 1.75, AR = 0.033

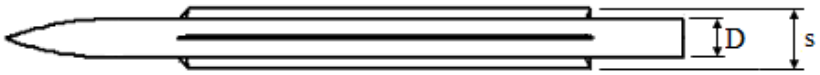

Figure 1: Configuration illustrating wing span (s) and body diameter (D)

All three wing configurations consist of a rectangular wing with a 45° leading edge sweep and straight trailing edge. The following research limitations also apply:

- Configurations with a tangent ogive nose of length 3D
- Configurations with a strake-body section of length 11.25D
- Four strakes arranged in the “+” orientation
- Leading edge sweep of 45°
- Flow regime is incompressible; $M \leq 0.3$
- Angle of attack range between 0° and 25°

It should be noted that “3D” refers to 3 times the body diameter, with the unit in calibers. In this dissertation low angles of attack (α) are considered to be $\alpha \leq 4°$, moderate angles of attack are then above 4° up to 15° and higher angles are

considered to be from 15° to 25°. Angles of attack above 25° will be referred to as high angles of attack.

1.1.Dissertation outline

In the subsequent chapters in this dissertation the available literature is reviewed followed by a summary of the research approach. The core engineering method, the FVM method, is then described in detail followed by a chapter on the DVM method. The reference data for validating the predicted FVM and DVM results is presented in the form of experimentally validated CFD simulations. This is followed by a detailed description of the engineering method results after which a chapter is dedicated to the discussion of result. Finally conclusions are drawn with some recommendations for further study.

2. Literature survey

The following section discusses important aerodynamic aspects of bodies alone, wings alone and wing-body combinations. The survey includes a discussion of available theories and prediction methods and their applicability to various missile configurations. Experimental observations by a number of authors are also considered.

2.1. Aerodynamics of Circular Slender Bodies

This part of the survey describes an overview of the theories developed for calculating the aerodynamic loads of bodies with a high fineness ratio (above 10 – also referred to as slender bodies) and no additional surfaces i.e. wings, strakes, canards etc. The fineness ratio of a body is defined as the ratio of the total body length to the maximum body diameter or

$$f = l/D_{max} \, . \tag{1}$$

2.1.1. Potential Theory

The velocity potential ϕ is a scalar function of position in time and is defined [19] as follows:

$$\phi = \phi(x, y, z, t), \tag{2}$$

$$\boldsymbol{V} = \boldsymbol{\nabla}\phi \tag{3}$$

where V is the velocity vector and ∇ is the gradient operator (note that bold letters represent vectors). In missile aerodynamics a partial differential equation (PDE) for

the velocity potential is solved and the velocities may be obtained by differentiation of ϕ. This PDE is called the potential equation [3]. Two axes systems are considered in the derivation of the potential equation, one fixed in the missile and fluid respectively (Figure 2).

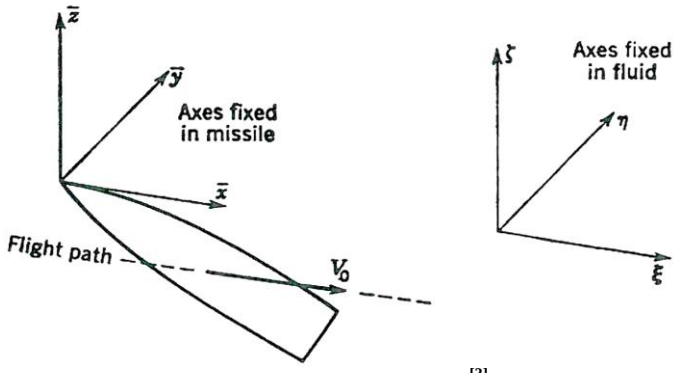

Figure 2: Missile axes system [3]

If the missile is stationary with the fluid moving at velocity V_∞, then the full nonlinear equation takes the following shape:

$$\left[c_\infty{}^2 + \frac{\gamma-1}{2}V_\infty{}^2 + (\gamma-1)\left(\phi_t + \frac{\phi_{\bar{x}}{}^2 + \phi_{\bar{y}}{}^2 + \phi_{\bar{z}}{}^2}{2}\right)\right]\left(\phi_{\bar{x}\bar{x}} + \phi_{\bar{y}\bar{y}} + \phi_{\bar{z}\bar{z}}\right)$$
$$= \phi_{tt} + \left(\phi_{\bar{x}}{}^2\phi_{\bar{x}\bar{x}} + \phi_{\bar{y}}{}^2\phi_{\bar{y}\bar{y}} + \phi_{\bar{z}}{}^2\phi_{\bar{z}\bar{z}}\right)$$
$$+ 2\left(\phi_{\bar{x}}\phi_{\bar{y}}\phi_{\bar{x}\bar{y}} + \phi_{\bar{x}}\phi_{\bar{z}}\phi_{\bar{x}\bar{z}} + \phi_{\bar{y}}\phi_{\bar{z}}\phi_{\bar{y}\bar{z}}\right)$$
$$+ 2\left(\phi_{\bar{x}}\phi_{\bar{x}t} + \phi_{\bar{y}}\phi_{\bar{y}t} + \phi_{\bar{z}}\phi_{\bar{z}t}\right) \qquad (4)$$

where c_∞ is the free stream speed of sound and γ is the ratio of specific heats. When Equation (4) is linearized all second order terms are reduced to first order or less which results in the condensed equation

$$\left(c_\infty{}^2 - \frac{\gamma-1}{2}V_\infty\right)\nabla^2\phi = \phi_{tt} + V_\infty{}^2\phi_{\bar{x}\bar{x}} + 2V_\infty\phi_{\bar{x}t}\,. \qquad (5)$$

In terms of free stream Mach number [20]

$$\phi_{\bar{x}\bar{x}}\left(1-{M_\infty}^2\right)+\phi_{\bar{y}\bar{y}}+\phi_{\bar{z}\bar{z}}=\frac{1}{{c_\infty}^2}\phi_{tt}+2\frac{M_\infty}{c_\infty}\phi_{\bar{x}t}\,. \tag{6}$$

If the body is sufficiently slender ($L \gg D$) it may be assumed that changes in the x direction are small, reducing Equation (6) to a 2-D problem around a circle in the y-z-plane,

$$\frac{\partial^2\phi}{\partial y^2}+\frac{\partial^2\phi}{\partial z^2}=0\,. \tag{7}$$

2.1.2. Slender body theory

Reference [3] describes how inviscid slender body theory (SBT) is derived from linear potential theory, which results in the following formulas for the normal and side force on circular slender bodies:

$$\frac{F_y}{q_\infty}=0 \quad \text{and} \quad \frac{F_z}{q_\infty}=2\alpha S(x) \tag{8}$$

where q_∞ is the free stream dynamic pressure, F_y is the side force, F_z is the normal force, α is the angle of attack and S(x) is the circular cross-sectional area as a function of x. From Equation (8), with the base area as reference area, the lift coefficient may then be given as

$$C_L=\frac{l}{q_\infty S}=\frac{F_z}{q_\infty S_b}=2\alpha \tag{9}$$

where S_b is the base area. Thus, the lift-curve slope $\frac{\partial C_L}{\partial \alpha}$ for SBT is two based on the body's base area. One of the limitations of SBT is its applicability when viscous

effects are present in the flow, such as vortex shedding. SBT suggests that the pressure distribution is symmetric about the horizontal plane (see Figure 3). In Figure 4 this expected pressure recovery of SBT is compared to experimental data for a slender body at 20^o angle of attack, Mach number of 1.96 and at 7.6 calibres along the body. The experimental pressure distribution shows a decrease similar to that of SBT, but poor pressure recovery occurs near the 0^o point after which a near-constant pressure distribution is observed [3]. This was attributed [3] to the forming of a region of near-uniform pressure on the lee side of the body due to the boundary layer separation.

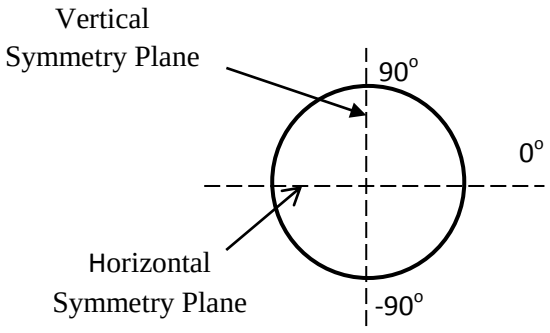

Figure 3: Description of the crossflow plane of a cylindrical slender body

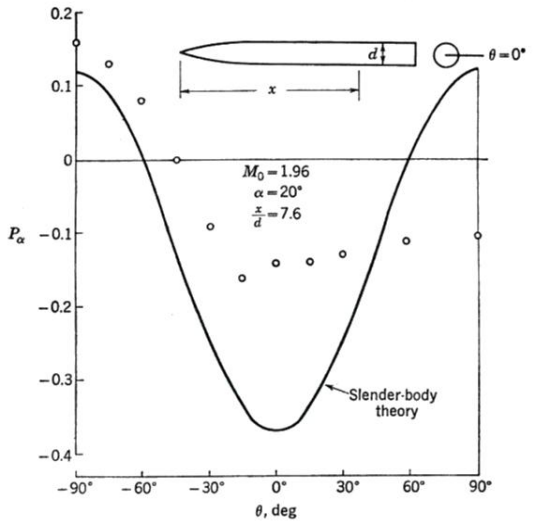

Figure 4: Pressure distribution around circular body as predicted by SBT [3]

2.1.3. Vortex Theory

The formation of vortices significantly influence the aerodynamics of missiles, therefore it is worth devoting some attention to vortex theory. Hans J. Lugt [21] provides three mechanisms for the generation of vortices in fluid motion. Briefly, they are as follows:

- Rotational flow is expected with when a fluid is in motion in an enclosed space. This is especially true for incompressible flow due to the conservation of mass.
- A vortex may form when fluid elements with vorticity accumulate at a point in the flow.
- Vortices may develop through instability in the flow field.

For a slender body of revolution at an angle of incidence below 90°, the flow around the body separates along a line toward the lee side of the body as show in Figure 5 (A). The rolled-up body vortices form due to vortex filaments that ascend after the boundary layer separation [3]. The position along the x-axis where vortices start forming (i.e. point of separation) is strongly influenced by the angle of attack and body geometry, as well as the Reynolds number and Mach number, which cause adverse pressure gradients in the boundary layer that drive separation [3].

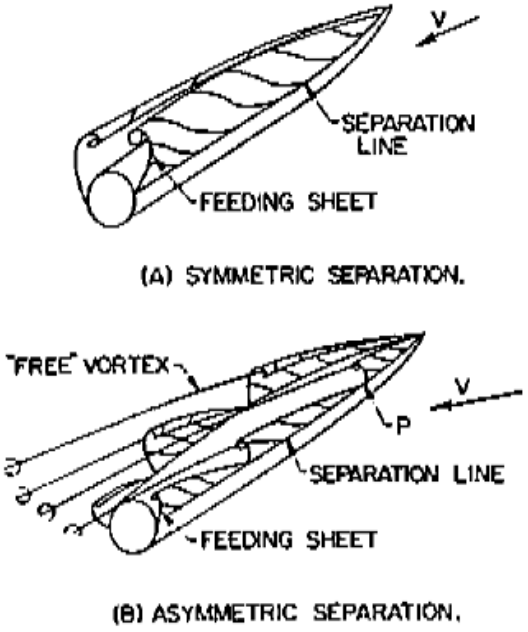

Figure 5: Vortex shedding from a body of revolution [18]

It is generally accepted [22] that, at low angles of attack, the flow remains attached along the length of the body. As the angle of attack increases, boundary layer separation occurs. At moderate angles of attack the vortices that form are symmetric, but at higher angles of attack asymmetric vortex shedding patterns occur [23]. Point P in Figure 5 (B) illustrates an arbitrary point at which the vortex sheet breaks away and forms a free vortex, after which a new vortex sheet forms immediately in its place.

The theory commonly known as crossflow theory was developed by Allen [22] in 1949 and was refined by Allen and Perkins [24] in 1951 to account for viscous effects such as vortex shedding when approximating the aerodynamic loads on slender bodies. Allen's crossflow theory has been applied to both subsonic and supersonic flow the assumption is applied that there is no Mach number dependence between $0 \leq M \leq 5$ at least.

If S is the reference area, then the lift coefficient according to the Allen and Perkins method may be written simply as

$$C_L = 2\left(\frac{S_b}{S}\right)\sin 2\alpha \cos\frac{\alpha}{2} + c_{d_c}\left(\frac{S_p}{S}\right)\sin^2\alpha\cos\alpha \tag{10}$$

where S_b is the base area, S_p.is the plan-form area (both in m^2) and c_{d_c} is the section drag coefficient. The method also includes approximations for the drag and moment coefficients:

$$C_D = C_{D_{\alpha=0}}\cos^3\alpha + \left(\frac{S_b}{S}\right)\sin 2\alpha \sin\frac{\alpha}{2} + c_{d_c}\left(\frac{S_p}{S}\right)\sin^3\alpha \tag{11}$$

and

$$C_m = \left(\frac{vol - S_b(l - x_m)}{SD}\right)\sin 2\alpha\cos\frac{\alpha}{2} + \left(\frac{S_p}{S}\right)\left(\frac{x_m - x_p}{D}\right)\sin^2\alpha \tag{12}$$

where l is the body length, x_m is the distance from the nose tip to the moment reference centre, x_p is the distance from the nose tip to the centroid of the planform area and *D* is the body diameter which may vary with axial distance.

The first term on the right hand side of Equations (10) to (12) is the contribution of potential theory and the second term represents the viscous effects. In reference [22], at low angles of attack ($\alpha < 4°$), it is suggested that Equations (10) to (12) may be simplified by the following approximations:

$$\cos\alpha \approx 1\,,$$

$$\sin\alpha \approx \alpha\,.$$

This leads to the following modified equations

$$C_L = 2\left(\frac{S_b}{S}\right)\alpha + c_{d_c}\left(\frac{S_p}{S}\right)\alpha^2 \,, \tag{13}$$

$$\Delta C_D = C_D - C_{D_{\alpha=0}} = \left(\frac{S_b}{S}\right)\alpha^2 + c_{d_c}\left(\frac{S_p}{S}\right)\alpha^3 \,, \tag{14}$$

$$C_m = \left(\frac{vol - S_b(l - x_m)}{SD}\right)\alpha + \left(\frac{S_p}{S}\right)\left(\frac{x_m - x_p}{D}\right)\alpha^2 \,. \tag{15}$$

An alternative method was proposed by reference [25] and was compared to Allan's Crossflow Theory (Equations (13) to (15)). The study concluded that crossflow theory shows good compatibility with experimental results, if slightly over-predicted, for various missile and airfoil models. However it could not be established which method would be more favourable.

Jorgensen [16] re-derived the Allen & Perkins theory and extended the method to angles of attack from zero to 180°. The formulations were derived semi-empirically and were also applied to bodies with wings/fins. The normal force and pitching moment coefficients from the Jorgensen formulation for angles of attack between 0° and 90°, with small angle approximation, can be expressed as

$$C_L = 2\left(\frac{S_b}{S}\right)\sin 2\alpha \cos\frac{\alpha}{2} + \eta c_{d_c}\left(\frac{S_p}{S}\right)\sin^2\alpha \,, \tag{16}$$

$$C_m = \left(\frac{vol - S_b(l - x_m)}{SD}\right)\sin 2\alpha \cos\frac{\alpha}{2} + \eta c_{d_c}\left(\frac{S_p}{S}\right)\left(\frac{x_m - x_p}{D}\right)\sin^2\alpha \,. \tag{17}$$

Equations (16) and (17) are very similar to the formulations of the previous method, with the addition of the crossflow drag proportionality factor η. Both c_{d_c} and η are taken from empirical data [16] [25].

Symmetric vortex shedding may also be estimated by what has been named the "lumped-vorticity approximation" [17]. The method described in reference [17] includes approximating the rolled up vortex sheet as a single concentrated vortex with the assumption of a fixed vortex feeding point (or separation point) on the body at 40° above the horizontal symmetry line. The vortex trajectories as well as aerodynamic loads predicted by the single concentrated vortex (SCV) method, as described in reference [17], were compared to available experimental data which showed reasonable correlation.

Marshall and Deffenbaugh [26] developed another method for solving the unsteady two-dimensional approach by modelling the wake as multiple discrete vortices. This method is sometimes referred to as the discrete vortex model (DVM) method [27] and was refined by Mendenhall [23] to include a "supersonic panel method". The method was also applied to a variety of body shapes in reference [18] with good correlation to experimental data.

2.1.4. Semi-empirical methods

In recent decades a number of semi-empirical methods have been derived for predicting flow over bodies of revolution.

A combination of potential theory and crossflow theory was proposed by Hopkins [25] to predict the pitching moment and forces on bodies of revolution at moderate angles of attack and low Mach numbers. The method utilizes an empirical trend to identify

which segments of the body potential theory may be applied to. The predictions were applied to body fineness ratios (f) between 4 and 12.5 and were compared to the method described by Allen [22] for 15 different bodies of revolution. The method of Hopkins was demonstrated to correlate to experimental data at least as well as that of Allen. Figure 6 shows the comparison of the lift coefficient for these two methods to potential theory as well as experimental data for two bodies.

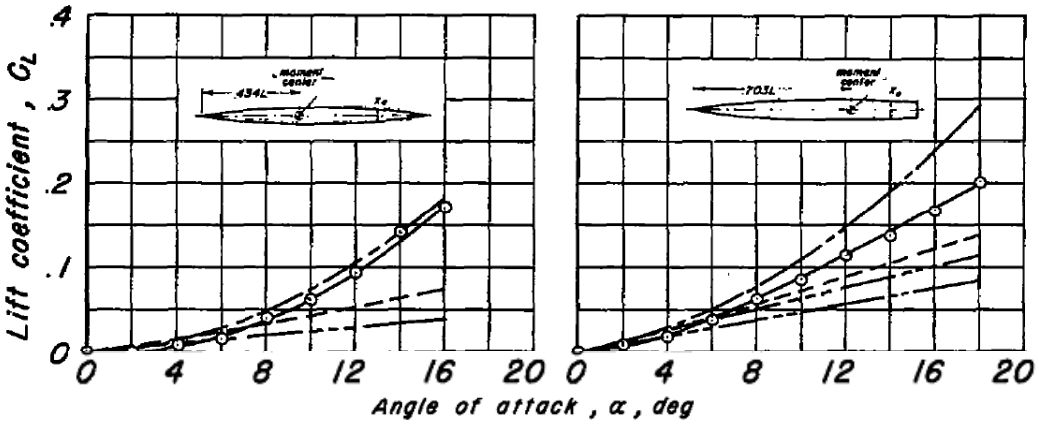

Figure 6: Lift coefficient determined by Hopkins' theory compared to Allen's crossflow theory [25]

Another method was published in the Engineering Sciences Data Unit (ESDU) [11] in 1983 to estimate the normal force and pitching moment of axisymmetric cylindrical bodies (without wings) for angles of attack up to 90°. The method was extended to Mach numbers below and equal to 1.2 in reference [9] as well as Mach numbers above 2.0 in reference [11]. Attention was also given to the effects of Reynolds number, Mach number and forebody blunting. The final modified equations [9] for $M \leq 1.2$ are listed below:

$$C_N = k_1 \sin 2\alpha \cos\frac{\alpha}{2} + \frac{C_{Dc}}{\pi}\left[4\frac{l}{D} - \frac{5}{6}\frac{l_f}{D}\right]\sin^2\alpha\,, \tag{18}$$

$$C_m = k_1(1 - C_{VL})\frac{l}{D}\sin 2\alpha \cos\frac{\alpha}{2} - \frac{C_{Dc}}{\pi}\frac{C_{CL}}{2}\frac{l}{D}\left[4\frac{l}{D} - \frac{5}{6}\frac{l_f}{D}\right]\sin^2\alpha \tag{19}$$

where C_{Dc} is the crossflow drag coefficient, C_m is the pitching moment coefficient about the nose, C_{VL} is the volume coefficient, C_{CL} is the centroid of the planform area coefficient and l_f is the forebody length. The factor k_1, which is applied to the potential term, is an empirical factor and is a function of Mach number. Again the applicability of this modified method is constrained to axisymmetric cylindrical bodies at certain conditions for two different forebody shapes, noted in Table 1.

Table 1: Constraints for the ESDU subsonic method [9].

Forebody shape	$\frac{l_f}{D}$	$\frac{l}{D}$	M_∞	Angle of attack
Tangent ogive	1.5 to 5	6 to 19.5	0.25 to 1.2	0° to 90°
Cone	1.9	10	0.5	

The following three factors may influence the accuracy of the EDSU subsonic method (i.e. Equations (18) and (19)):

1. The sensitivity of the normal force to surface conditions at the nose in the presence of asymmetric vortex flow.
2. Unsteady effects due to the presence of asymmetric vortex flow.
3. Variations in the body geometry

It was also stated that the accuracy of centre-of-pressure predictions x_{cp}/l falls within $\pm$ 0.08.

2.1.5. Experimental Observations

For the three-dimensional (3-D) cylindrical body the state of the boundary layer at separation depends on both the angle of attack and the Reynolds number, which is based on body diameter. There are three regimes typically found in experimental

testing and are defined by four transition mechanism boundaries. In addition to laminar and turbulent boundary layer separation, there is a third regime known as the "short bubble" regime [9] [11]. The short bubble is characterized by an initial laminar boundary layer separation after which turbulent re-attachment occurs, followed by final separation of the turbulent boundary layer.

The four transition mechanism boundaries are briefly described [9] with Equations (20) to (23) and a graphical representation in Figure 7.

1. Free shear-layer instability:

$$Re_D = \frac{\tan\alpha}{\cos\alpha\,(1 + 3.3\tan^2\alpha)}10^6\,. \tag{20}$$

2. Attachment-line instability:

$$Re_D = 1.1\frac{\tan\alpha}{\cos\alpha}10^6\,. \tag{21}$$

3. Crossflow instability:

$$Re_D = 0.145\frac{1 + 3.3\tan^2\alpha}{\sin\alpha}10^6\,. \tag{22}$$

4. Streamwise-flow instability:

$$Re_D = 4 \times 10^6\,. \tag{23}$$

In general, side forces and yawing moments may arise due to out-of-plane force distributions that result from asymmetric vortex flow. It was noted that side forces reduce in magnitude as Mach number increases. Reference [9] produced a graph (see Figure 8) of maximum side force versus crossflow Mach number, obtained from

various sets of data. If a body has a pointed nose, initial asymmetry generally occurs near the tip. This initial asymmetry is prevented by blunting the nose with a spherical diameter d as demonstrated in Figure 9.

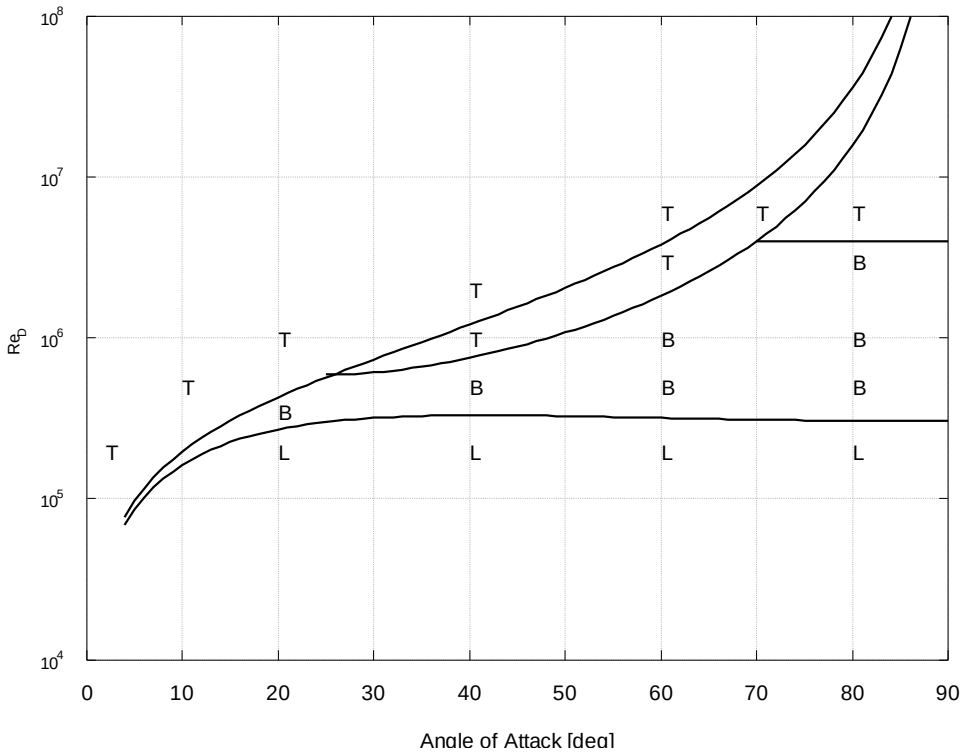

Figure 7: Experimental Boundary Layer Flow Regimes [9]: laminar (L), bubble (B) and turbulent (T).

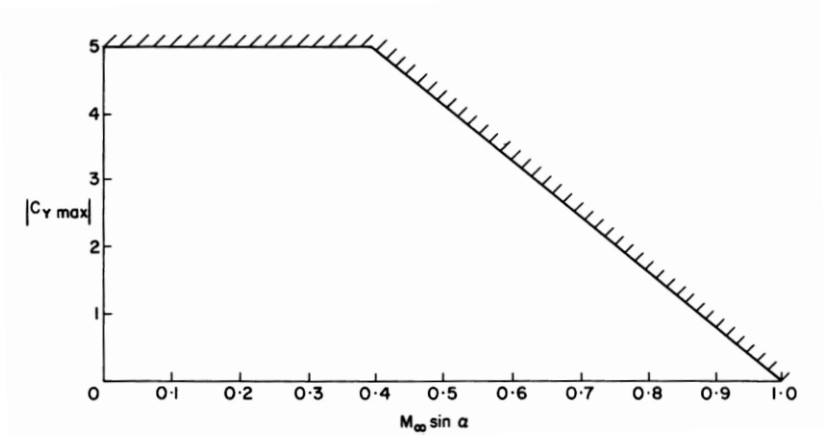

Figure 8: Variation of maximum side force with crossflow Mach number [9]

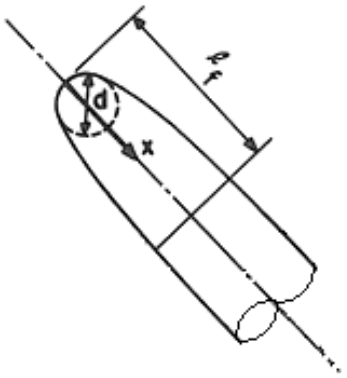

Figure 9: Graphical Illustration of Blunted Nose [9]

An experimental investigation [28] was conducted in order to determine the point at which the body vortices separate from the body. This was done by measuring the pressure distribution around the body in any crossflow plane and it was noted that the point of separation occurs at the point where a constant pitot pressure is maintained (also see graph on pressure recovery in Figure 4). The downwash due to the wake vortices were also investigated and expressions for the flow angles were derived using potential theory with the addition of two symmetrical vortices of equal strength. The paths and strengths of the body vortices could also be predicted quite accurately but requires knowledge on the normal force. The comparisons between the derived theoretical expressions and experimental data showed reasonable correlation at angles of attack below 20°.

2.2. Wing Alone Aerodynamics

The aerodynamics of very low aspect ratio wings (AR ≤0.1) are of particular interest in this study. Low aspect ratio wings (AR ≅ 1) have been extensively studied since the late 1930's [29] [30]. Some wing plan forms that have been studied include delta wings, rectangular wings, cropped delta wings, wing-strake combinations and trapezoidal wings [31] [32]. Some experimental observations are available on all the

noted wing types [31] [32] [33]. In reference [34] various theoretical prediction methods were applied to wings with rectangular and delta plan forms while focussing on aspect ratios below 3.

2.2.1. Experimental Observations

An examination of experimental data relating to delta wings of low AR will indicate a non-linear relationship between angle of attack and aerodynamic coefficients [34]. A typical example of such a lift-curve is shown in Figure 10.

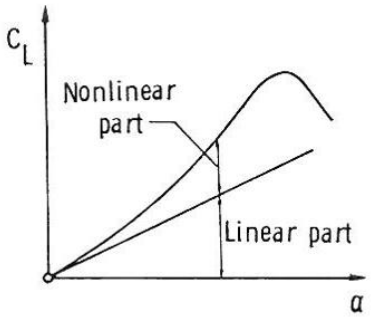

Figure 10: Lift curve of low aspect ratio delta wing [31]

At low angles of attack, the lee-side flow remains attached, but as the angle of attack increases, the flow separates from the leading edges forming lee-side vortices [31] (see Figure 11). There are two simple equations relating the free stream Mach number (M_∞), angle of attack (α) and leading edge sweep angle (Λ) to the angle of attack and Mach number normal to the leading edges (α_N and M_N respectively):

$$\alpha_N = \tan^{-1}\frac{\tan\alpha}{\cos\Lambda}, \tag{24}$$

$$M_N = M_\infty\sqrt{1-\cos^2\alpha\sin^2\Lambda}\,. \tag{25}$$

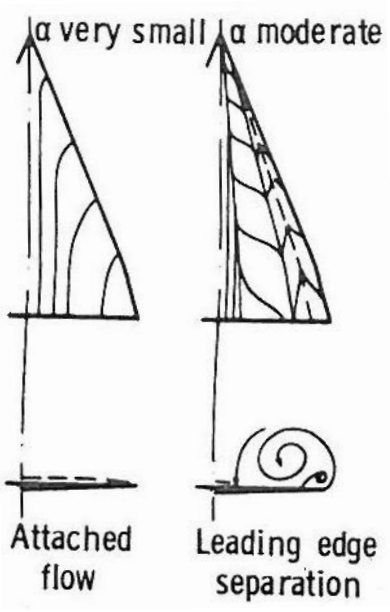

Figure 11: Lee-side flow features of a delta wing at subsonic speeds [31]

A phenomena known as "vortex breakdown" has been shown [31] [32] to occur at high angles of attack. At the vortex breakdown point, an abrupt expansion of the vortex cores above the wing occurs, decreasing the axial velocity downstream of this point. The AR (and thus leading edge sweep) of the delta wing influences the angle of attack at which vortex breakdown will occur and it was shown by Stahl [32] that the critical angle of attack at which breakdown is observed, decreases with decreasing leading edge sweep.

The effects of AR on the normal force coefficient (C_N) are shown in Figure 12. At supersonic speeds, C_N tends to increase with increasing AR [31]. At subsonic speeds the AR has a more complex effect on C_N due to the varying effect the AR has on vortex breakdown (or wing stall). The angle of attack at which vortex breakdown occurs, i.e. the peak of the C_N-α curve, increases with decreasing AR for $1.5 \leq \text{AR} \leq 4$ and decreases again for AR=1. Below angles of attack of approximately 15°, C_N tends to increase with increasing AR as with the supersonic data.

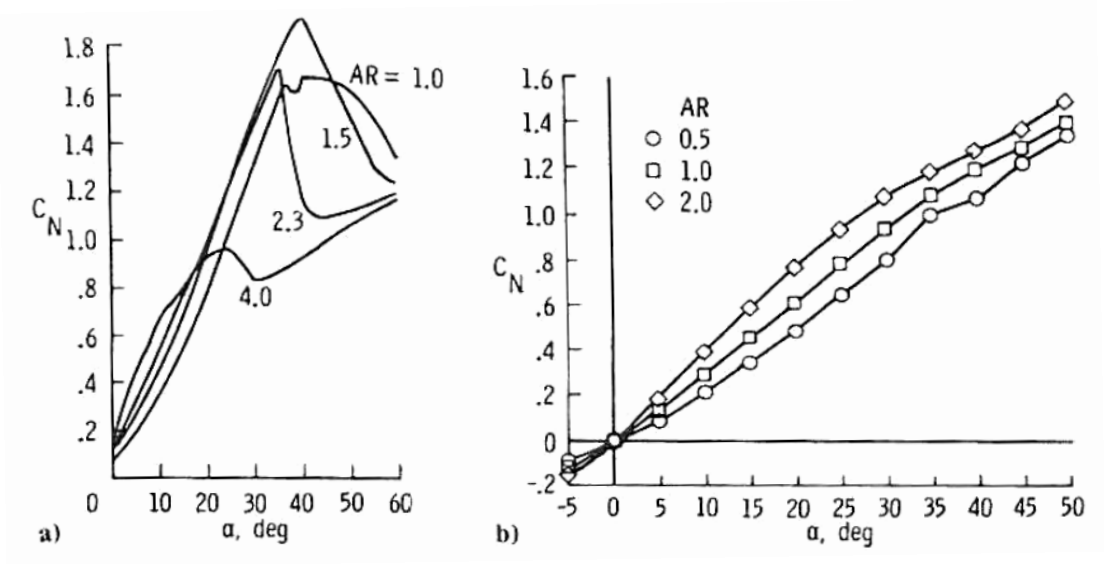

Figure 12: Effects of AR on normal force coefficient for (a) subsonic and (b) supersonic flow [31]

Low aspect ratio rectangular and trapezoidal wings are expected to have very similar flow fields as both planforms have separate leading and side edges [32] (as opposed to delta wings which have swept back leading edges). For thin wings with slightly rounded leading edges, a separation bubble was observed at the leading edge, which increases in size with increasing angle of incidence. The separation bubble can also be described as a vortex having a core that is parallel to the wing surface [31]. A short separation bubble for a given wing cross-section is demonstrated in Figure 13.

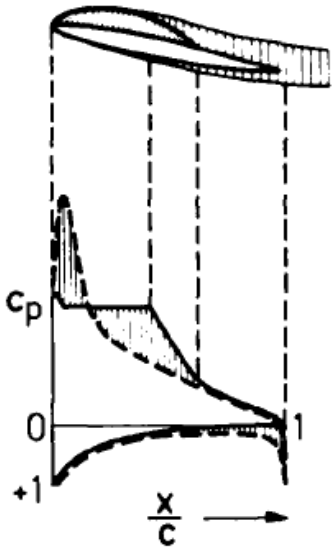

Figure 13: Short Bubble Region for Wing Profile [32]

For flat plate rectangular wings with sharp edges, the flow separates around the side edges. The separated flow forms a vortex sheet which rolls up into a vortex core [32]. The side edge vortices as well as the separation bubble and other flow features as interpreted from skin friction lines [35] are illustrated schematically in Figure 14. Similarly to the delta wing, C_N was shown [31] to increase with increasing AR at low speeds below angles of attack of approximately 15°. This is illustrated in Figure 15. The vortex breakdown point also tends to increase with decreasing AR up to AR=0.5. The vortex breakdown point is then at a slightly lower angle of attack at AR=0.35 and no vortex breakdown effect is observed at AR=0.134.

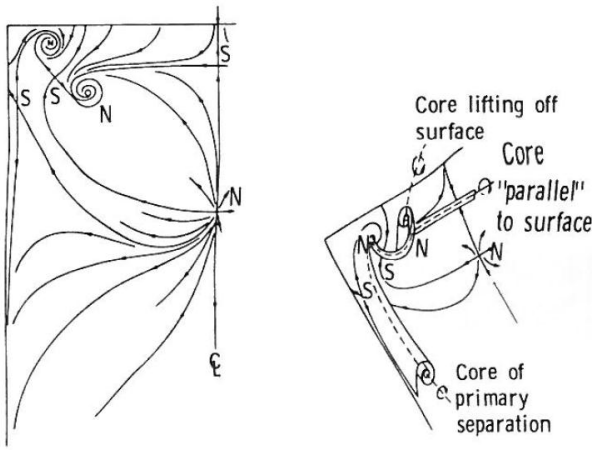

Figure 14: Interpretation of skin friction lines for a slender rectangular wing [35]

Clipped delta wings have also been used in various missile designs [31]. A C_N-α curve for wings with three different taper ratios (λ) are shown in Figure 16. If a rectangular wing (λ = 1) is modified so that the leading edges are swept back to a finite value, the C_N-α curve changes only moderately. If the sweep angle is increased, the flow field will begin to approach that of a delta wing as the side edges and their effects are reduced.

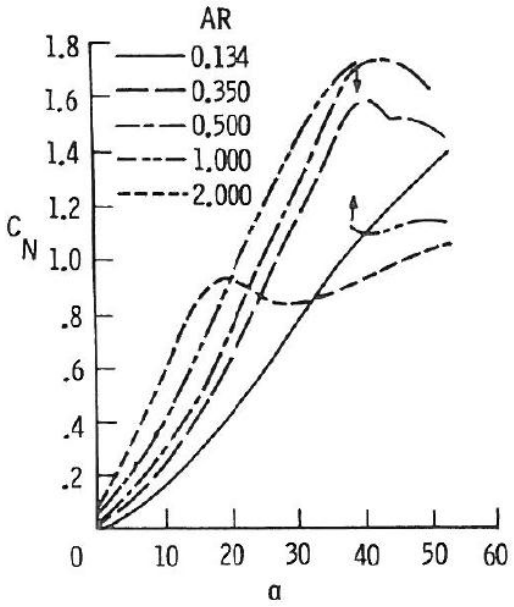

Figure 15: Effect of AR on the normal force coefficient for a rectangular wing at low speeds [31]

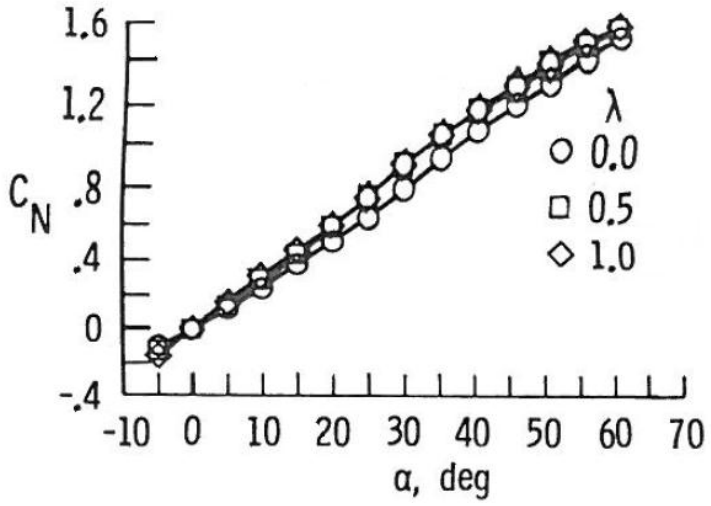

Figure 16: Effect of taper ratio on wing normal force coefficients for AR=1 and M_∞=2.16 [33]

As shown previously, vortex breakdown for wings at subsonic speeds causes significant loss of lift at high angles of attack. The vortex breakdown for swept back wings at large angles of attack can be delayed by adding small strakes in front of the wing [31] [32]. The strakes generally have slender delta wing planforms and have a total area that is approximately 10% that of the main wing [31] [32]. The strong leading edge vortices created by the strake increases the effective sweep of the main wing which stabilizes the leading edge separation of the main wing [31]. An example of the strake-wing combination and the effect on lift is shown in Figure 17.

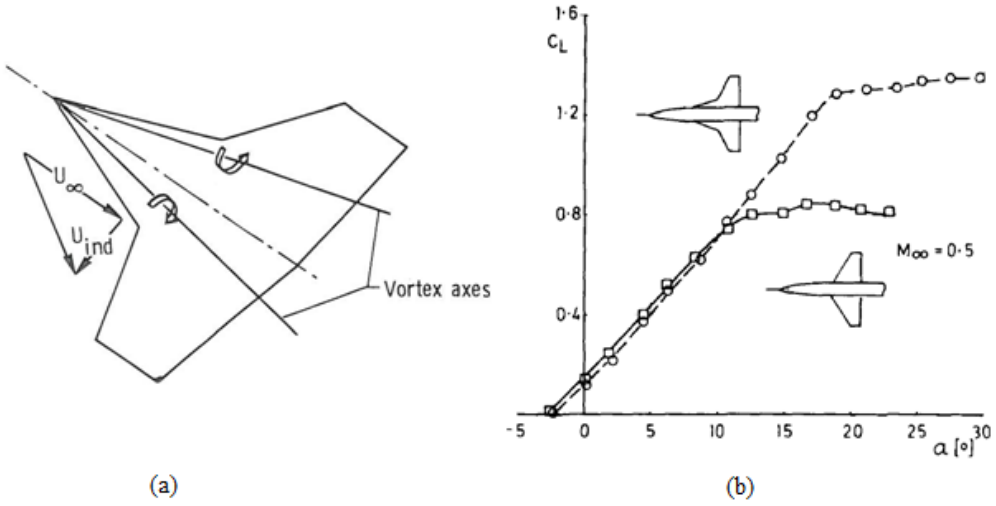

Figure 17: (a) Strake-wing planform with vortex structure [31] (b) Effect of strakes on wing-body lift at M_∞=0.5 [32]

2.2.2. Theoretical Methods

In 1946 a theory was proposed by Jones [29] to determine the lift of low aspect ratio wings for small angles of attack. The problem is approached utilising classic thin-airfoil theory [36] [37] as well as potential theory to calculate compressibility effects. Elliptical, triangular and rectangular airfoil shapes were considered. The formulas obtained by Jones were similar to those developed by Munk's theory [38] on airship hulls.

Flax and Lawrence [34] proposed that the problem of predicting the flow over low aspect ratio wings divides into two parts. Firstly, estimating the lifting-surface theory within reasonable accuracy and time and secondly, calculating the non-linear effects. In the past the non-linear effects have largely been determined by semi-empirical means. Crossflow theory, first proposed by Allen [22] for slender bodies, was believed to be the best basis for deriving semi-empirical methods [34] for estimating non-linear effects. In order to reduce computational time the lifting-surface theory is reduced to the classical lifting-line theory first developed by Prandtl.

2.3. Aerodynamics of wing-body combinations

2.3.1. Wing-body Interference

The effect of wing-body interference has been largely studied throughout the history of missile aerodynamics due to the subject's importance in the calculation of aerodynamic loads of wing-body combinations. It has been said [20] [39] that there are two categories of methods currently available for predicting wing-body characteristics; the first being theoretical methods that attempt to solve complicated boundary-value problems and the second being semi-empirical engineering methods with limited applicability. One theoretical method produced by reference [40] involves a complicated solution to the linearized cylindrical potential equation. An attempt to derive a method with high accuracy as well as wide applicability was made by Nielsen and Pitts [39]. The study was conducted at supersonic speeds and produced an extended theoretical method for determining the aerodynamic lift and centre-of-pressure position as a function of wing aspect ratio and effective chord-radius ratio (i.e. ratio of wing chord length over body radius).

The lift and centre-of-pressure prediction method developed by Pitts, Nielsen and Kaattari. [41] is based on slender body theory (SBT) and involves the theoretical estimation of wing-body interference factors at supersonic speeds. The lift of the wing alone and wing-body combination is represented as L_W and L_C respectively and are linearly related by the factor K_C,

$$L_C = K_C L_W \, . \tag{26}$$

K_C is defined as the sum of the following ratios:

- $K_{B(W)}$ – ratio of body lift (in the presence of wings) to wing alone lift
- $K_{W(B)}$ – ratio of wing lift (in the presence of body) to wing alone lift
- K_n – ratio of nose lift to wing alone lift

$$K_C = K_{B(W)} + K_{W(B)} + K_n \,. \tag{27}$$

By applying slender body theory SBT [3] [42] the values given to these ratios are

$$K_n = \frac{2\pi {a_n}^2}{S_W \left(C_{L_\alpha}\right)_W}, \tag{28}$$

$$K_{W(B)} = \frac{2}{\pi} \frac{\left\{\left(1 + \frac{a^4}{{s_m}^4}\right)\left[\frac{1}{2}\tan^{-1}\frac{1}{2}\left(\frac{s_m}{a} - \frac{a}{s_m}\right) + \frac{\pi}{4}\right] - \frac{a^2}{{s_m}^2}\left[\left(\frac{s_m}{a} - \frac{a}{s_m}\right) + 2\tan^{-1}\frac{a}{s_m}\right]\right\}}{\left(1 - \frac{a}{s_m}\right)^2}, \tag{29}$$

$$K_{B(W)} = \frac{\left(1 - \frac{a^2}{{s_m}^2}\right)^2 - \frac{2}{\pi}\left\{\left(1 + \frac{a^4}{{s_m}^4}\right)\left[\frac{1}{2}\tan^{-1}\frac{1}{2}\left(\frac{s_m}{a} - \frac{a}{s_m}\right) + \frac{\pi}{4}\right] - \frac{a^2}{{s_m}^2}\left[\left(\frac{s_m}{a} - \frac{a}{s_m}\right) + 2\tan^{-1}\frac{a}{s_m}\right]\right\}}{\left(1 - \frac{a}{s_m}\right)^2} \tag{30}$$

where S_W is the wing area, a is the body radius, a_n is the body radius at the nose shoulder, $\left(C_{L_\alpha}\right)_W$ is the lift-curve slope of the wing at zero angle of attack, and s_m is the maximum semi-span of the wing-body combination. The theoretical normal force coefficient C_N is then estimated as follows

$$C_N = C_{N_n} + C_{N_{W(B)}} + C_{N_{B(W)}}\,, \tag{31}$$

$$C_N = \left(K_n + K_{W(B)} + K_{B(W)}\right)\left(C_{N_\alpha}\right)_W \alpha \,. \tag{32}$$

If the wing-body combination produces more lift than the wing alone (i.e. the body produces positive lift interference) then $K_{W(B)}$>1. If $K_{B(W)}$<1, the body produces negative lift interference [43].This method has been applied to, and experimentally validated for, nearly 100 wing-body combinations and it was found that in most cases the lift was predicted to within $\pm$10% of experimental results. Modifications for finite and negative aftbodies were developed in references [44] [45] and [46].

In 1989, Nelson and Bossi [47] explored wing-body interference factors for supersonic missiles with elliptical cross-section fuselages. Changes in $K_{W(B)}$ as a function of span to body radius (s/a) were compared for different aspect ratios of delta-wings by solving Euler equations. The research showed that body (fuselage) has a positive effect on the wing lift for small s/a and the effect of the body becomes negligible for large s/a-values. An investigation by Est and Nelson [48] in 1995 included effects of Mach number, body shape and angle of attack on $K_{W(B)}$ and centre-of-pressure using an Euler code, ZEUS. Again the study was only applied to supersonic Mach numbers (between 2 and 4) and concluded that $K_{W(B)}$ predictions do not vary significantly with angle of attack below 5°, but show sensitivity to Mach number, wing leading-edge sweep angle and body shape.

2.3.2. Equivalent Angle of Attack Concept

The equivalent angle of attack (EAOA) method was derived in 1977 by reference [49] to computationally derive the aerodynamic characteristics of cruciform wing-body combinations. The method may be applied to Mach numbers ranging from

subsonic to supersonic speeds and angles of attack up to 20°. The EAOA method is based on the principal that the normal force coefficient of a wing/fin is the same as the normal force coefficient of the wing/fin alone, comprised of two of the same wings/fin connected symmetrically at the root chord, then the other force and moment coefficients are also alike. The equivalent angle of attack α_{eq} is then the angle of attack of the wing alone at which the above statement is true: if the body diameter is large compared to the wing span, the angle of attack experienced by the wing alone does not equal the body angle of attack, due to the disturbance introduced by the body to the flow field [50].

The wing-body interference factors derived from slender body theory are used to calculate α_{eq} along with small angle approximations and the assumption of linear superposition of the contributing factors to the lift coefficient. Additional work was done on the extension and application of the EAOA method in references [41] to [51]. The equivalent-angle-of-attack can be written as [47]

$$\alpha_{eq} = K_{W(B)}\alpha + \frac{4}{AR}K_{\phi}\alpha\beta \tag{33}$$

where β is the sideslip angle and K_{ϕ} is the sideslip interference factor. Thus the second term on the right-hand side represents effects from fin sideslip angle. The first term on the right-hand side of the equation represents the contribution due to body upwash.

If vortex interaction is considered a third term may be added to Equation (33), such that

$$\alpha_{eq} = K_{W(B)}\alpha + \frac{4}{AR}K_{\phi}\alpha\beta + \left(\Delta\alpha_{eq}\right)_{v} \tag{34}$$

where $\left(\Delta\alpha_{eq}\right)_{v}$ is the induced change in angle due to vortex interaction [43]. The component of normal force coefficient of the wing in the presence of the body $\left(C_{N_{W(B)}}\right)$ can be written as follows,

$$C_{N_{W(B)}} = \left.\frac{\partial C_{N_W}}{\partial\alpha}\right|_{\alpha=0} \alpha_{eq}\,. \tag{35}$$

If the wing is sufficiently aft of the nose and at small angles of attack, the cylindrical portion of the body will produce very little or no lift [50]. Therefore, lift is only generated due to the presence of the wing. By applying slender body theory (SBT), the normal force for the wing-body section may be calculated as

$$C_{N_{W(B)}} + C_{N_{B(W)}} = \frac{2\pi\alpha_c {s_m}^2}{S}\left(1 - \frac{a^2}{{s_m}^2}\right)^2 \tag{36}$$

where α_c is the angle between the body axis and the wind velocity vector. If only the wing alone is considered [20] [50] [52] Equation (36) reduces to

$$C_{N_W} = \frac{2\pi\alpha_c(s_m - a)^2}{S}\,. \tag{37}$$

Dividing Equation (36) by Equation (37) gives

$$\frac{C_{N_{W(B)}} + C_{N_{B(W)}}}{C_{N_W}} = \left(1 - \frac{a}{s_m}\right)^2 . \tag{38}$$

It was suggested by Morikawa [52] , Ward [53] and Nielsen and Kaattari [20] that the wing alone component be derived from linear theory or obtained from empirical data. This is called the *modified* SBT method. Equation (38) can also be rewritten [50] [52] in terms of the interference factors $K_{W(B)}$ and $K_{B(W)}$ as follows

$$K_{W(B)} + K_{B(W)} = \left(1 - \frac{a}{s_m}\right)^2 \tag{39}$$

where

$$K_{W(B)} = \frac{C_{N_{W(B)}}}{C_{N_W}};\ \ \alpha \neq 0, \delta = 0,$$

$$K_{B(W)} = \frac{C_{N_{B(W)}}}{C_{N_W}};\ \alpha \neq 0, \delta = 0.$$

The SBT formulations for the above interference factors are shown in Equations (28) to 30 and are plotted against the α/s_m ratio in Figure 18. The results can however be improved by replacing these values by computational, semi-empirical or experimental values.

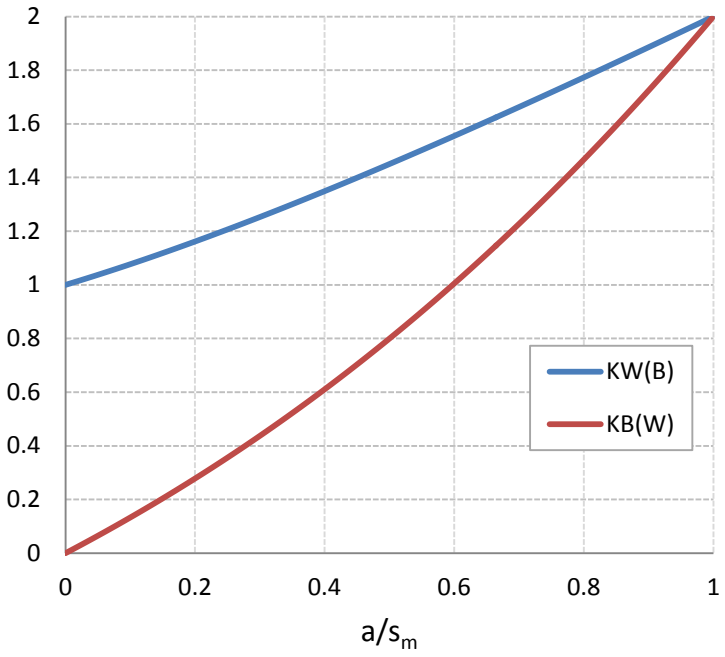

Figure 18: Slender Body Theory Wing-body Interference Factors

If a tail is present, the normal force acting on the tail section in the presence of the wing is given [50] as follows

$$C_{N_{T(W)}} = \left(1 + \frac{k_B}{k_W}\right) \Delta\alpha_V \left.\frac{\partial C_{N_T}}{\partial \alpha}\right|_{\alpha=0} \tag{40}$$

where k_B is the body carryover factor for wing deflection, k_W is the wing deflection factor and $\Delta\alpha_V$ is the change in local upwash due to the vortex field. The total normal force coefficient is then simply the sum of all the relevant components:

$$C_{N_{BWT}} = C_{N_B} + C_{N_{W(B)}} + C_{N_{B(W)}} + C_{N_{T(B)}} + C_{N_{B(T)}} + C_{N_{T(W)}} \,. \tag{41}$$

By applying the EAOA method Equation (41) may be written [50] as

$$C_{N_{BWT}} = C_{N_B} + \left[\left(K_{W(B)} + K_{B(W)}\right)\alpha_c + (k_W + k_B)\delta\right]_{wing} \left.\frac{\partial C_{N_W}}{\partial \alpha}\right|_{\alpha=0} + \left[\left(K_{W(B)} + K_{B(W)}\right)\alpha_c + (k_W + k_B)\delta + \left(1 + \frac{k_B}{k_W}\right)\Delta\alpha_V\right]_{tail} \left.\frac{\partial C_{N_T}}{\partial \alpha}\right|_{\alpha=0} \quad (42)$$

where δ is the wing deflection angle. The pitching moment coefficient can then be calculated using the centre-of-pressure estimate from references [3] and [42] together with the result from Equation (42). Extensions to the EAOA method includes effects of bank, supersonic Mach numbers and high angles of attack and are discussed extensively in reference [50].

2.3.3. Potential Methods

Three potential methods applicable to this study, namely the single concentrated vortex (SCV), discrete vortex model (DVM) and free vortex model (FVM) methods. As previously mentioned (Section 2.1.3), the SCV method models the rolled up vortex sheet as two single concentrated vortices. This constitutes a line vortex that is concentrated at the centre of gravity of the vorticity. The SCV method was first proposed by reference [17] for slender bodies of revolution, but may be extended to wing-body combinations [27]. For a case of leading edge separation on delta wings [54], the sharp edge is defined by the Kutta-condition in order to determine the strength and positions of the concentrated vortices. For bodies alone, a similar condition is defined such that the vortex feeding points are defined as stagnation points [17]. The

locations of these points were estimated by experimental observation to be approximately 40° above the horizontal symmetry line.

In the DVM method, the vortex sheet that separates from the strake side edge is represented by multiple discrete singularities (vortex filaments). The shed vortices are then modelled as free vortices which then move as Lagrangian fluid particles [27]. In order to define the shed vortex it is required to first determine its initial position in two orthogonal directions (generally in the y-z plane as shown in Figure 2, Section 2.1.1) as well as the strength of the vortex. The nature of the strake side edge is defined by the Joukowski-Kutta condition and the local velocity at the edge is determined from the velocity potential. The method for predicting the path of the discrete vortices is elucidated by references [27] and [55].

The predictive method that is relevant to this study is the FVM method and was recently developed by Tuling et al. [1] [2]. The method has been applied to the following conditions:

- Cruciform wing-body combination in "+" orientation
- Wings of very low aspect ratio (below 0.1) and taper ratio greater than 0.85
- Constant body diameter across wing-body section
- Wing span to body diameter ratio of 1.25
- Wing lengths constituting more than 50% of body length
- Supersonic speeds

The FVM method, as with the SCV and DVM methods, reduces the three-dimensional steady problem to a two-dimensional unsteady problem and models the

shed vortices as single concentrated vortices. In contrast to other existing methods, the FVM method models the vortex positions as a function of the shed vorticity, but requires initial vortex positions and strengths to solve the first order differential equations. The vortex strength is also determined and, together with the vortex positions, is used to calculate the normal force and centre-of-pressure induced by the vortex sheet. This is accomplished using the vortex impulse theorem. Also, the Kutta condition is not satisfied at any stage in the FVM solution method. The set of differential equations to be solved require an initial vortex position and strength [1] [2]. Contrary to other engineering methods, the FVM method does not assume a constant vortex strength but determines the vortex positions using the shed vorticity. The normal force coefficient is calculated using a component build-up method, which is a summation of three components: normal force coefficient due to forebody $\left(C_{N_{B_{forebody}}}\right)$, wing-body section $\left(C_{N_{B+W}}\right)$ and aftbody $\left(C_{N_{B_{aftbody}}}\right)$.

$$C_{N_{BW}} = C_{N_{B_{forebody}}} + C_{N_{B+W}} + C_{N_{B_{aftbody}}} . \tag{43}$$

The method was applied to four different configurations and compared to available experimental data at different Mach numbers. It was concluded [1] [2] that the method predicts the normal force for angles of attack up to 10°. The centre-of-pressure predictions however were poor for all four configurations and are therefore a limitation of the method (see Figure 19).

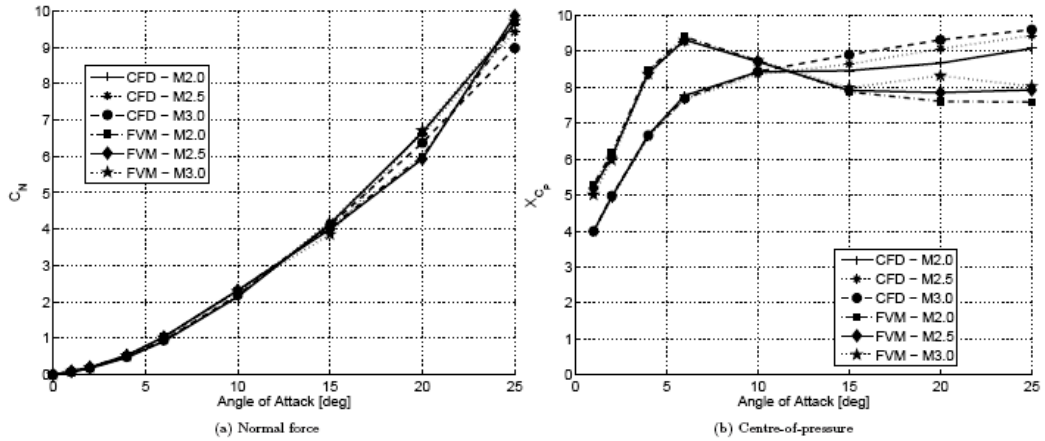

Figure 19: FVM and CFD comparison [27] for (a) normal force coefficient and (b) centre-of-pressure position

Recently both the SCV and DVM methods were applied [1] [27] to a wing body combination similar to the configuration described above with wings of aspect ratio 0.025 and taper ratio of approximately 1 (also referred to as strakes). Three different Mach numbers were considered namely 2.0, 2.5 and 3.0. The lee side flow was shown to be largely influenced by the secondary vortex that arises due to the wing-body junction. The engineering predictions were also compared to validated computational fluid dynamics (CFD) simulations (see Figure 20). When compared to configurations with delta wings, the DVM method required fewer number of time steps for bodies with strakes to accurately capture the shed vorticity. The SCV method proved less accurate for bodies with strakes as the method over-predicts normal forces at angles of attack larger than 4°. The concepts of these engineering methods are discussed in more detail in the following section, focussing on the DVM and FVM methods which are investigated in this study.

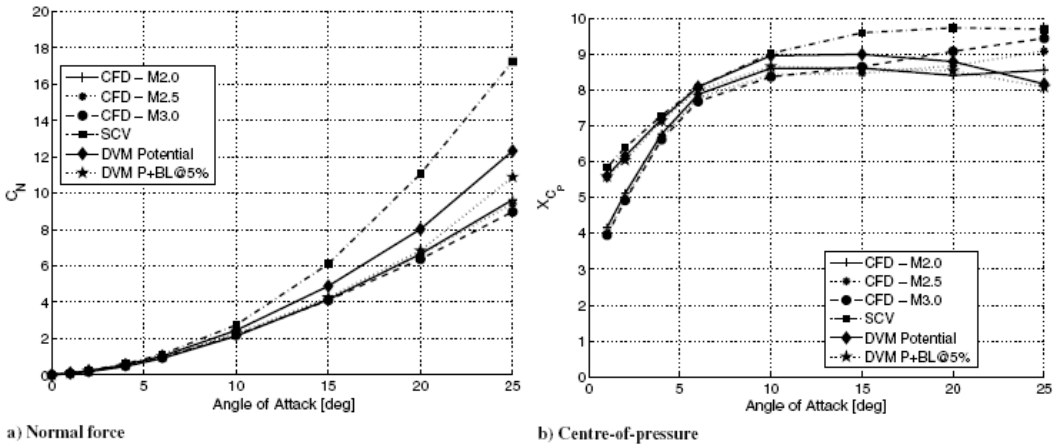

a) Normal force

b) Centre-of-pressure

Figure 20: SCV and DVM comparison to CFD for (a) normal force coefficient and (b) centre-of-pressure position [27]

3. Research Approach

3.1. Approach

A database of specific flow features was created for configurations of varying span to body diameter ratios (s/D) at incompressible Mach numbers. The flow features relevant to this study include normal force, centre-of-pressure and vortex positions. These were determined using three different methods:

1. CFD simulations
2. Experimental testing
3. Engineering method predictions

The CFD simulations were carried out using ANSYS Fluent v15 with meshes created in Gambit. The simulations were run at Mach numbers 0.1 and 0.2 and angle of attack range of $0° \leq \alpha \leq 25°$. Full scale symmetrical models were created for the computational simulations as no asymmetrical/three-dimensional effects are expected at these low angles of attack.

The experimental tests were carried out in order to validate the loads resulting from the CFD simulations. A 56% scaled model was designed for the experimental validation. Tests were conducted at Mach numbers 0.1, 0.2 and 0.3. The loads of interest, normal force and pitching moment, were measured up to an angle of attack of 20°.

In addition to the FVM method, another engineering level prediction method called the discrete vortex model (DVM) method was utilized for comparison purposes because of its accepted usage [27]. Both the FVM and DVM methods were developed

for missiles with wings/strakes, therefore the load predictions using these two methods were carried out for the three noted body-strake configurations only. The loads predicted by the FVM and DVM methods do not include the total loads experienced by the missile, but are the component loads due to the vortex separation.

In this study, the method for calculating the normal force over the entire configuration is based on the component build-up method. This allows the comparison to the total loads that are obtained from CFD simulations as well as experimental testing. The subsequent sections discuss these methods in more detail, including the comparisons of the predicted loads and vortex positions.

3.2. Configuration

Three body-strake configurations with modelled each with a different span to body diameter ratio (s/D) namely 1.25, 1.5 and 1.75. The general dimensions for these configurations are illustrated in Figure 21.

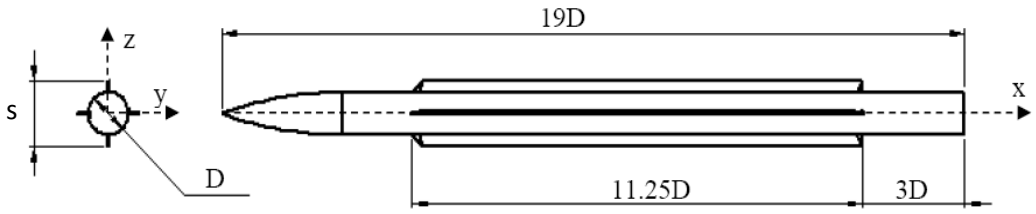

Figure 21: Body-stake configurations general dimensions

The forebody of the body-strake configurations is defined as the body section upwind of the strake leading edges which includes a nose of 3 diameters or calibers (3D). The total forebody length is thus 4.75D. At zero roll angle the strakes are in the '+' orientation as shown on the left hand side of Figure 21. Non-zero roll angles were not considered in this study.

4. Free Vortex Model Method

The purpose of the free vortex model (FVM) method is to predict the aerodynamic loads and lee side flow features of slender body configurations with low aspect ratio wings (strakes) in the '+' orientation. The method focuses on predicting the load component due to vortex separation; this is explained in more detail in Section 4.3. The calculated loads and flow features include the normal force coefficient and centre-of-pressure positions as well as vortex positions and strengths.

The calculations are carried out by reducing the steady, three-dimensional (3-D) problem to a transient, two-dimensional (2-D) problem. This is accomplished by dividing the 3-D flow field into multiple planes (see Figure 22) so that a difference in time dt in the 2-D impulsively started flow corresponds to the axial distance between planes dx. Time (dt) and axial distance (dx) are related by the free stream velocity,

$$V_\infty = \frac{dx}{dt}. \tag{44}$$

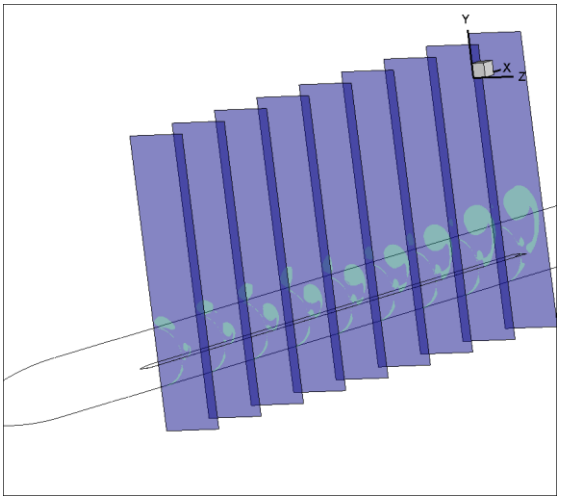

Figure 22: Flow field divided into multiple planes for impulsively started 2-D problem

This simplification reduces the computing time of the engineering method and allows incompressible potential flow equations to be used. The calculation method of the FVM method is described in this section.

4.1. Theoretical Formulation

The linear potential equation is shown in Equation (6) and is repeated here for convenience:

$$\phi_{\bar{x}\bar{x}}\left(1-{M_\infty}^2\right)+\phi_{\bar{y}\bar{y}}+\phi_{\bar{z}\bar{z}}=\frac{1}{c_\infty^2}\phi_{tt}+2\frac{M_\infty}{c_\infty}\phi_{\bar{x}t}\,.$$

Assuming 2-D flow (in the y-z plane), Equation (6) is reduced to

$$\phi_{\bar{y}\bar{y}}+\phi_{\bar{z}\bar{z}}=0\,. \tag{45}$$

This method of reducing a 3-D problem to a 2-D problem exists under the assumption that the body diameter is constant (or changes slowly) in the direction perpendicular to the plane considered.

For a noncircular cross-section (which is the case for body-strake combinations) the potential equations are not readily available. Therefore the physical plane ($\sigma = y + iz$) with the wing-body cross-section is transformed to a circle plane ($\nu = \tau + i\lambda$) in order to perform the analysis. The transformation follows that of references [23], [27] and [56]. The physical and transformed planes are defined as in Figure 23. The transformation is defined any point in the σ plane can be transformed to the ν plane and vice versa. Thus

$$\nu = \nu(\sigma)\,, \tag{46}$$

$$\sigma = \sigma(\nu)\,. \tag{47}$$

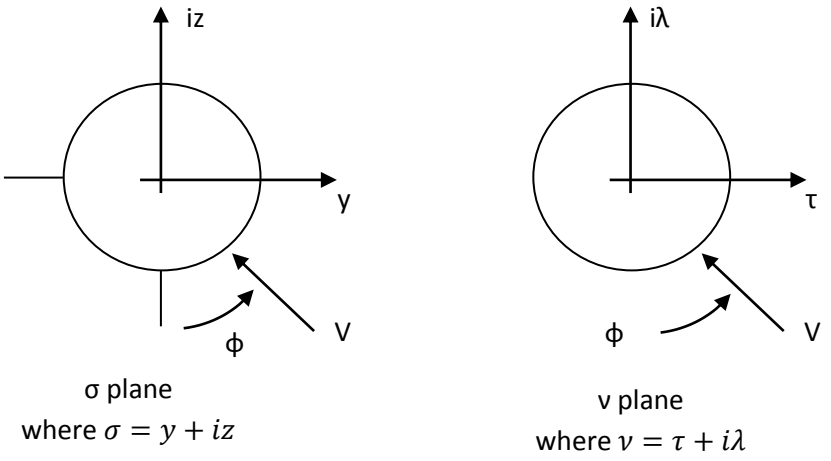

Figure 23: Cross-section physical transformation

The transformation and its derivatives are given as:

$$\sigma^2\left(1+\frac{a^4}{\sigma^4}\right)=\nu^2\left(1+\frac{{r_o}^4}{\nu^4}\right), \tag{48}$$

$$r_o^2=\frac{1}{2}s^2\left(1+\frac{a^4}{s^4}\right), \tag{49}$$

$$\frac{d\nu}{d\sigma}=\frac{\sigma}{\nu}\left(\frac{1+\frac{a^4}{\sigma^4}}{1+\frac{{r_o}^4}{\nu^4}}\right), \tag{50}$$

$$\frac{d^2\nu}{d\sigma^2}=\frac{d\nu}{d\sigma}\left[\frac{1}{\nu}\left(3-\frac{4}{1-\frac{{r_o}^4}{\nu^4}}\right)\left(\frac{d\nu}{d\sigma}\right)-\frac{1}{\sigma}\left(-\frac{4}{1-\frac{a^4}{\sigma^4}}\right)\right] \tag{51}$$

where r_o is the circle radius in the ν–plane. It was shown in reference [1] that the complex potential for two vortices with strengths Γ_1 and Γ_2 in the ν-plane is

$$W(\nu)=iV\sin\alpha\, e^{-i\phi_x}\left(\nu-\frac{r_o^2e^{i2\phi_x}}{\nu}\right)-\frac{i\Gamma_1}{2\pi}\ln\left(\frac{\nu-\nu_1}{\nu-\frac{r_o^2}{\bar{\nu}_1}}\right)-\frac{i\Gamma_2}{2\pi}\ln\left(\frac{\nu-\nu_2}{\nu-\frac{r_o^2}{\bar{\nu}_2}}\right) \tag{52}$$

where ϕ_x is the roll angle in degrees. The complex velocity in the σ-plane at $\sigma = \sigma_1$ and generalized to the j^{th} vortex is then

$$\frac{dW}{d\sigma} = v_j - iw_j$$

$$= \left[-iV \sin\alpha \, e^{-i\phi_x} \left(1 - \frac{r_o^2 e^{i2\phi_x}}{v_1^2} \right) + \frac{i\Gamma_j}{2\pi} \left(\frac{1}{v_j + \frac{r_o^2}{\bar{v}_j}} \right) - i \sum_{k=1}^{n} \left(\frac{1}{v_j + v_k} - \frac{1}{v_j + \frac{r_o^2}{\bar{v}_2}} \right) \right] \left(\frac{dv}{d\sigma} \right)_{\sigma=\sigma_j}$$

$$- \frac{i\Gamma_j}{\pi} \left(\frac{d\sigma}{dv} \right) \left(\frac{d^2 v}{d\sigma^2} \right)_{\sigma=\sigma_j} . \tag{53}$$

It was also shown [1] that the equations of the rate of change for the j^{th} vortex with respect to the axial are

$$\frac{dy_j}{dt} = v_j \frac{1}{V \cos\alpha} \tag{54}$$

and

$$\frac{dz_j}{dt} = w_j \frac{1}{V \cos\alpha} . \tag{55}$$

4.2. Vortex Induced Loads

The vortex impulse theorem [57] states that, for a wing-body-tail combination, the influence of the wing wakes on the other components are due to the impulse of each shed vortex and its image vortex, in a transformed circle plane. The interaction of the wing wake is utilized to calculate the forces and moments due to the presence of shed vortices.

The impose loads can be expressed [1] as

$$F_Z - iF_Y = \rho V \Gamma \nu_r \tag{56}$$

where ν_r is the complex distance between the vortex and its image vortex in the circle plane. With regards to this study, the vortex impulse theorem will be applied in particular when a vortex sheet (or concentrated vortex) is shed from the body.

4.3. Component build-up method

In this study, the method for calculating the normal force over the entire configuration is based on the component build-up method. This allows the comparison to the total loads that are obtained from CFD simulations as well as experimental testing owing to the fact that the normal force obtained from the FVM method is the component due to the vortex separation. The configuration as discussed in Section 3.2 may be divided into three parts: the fore body section, cruciform wing-body section and the aft body section. Each of these sections generates a normal force component that equals the total normal force when summed:

$$C_N = C_{N_{fore\ body}} + C_{N_{BW}} + C_{N_{aft\ body}} \tag{57}$$

where $C_{N_{BW}}$ is the cruciform wing-body component. According to Allen [22] the normal force for cruciform wing-body section is the sum of two components, namely the load due to an attached potential flow and a vortex induced load. The total normal force is then

$$C_N = C_{N_{fore\ body}} + C_{N_{attached}} + C_{N_{vortex}} + C_{N_{aft\ body}}\ . \tag{58}$$

The attached potential component is given [1] as

$$C_{N_{attached}} = \left(K_{W_B} + K_{B_W}\right) C_{N_{W_a}} \sin\alpha \cos\left(\frac{\alpha}{2}\right). \tag{59}$$

Therefore the total load can be expressed as

$$C_N = C_{N_{fore\ body}} + \left(K_{W_B} + K_{B_W}\right) C_{N_{W_a}} \sin\alpha \cos\left(\frac{\alpha}{2}\right) + C_{N_{vortex}} + C_{N_{aft\ body}} \tag{60}$$

where $C_{N_{vortex}}$ is the normal force component induced by the vortex. $C_{N_{vortex}}$ is then determined using the FVM method and the accuracy with which it is predicted is the topic of this study.

5. Discrete Vortex Model Method

Along with the experimentally validated CFD data, the free vortex model (FVM) method will also be compared to the discrete vortex model (DVM) method which is an established engineering method [23] [27] [58]. Similarly to the FVM method, the DVM method also predicts the load component due to vortex separation and divides the lee-side flow field into multiple two-dimensional sheets in order to reduce the steady, three-dimensional problem to a transient, two-dimensional problem.

5.1. Summary of Theory

The vortex sheet that separates from the strake side edge is represented by multiple discrete singularities (vortex filaments). The shed vortices are then modeled as free vortices which then move as Langrangian fluid particles [27].

Similar to the FVM method, the complex potential for the flow is transformed to the circle plane (see Figure 23 in Section 4.1). If the complex potential is $W(\nu)$, then the complex velocity is given as

$$\frac{dW(\nu)}{d\sigma} = \frac{dW(\nu)}{d\nu}\frac{d\nu}{d\sigma}. \tag{61}$$

The total complex potential W(ν) for two vortices with strengths Γ_1 and Γ_2 in the transformed (ν) plane is

$$W(\nu) = iV\,sin\,\alpha\,e^{-i\phi_x}\left(\nu - \frac{r_o^2 e^{i2\phi_x}}{\nu}\right) - \frac{i\Gamma_1}{2\pi}ln\left(\frac{\nu-\nu_1}{\nu-\frac{r_o^2}{\bar{\nu}_1}}\right) - \frac{i\Gamma_2}{2\pi}ln\left(\frac{\nu-\nu_2}{\nu-\frac{r_o^2}{\bar{\nu}_2}}\right). \tag{62}$$

Thus the complex velocity in the σ-plane at $\sigma = \sigma_1$ and generalized to the j[th] vortex was shown to be

$$v_j - iw_j = \left[-iV \sin\alpha\, e^{-i\phi_x} \left(1 - \frac{r_o^2 e^{i2\phi_x}}{v_1^2} \right) + \frac{i\Gamma_j}{2\pi} \left(\frac{1}{v_j + \frac{r_o^2}{\bar{v}_j}} \right) - i \sum_{k=1}^{n} \left(\frac{1}{v_j + v_k} - \frac{1}{v_j + \frac{r_o^2}{\bar{v}_2}} \right) \right] \left(\frac{dv}{d\sigma} \right)_{\sigma} - \frac{i\Gamma_j}{\pi} \left(\frac{d\sigma}{dv} \right) \left(\frac{d^2 v}{d\sigma^2} \right)_{\sigma=\sigma_j} . \tag{63}$$

For the DVM method the Joukowski-Kutta condition is employed which states that a stagnation point exists at an edge with a finite angle or sharp point. Thus, for the potential $W(v)$, a stagnation condition exists at side edge in the circle plane so that

$$\frac{dW(v)}{d\sigma} = 0 .$$

When the Joukowski-Kutta condition is applied to Equation (62), this then results in the following relationship [1] [27]:

$$-iV \sin\alpha\, e^{-i\phi_x} \left(1 + \frac{r_o^2 e^{i2\phi_x}}{v_{sp}^2} \right) = \frac{i}{2\pi} \sum_{k=1}^{n} \Gamma_k \left(\frac{1}{v_{sp} + v_k} - \frac{1}{v_{sp} + \frac{r_o^2}{\bar{v}_k}} \right) \tag{64}$$

where v_{sp} is the position where separation occurs in the ν-plane. The method of reference [59] is then utilized to calculate the vortex strengths, which assumes that the velocity at the initial point of separation on a sharp edge is $v = \frac{1}{2} Va$. The shed line vortex is propagated outward along the spanwise axis at a distance $\Delta x = v\Delta t$ and is replaced by a single concentrated vortex which, along with the discrete vortices, is mapped as Lagrangian fluid particles. From the potential $W(v)$ the complex velocities at the Joukowski-Kutta edge are calculated as

$$v - i\omega = \left.\frac{dW}{d\sigma}\right|_{\nu=\nu_{sp}} = \left.\frac{dW}{d\nu}\frac{d\nu}{d\sigma}\right|_{\nu=\nu_{sp}}. \tag{65}$$

Secondary separation due to boundary layer has also been considered by using the criterion developed by Stratford [60] [61]. Given that the separation is limited to the body only and that the boundary layer is laminar (as in the condition in reference [27]), separation occurs when the following criterion [60] is met:

$$\left[C_p\left(x\frac{\partial C_p}{\partial x}\right)^2\right] = 7.64 \times 10^3$$

for a constant pressure gradient $\left(\frac{\partial p}{\partial x}\right)$, where x is the distance from the stagnation point and $C_p = \frac{p_{sep}-p_o}{\frac{1}{2}\rho {V_o}^2}$.

There are two variations of the DVM method that are utilized in this study; the first is referred to as the DVM potential method and the second as the DVM boundary layer (BL) method. The potential method is the base formulation initially proposed by Sacks et al [59] for slender wing applications. The first application of the DVM method to so called wing-body configurations was done by Mendenhall and Lesieutre[62] on forebodies with chines in subsonic flow. The method was recently extended to cruciform wing-body combinations by Tuling [1] which is applicable to the configurations in the present study, although the method was applied to supersonic speeds. The theoretical development is described in more detail in references [1] and [2].

Reference [27] investigated the DVM method's dependence on the number of discrete vortices used. This also translates to the number of steps used along the strake edge and it was found that, for vortex paths in $z \geq 0.4$ and $y \geq 1.2$, at least

120 vortices were required to sufficiently model the flow over the strakes. Since the configurations relevant to this study are the same as that of reference [27], the same amount of steps was utilized in this application of the DVM method. Figure 24 gives an indication the vortex path as a function of step size (number of vortices) in the physical plane, as assessed by reference [27]. The DVM potential method was used to evaluate the grid sensitivity.

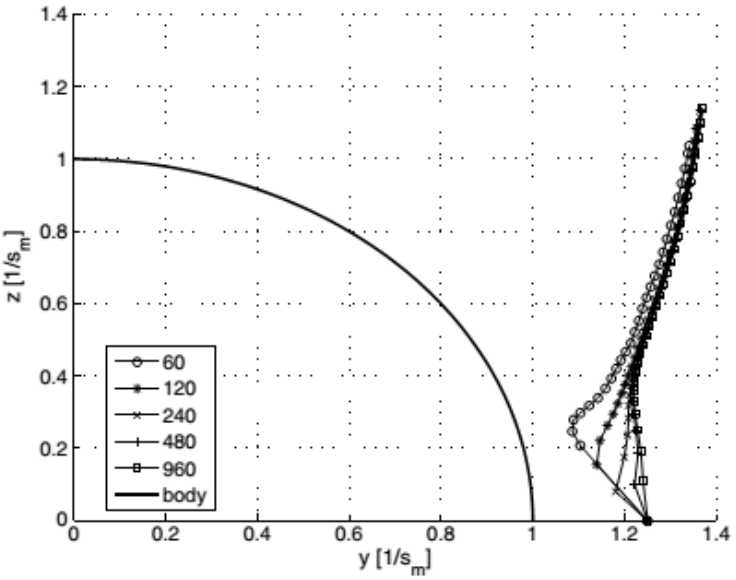

Figure 24: Vortex paths as a function of step size [27]

The DVM BL method was initially applied by Mendenhall and Lesieutre [62] after it was found that, if the initial vortex positions were placed too close to the body, numerical difficulties may arise in that the vortex becomes "trapped" in the BL [1]. This then influences the vortex trajectory calculations. To prevent these difficulties, they proposed placing the shed vortex well outside the boundary layer at a distance of 5% of the of the local body radius from the surface.

There are some distinct differences between the FVM and DVM methods. Firstly, the computing time for the FVM method is much less than that of the DVM method. Where the FVM method completes a simulation in a matter of seconds, with the same

CPU power, the DVM method will complete a simulation in a matter of hours. Secondly, the DVM method divides the vortex sheet into multiple vortex filaments (Figure 25 (a)) and the FVM method calculates vortex positions by tracking the single rolled up vortices (Figure 25 (b)). The DVM method defines the Joukowski-Kutta condition at the strake side edges, whereas the Joukowski-Kutta condition is not specified at any point in the FVM method. Lastly, the FVM method calculates the vortex strengths at each lengthwise station (see Figure 22), whereas the DVM method assumes a constant vortex strength throughout.

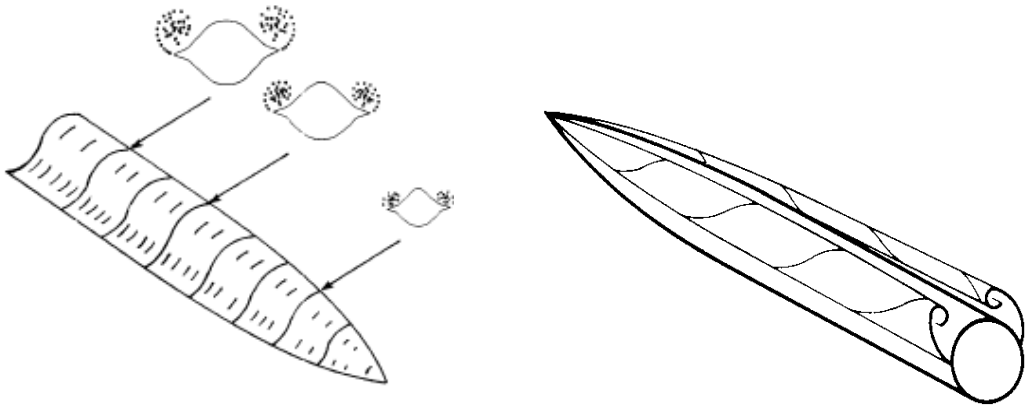

(a) (b)

Figure 25: (a) Vortices divided into multiple vortex filaments and (b) single consentrated vortex or rolled up vortex sheet

5.2. DVM Results

Prediction results for both the potential and boundary layer formulations of the DVM method are illustrated in Figure 26. In both methods a body vortex is specified with the same initial vortex positions and strengths. The results show that for the span to body diameter (s/D) ratios of 1.25 and 1.5 the DVM boundary layer (BL) method

under-predicts the normal force (C_N) when compared to the potential method. The error between the two methods is observed to decrease with increase in strake span such that the two curves overlap at s/D=1.75.

In contrast, very little difference is observed between the BL and potential prediction of the centre-of-pressure positions (X_{C_p}). Since X_{C_p} is dependent on both the normal force and pitching moment (C_m), this indicates that the difference in C_N between the two methods has a linear relationship to the difference in C_m predicted for the two methods. Thus the slope $\frac{dC_m}{dC_N}$ remains almost constant with increase in strake span resulting in small differences in X_{C_p} with increasing strake span.

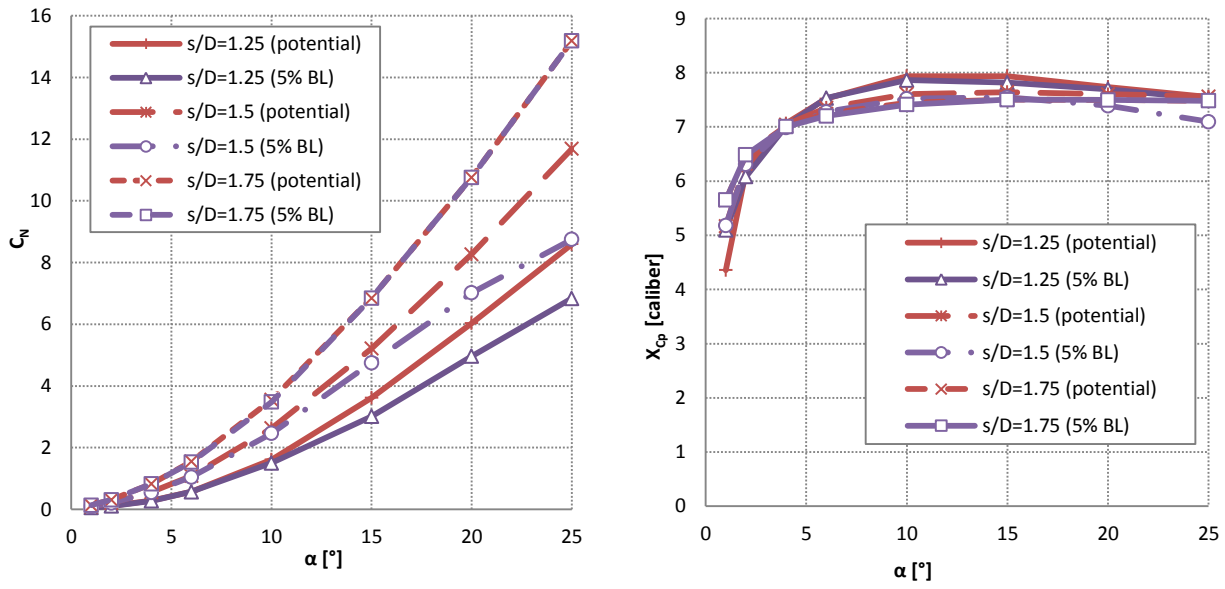

(a) (b)

Figure 26: DVM predictions for (a) normal force coefficient and (b) centre-of-pressure position

These load results as well as the predicted vortex positions are discussed in more detail in Section 7, when compared to the FVM method and validated CFD data.

6. Data Validation

6.1. Numerical Simulations

A global loads and flow field database was compiled using CFD. A symmetric computational model was constructed in the assumption that no asymmetric vortices are expected at the low angles of attack relevant to this study (see Section 3). Mesh independent results were obtained with a structured mesh of 22 million cells. The base pressure drag was found to fluctuate the most with change in mesh density and is given as an example of the mesh convergence study in Figure 27. In order to accurately capture the nature of the vortices and their effects on the aerodynamic loads, the meshed volume containing the lee-side flow and shed vortices was refined so that the vortex core consisted of at least 8 cells (in the crossflow plane).

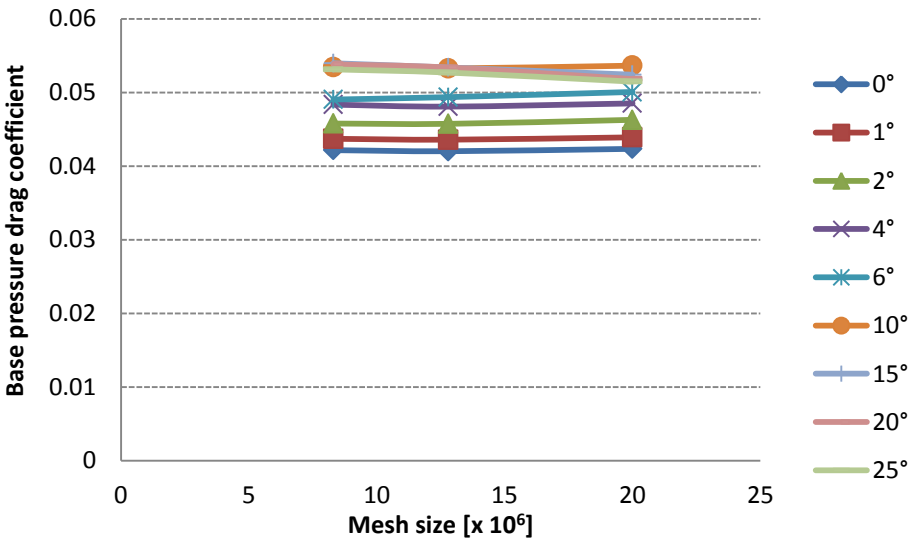

Figure 27: Mesh convergence for base pressure drag for s/D=1.25

The procedure of simulating the noted configurations in this part of the numerical study entails pre-processing in Gambit, simulations in ANSYS Fluent and post-processing using both Tecplot 360 and MATLAB (see Figure 28).

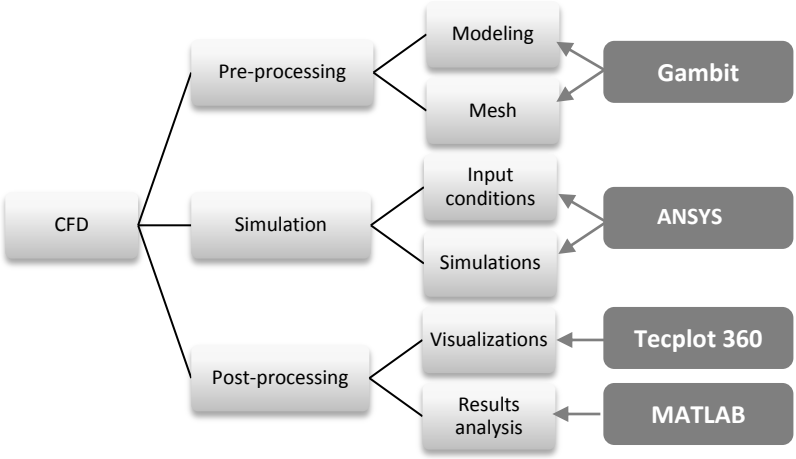

Figure 28: Numerical simulation process

6.1.1. Pre-processing

Both the modeling of the configuration as well as the construction of the mesh was carried out in the code Gambit. Three bodies with strakes were simulated, each with a different span to body diameter ratio (s/D) namely 1.25, 1.5 and 1.75.

The mesh boundaries are located at a distance of 100 times the length of the model away from the body in all directions. This is to ensure that the influences of the aerodynamic characteristics of the model on the wider volume of air, due to the conditions of subsonic flow, are included in the simulations.

Three structured meshes with increasing number of cells were investigated and the finest mesh with 22 million cells was found to be mesh-independent. Figure 29 shows a section of the final mesh. The boundary layer was simulated with near-wall treatment such that at least three cells were present in the viscous sub-layer, for which the wall y+-values are calculated by the Fluent code to be less than 1.

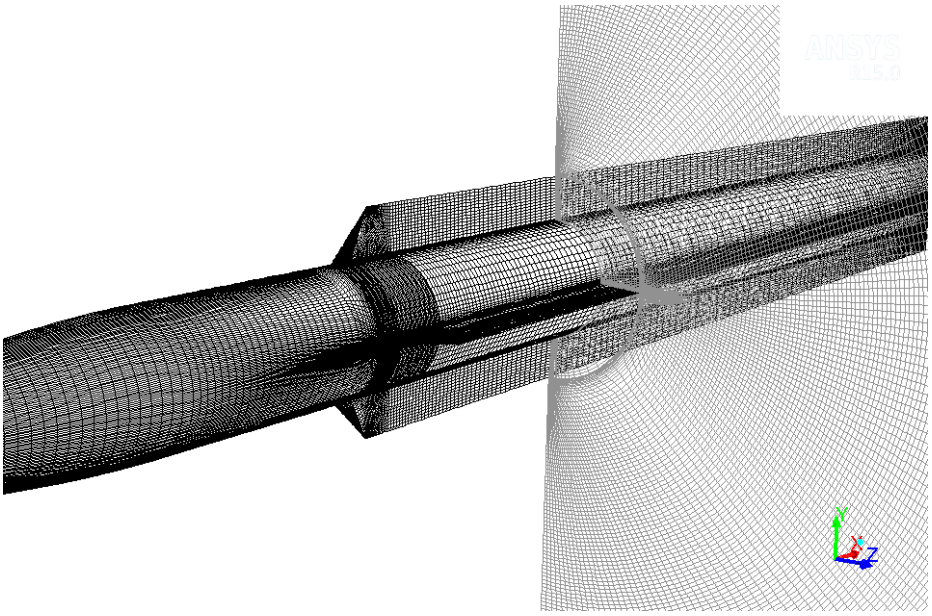

Figure 29: Mesh section of body-strakes configuration

6.1.2. Simulations

The CFD simulations were performed using ANSYS Fluent v15, implementing a coupled pressure-velocity algorithm with second order upwind spatial discretization scheme. The Spalart-Allmaras turbulence model was used as it is less costly while still robust. The Spalart-Allmaras model was also specifically designed for aerospace applications and since the results were shown to be highly accurate (as discussed in the following section), no additional turbulence models were simulated. Simulations were run on 48 nodes taking approximately 20 CPU hours. The solutions were considered converged when the residuals had reduced by a third order of magnitude and the loads asymptoted to constant values. The simulations were run at Mach numbers of 0.1 and 0.2 and angles of attack from 0° to 25°. For each angle of attack the flow angle is changed in the inlet and outlet boundary conditions, so that only one mesh is required for each configuration. The inlet boundary condition is specified as a pressure-far-field condition with a pressure outlet. The inlet and outlet conditions for the relevant Mach

numbers were determined to be the same as that of the wind tunnel conditions for comparison, these are given in Table 2.

Table 2: CFD input flow conditions

Mach Number	**0.1**	**0.2**
Static Pressure	48.6 kPa	47.6 kPa
Static Temperature	283K	286 K
Re_D	$88.7x10^3$	$174.3 x10^3$

The relevant loads were extracted from the Fluent results and were plotted against the available experimental data. In addition to the loads, the body and wing vortex positions were also extracted from the CFD data. The CFD results and the comparisons to experimental data are given in the subsequent sections for all configurations.

6.1.3. CFD Results

Aerodynamic loads

The simulation load results for normal force coefficient (C_N), pitching moment coefficient (C_m), centre-of-pressure position (X_{C_p}) and axial force coefficient (C_A) are shown in Figures 30 and 31. It should be noted that no Mach number dependence is observed for both C_N and C_m. As expected both, these coefficients increase with increasing wing span. Values of X_{C_p} (in calibers) are also shown to be Mach independent and only small differences exist for varying wing spans. At angles of attack (α) below 5°, X_{C_p} moves further aft with increase in wing span. Between 5°

and 15° angle of attack, however, X_{C_p} shifts further forward toward the nose with increase in wing span. Above 15° the change in X_{C_p} with wing span is negligible. There is a near linear relationship between the increase in C_N and C_m as the strake span increases, thus the slope $\frac{dC_m}{dC_N}$ remains almost constant with increase in strake span. Since X_{C_p} is directly related to $\frac{dC_m}{dC_N}$, the increase in strake span has a very small effect on X_{C_p}.

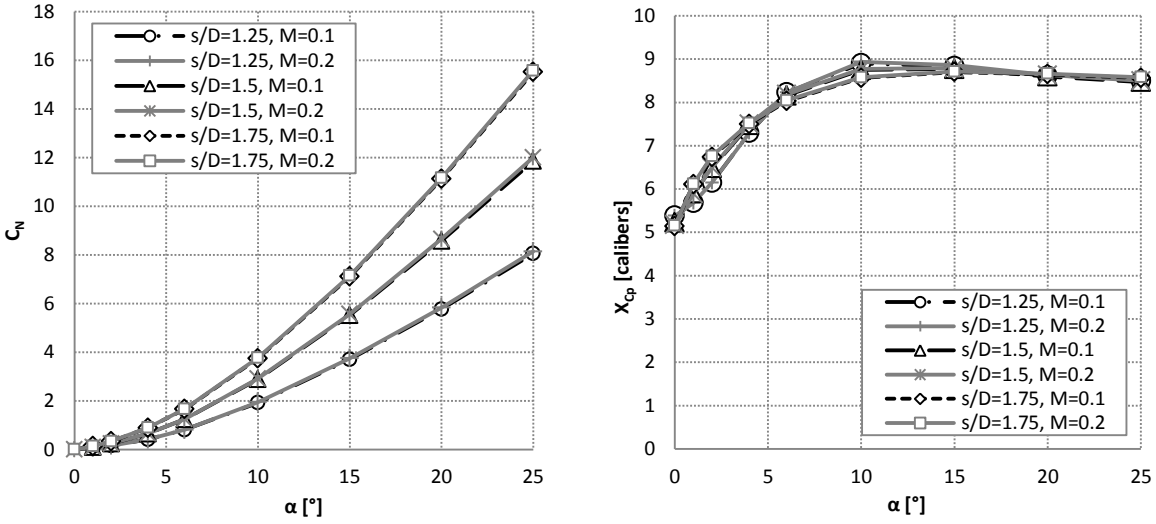

(a) (b)

Figure 30: (a) Normal force and (b) centre-of-pressure position CFD results for all Mach numbers and configurations

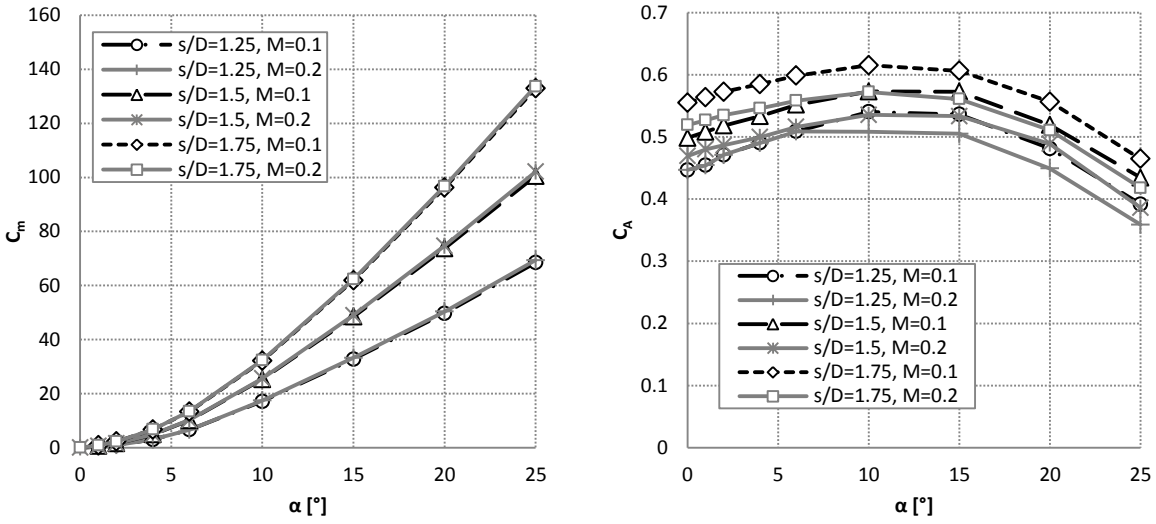

(a) (b)

Figure 31: (a) Pitching moment and (b) axial force position CFD results for all Mach numbers and configurations

A reduction in C_A is observed with increase in Mach number and subsequent increase in Reynolds number based on body diameter (Re_D), although little difference is observed in the curve slopes for each configuration. For s/D=1.25 however, no difference is observed in the absolute C_A value for $\alpha \leq 6°$. Above 10° C_A for Mach 0.2 is offset by a near-constant value. These C_A results indicate critical Re_D behavior usually observed in cylinder crossflow as shown in Figure 32. It may be observed that the crossflow in the presence of the strakes imitate crossflow in the presence of a transitional bubble. This effect decreases with decreasing strake span, resulting in transcritical behavior at $\alpha \leq 6°$ for s/D=1.25 where C_A remains constant with increase in Re_D.

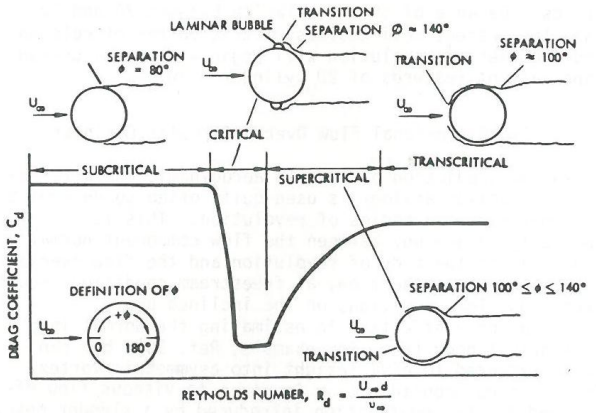

Figure 32: Drag bucket curve for a cylinder in crossflow [63]

Vortex shedding

The positions of the vortices shed from the strakes are given in this section for all configurations and Mach numbers. The lateral and vertical vortex positions are plotted against normalized axial positions in calibers for angles of attack of 6°, 10°, 15°, 20° and 25° in Figures 33 to 37. The lateral (y) and vertical (z) distances are non-dimensionalised by the body radius (a).

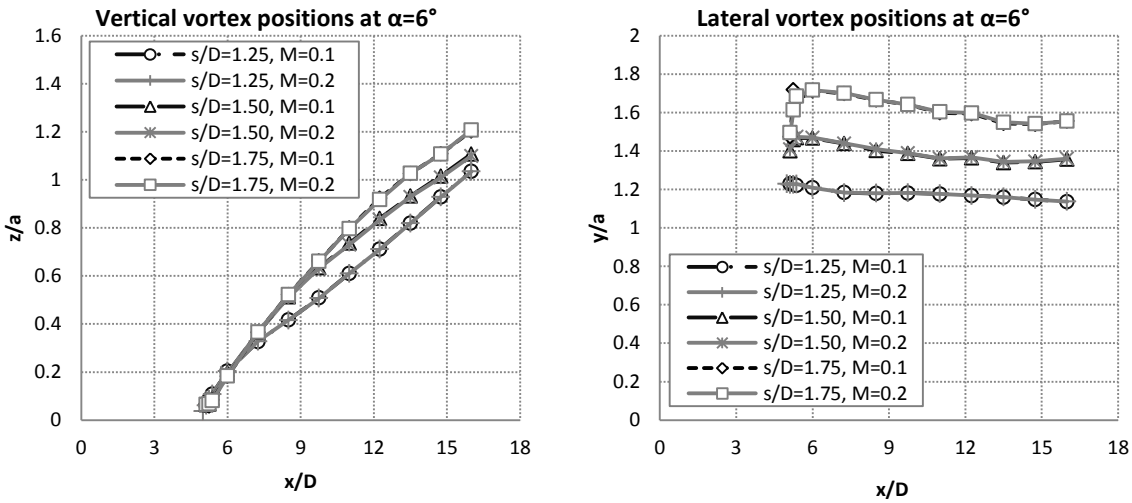

(a) (b)

Figure 33: CFD (a) vertical and (b) lateral vortex positions for α=6°

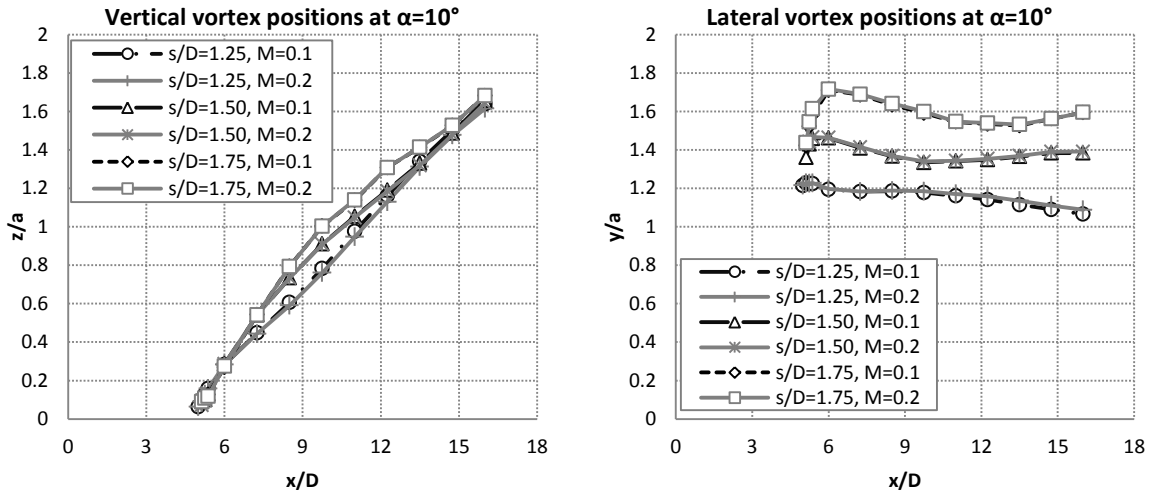

(a) (b)

Figure 34: CFD (a) vertical and (b) lateral vortex positions for α=10°

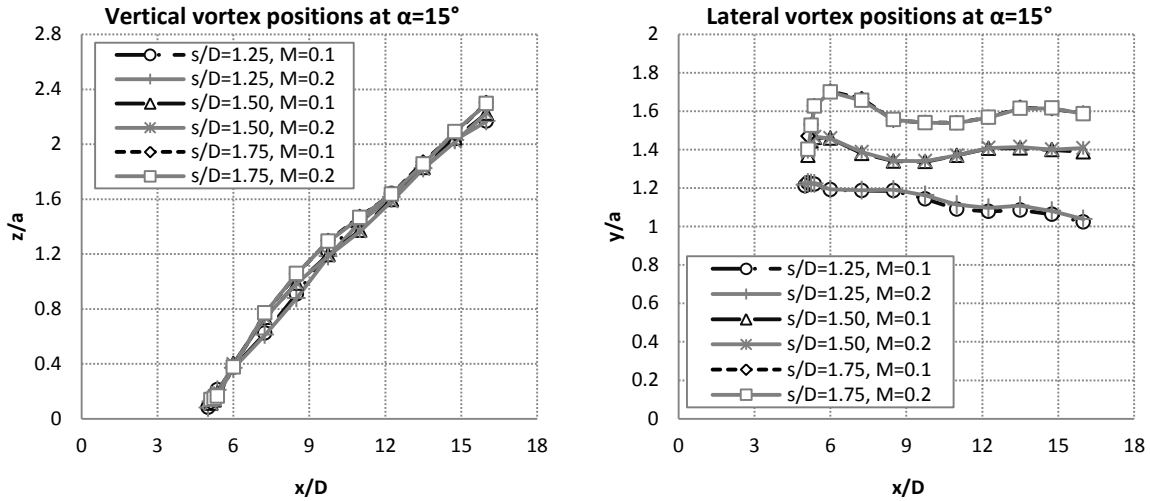

(a) (b)

Figure 35: CFD (a) vertical and (b) lateral vortex positions for α=15°

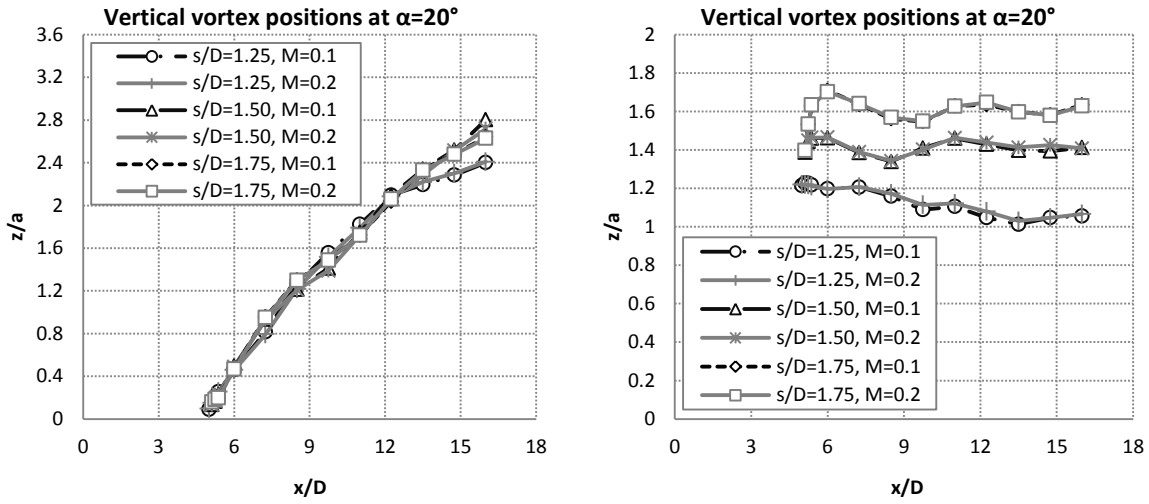

(a) (b)

Figure 36: CFD (a) vertical and (b) lateral vortex positions for α=20°

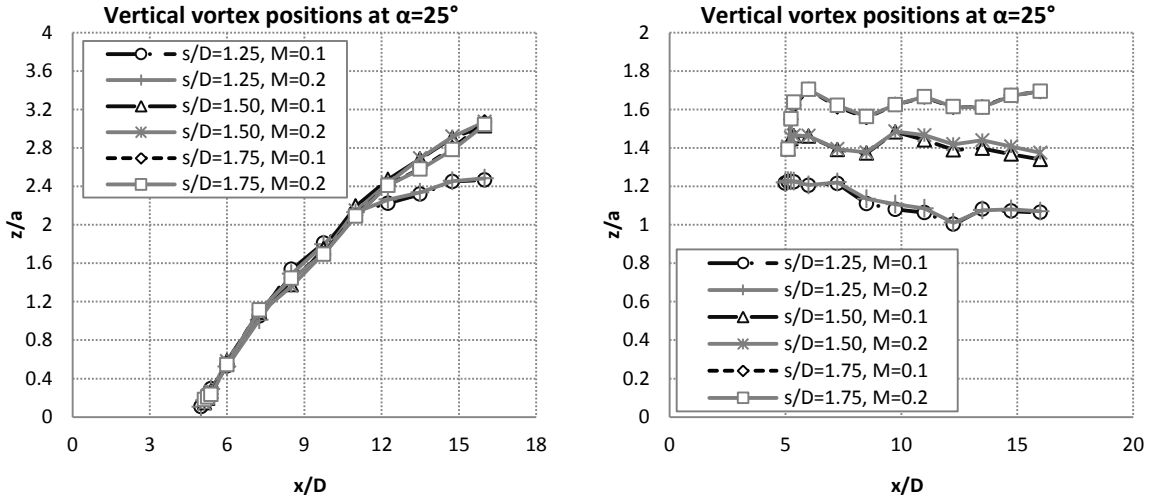

(a) (b)

Figure 37: CFD (a) vertical and (b) lateral vortex positions for α=25°

As with the load results the data shows no Mach number dependence. Lateral vortex positions show very similar trends at the various angles of attack for each wing span. For s/D=1.25, the vortex starts at the strake leading side edge and moves inward toward the vertical symmetry plane. For s/D=1.50 and 1.75 the vortex initially moves outward and then moves back inward and outward again in a wavelike fashion in the

axial direction. This motion was initially thought to be a result of body vortex interaction with the strake vortex, however it was found that the body vortex dissipates at x/D above 8.5. Thus the wavelike spanwise movement of the vortex may be the natural movement of the vortex in the presence of the body.

The vertical vortex positions for the different s/D ratios become more similar with increase in angle of attack. At $\alpha = 6°$ the vortices move away from the body with increasing axial distance. The vortices detach at the leading edge of the strake and move further away from the body with increasing wing span, particularly toward the rear of the body. At $\alpha = 10°$ the vertical positions of the concentrated vortex along the axial direction move further away with increase in wing span between 6D and 10D. Above 10D the slope decreases and the vertical positions at the end of the body for the three wing spans seem very similar. At $\alpha = 15°$ the vertical vortex positions for all three configurations are very similar, with very little differences in height and slope. At $\alpha = 20°$, however, there is very little variation in the vertical vortex positions between the three different wing spans up to an axial position of 13.5D, after which a decrease in slope is observed for the s/D=1.25 vortex. This decrease in the s/D=1.25 slope appears further forward, around 11D, at $\alpha = 25°$. At this angle the variations in vertical vortex positions for all three configurations up to 11D are even less and the positions for the s/D=1.5 and 1.75 configurations continue to correspond beyond 11D. Since the vertical positions are largely influence by the position of strake leading edges, there is less variation in the vertical vortex positions as the leading edge positions remain constant with increasing strake span.

The increase in spanwise vortex positions with increasing strake span is expected as the origin of the vortices is greatly influenced by the location of the strake side edges.

Thus the increase in strake span automatically results in an offset in spanwise location of the vortices. At $\alpha \geq 15°$ a body vortex is also present, which was found to be independent of the strake profiles as it develops near the nose of the missile. At these higher angles of attack the wing vortices are also influenced by the presence of the body vortex. The decrease in vertical positions at $\alpha \geq 15°$ points towards a decrease in the influence of the body vortex. This results from the dissipation or separation of the body vortex from the wing vortex.

6.2. Experimental Validation for CFD Results

6.2.1. Experimental Setup

The benefit of CFD simulations is that it provides qualitative information on the flow that would not be possible in experimental testing. It is, however, essential that the CFD data be validated experimentally due to the complex nature of the flow around circular slender bodies at subsonic speeds. The comparison will determine the level of accuracy of the CFD simulations at the relevant Mach numbers and angles of attack. The experimental tests were conducted in the low speed facility of the CSIR. The low speed wind tunnel (LSWT) is a closed loop atmospheric wind tunnel with maximum speed of 110 m/s (Mach 0.35) and a 2.2m x 1.5m test section. A 56% scaled model was designed for the experimental tests with a maximum body diameter of 45mm. The tunnel blockage was is determined as follows:

$$blockage\% = \frac{S}{S_{TS}} \times 100 \tag{66}$$

where S_{TS} is the test section cross-section area in m^2. Thus the blockage at 0° angle of attack (α) for the LSWT tests were determined to be

$$blockage\% = \frac{\frac{\pi}{4}(0.045)^2}{2.2 \times 1.5} \times 100 = 0.0482\% \approx 0.05\% .$$

In reference [64] an aircraft model with a 18 inch (≈ 0.46 m) wingspan was tested in a 3ft x 4ft (≈ 0.9m x 1.2m) transonic wind tunnel with 0.59% blockage as well as a 12ft (≈ 3.66m) subsonic wind tunnel with 0.05% blockage. The results obtained in the 12ft wind tunnel were found to be essentially interference free. In a study [65] of the global blockage effects in a transonic wind tunnel with a 1.5 x 1.5m test section,

two different sized models with 0.85 and 0.05% blockage ratios were considered. Tests were conducted for Mach numbers 0.3, 1.0 and 1.2 and it was concluded that, for the typical transonic wind tunnel, the larger model with 0.85% blockage should not be significantly influenced by blockage effects.

The configurations tested include the three body-strakes configurations with different span to body diameter ratios (s/D) as discussed in the previous section. The tests were conducted at three different Mach numbers namely 0.1, 0.2 and 0.3. The test conditions at the various Mach numbers are given in Table 3.

Table 3: LSWT Test Conditions

	Mach number			**Units**
	0.1	**0.2**	**0.3**	**---**
PStatic	86500	86910	88240	Pa
PDynamic	595.4	2445.1	5512.8	Pa
TTotal	294.37	298.36	304.25	K
Density	1.0256	1.0228	1.0282	kg/m^3
Velocity	34.44	69.18	102.84	m/s
Re/m	1.95	3.95	6.01	million/m

The loads of interest, normal force and pitching moment, were measured up to a pitch angle of 20° (the angles of attack vary according to the flow angularity and offsets). The model was mounted on a C-strut with the following hardware:

- Sting
- Sting extension
- "12mm K" balance
- Model consisting of 3 configurations

The Experimental setup is shown in Figure 38.

Figure 38: Model Setup in LSWT

The model parameters are listed in Table 4 with the model definitions illustrated in Figure 39.

Table 4: Wing-Body Model parameters

Parameter	Value	Unit
Total Length	19	D (calibers)
Nose length	3	D (calibers)
Strake length	11.25	D (calibers)
Aft body length	3	D (calibers)
mrc	0 (Nose tip)	D (calibers)
Model Diameter	45	mm

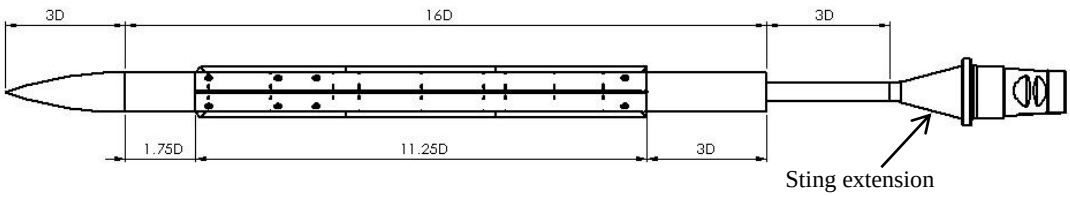

Figure 39: Model dimensions including sting extension

All configurations were tested at the same conditions i.e. the same three Mach numbers. Force and moment data was corrected for flow angularity and model offsets. The test matrix is summarized in Table 5.

Table 5: Test Matrix

Scan	Roll angle	Pitch angle	Mach Number
1	0°	-4° to 17°	0.1, 0.2, 0.3
2	180°	-20° to 4°	0.1, 0.2, 0.3

The balance measures the aerodynamic loads acting on the body in the presence of free stream air flow and yields an output in millivolts (mV), which is used to define the loads in engineering units by the process of data reduction. A detailed description of this process and the experimental procedures is given in Appendix A. The calculated balance uncertainties, based on a coverage factor of k=2, are listed in Table 6. A detailed explanation of the uncertainty calculations are also given in Appendix A.

Table 6: Balance Uncertainties

	Mach number		
Component	**0.1**	**0.2**	**0.3**
Normal Force ΔC_N	0.278	0.0677	0.0300
Pitching Moment ΔC_m	0.502	0.1220	0.0542

For Mach 0.1 the uncertainty in the centre-of-pressure $\left(\Delta X_{C_p}\right)$ is greater than 1 caliber for angles of attack below 13°, with a minimum uncertainty of 0.4 calibers at 20°. The centre-of-pressure uncertainty is reduced significantly at the higher Mach numbers. At Mach 0.2 ΔX_{C_p} exceeds 1 caliber below angles of attack of 4°, with a

minimum uncertainty of 0.09 calibers at 20°. At Mach 0.3 the maximum ΔX_{C_p} is 2.45 calibers at 0° angle of attack and less than 1 caliber for all angles above 0°.

In addition to the aerodynamic loads, surface flow visualization by means of oil flow was also carried out during the LSWT tests. A titanium dioxide-oil (TDO) mixture was applied to the surface of the body and the body was covered with a black coating. This dark background is necessary to provide contrast between the body and the white of the TDO mixture for clear visual indications of the surface flow. The flow over the model surface was photographed for selected angles of attack and this technique provided a clear indication of the flow separation lines by forming so-called "oil ridges" as demonstrated in Figure 40.

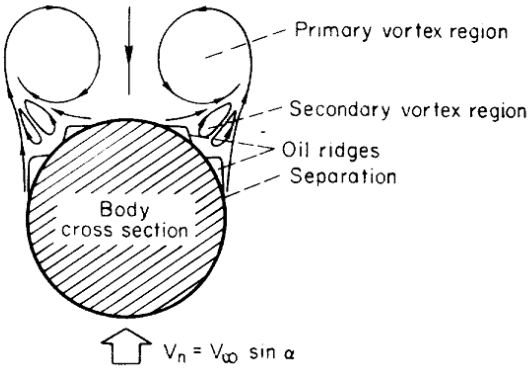

Figure 40: Schematic of oil ridges forming in the crossflow plane of a circular body [16]

These oil ridges form lines of separation in the three-dimensional set-up. The areas where the oil has been removed from the body are as a result of attached flow. The attached flow provides a high wall shear stress (τ_w), measured in Pascals (Pa), which directly related to flow velocity as follows [19]:

$$\tau_w = \mu \frac{du}{dh}\bigg|_{h=0} \tag{67}$$

where μ is the viscosity of the air, u is the velocity component in the axial direction and h is the distance normal to the body surface. For separation points, as

demonstrated in Figure 41 (d) the wall shear stress will be zero, whereas $\frac{du}{dh} > 0$ for the attached flow (Figure 41 (a)).

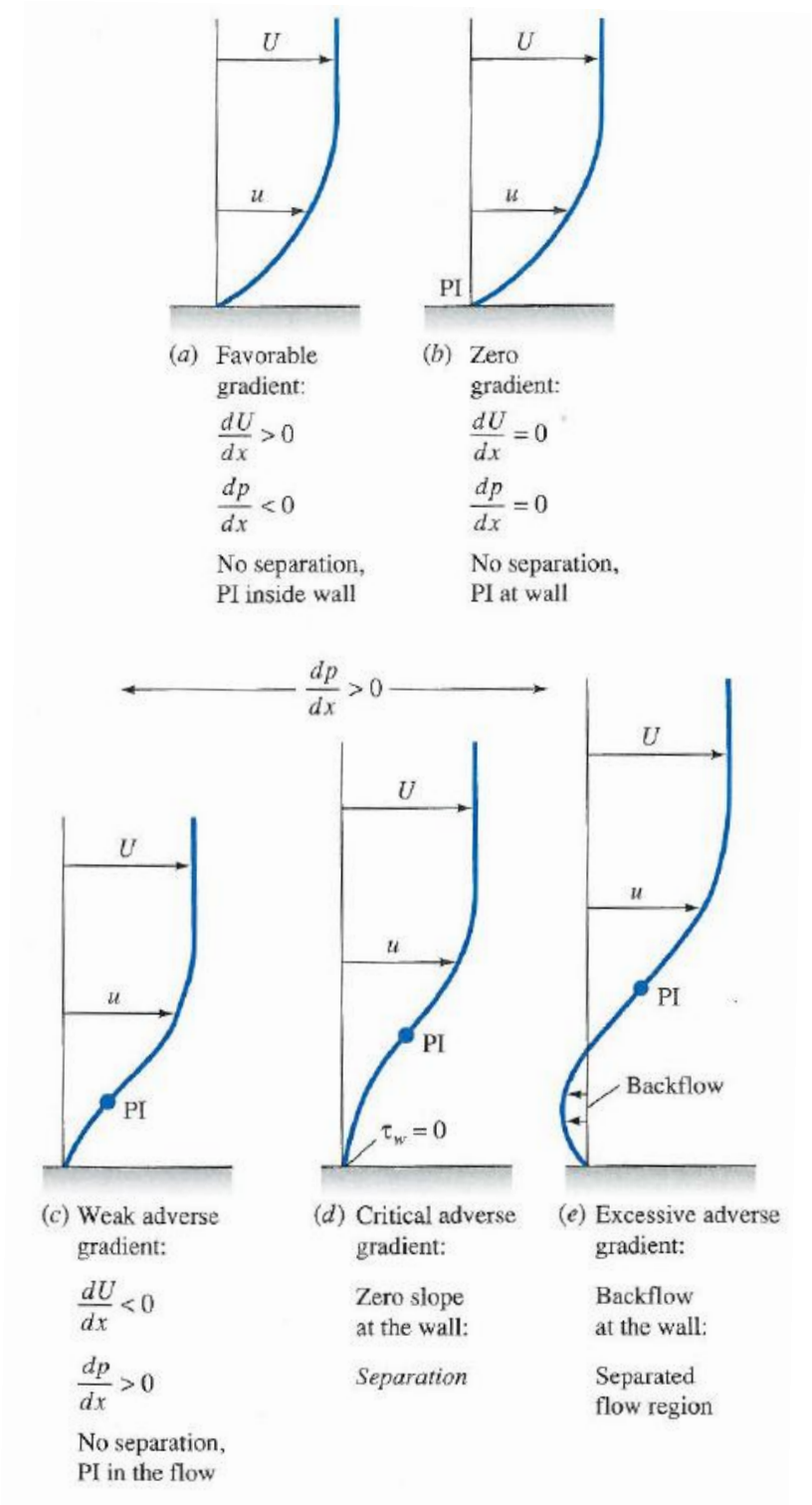

Figure 41: Effect of pressure gradient on boundary layer profiles; PI = point of inflection [19]

6.2.2. Comparison of CFD and Experimental Results

Aerodynamic Loads

The loads of interest, normal force and pitching moment coefficients, for the three configurations are shown in Figures 42 to 44. The CFD simulations correlate well with the available experimental data. However, for s/D of 1.25, there is a measurable discrepancy between the experimental and CFD normal force coefficient C_N at 20° angle of attack, though this error is small and still falls within the calculated balance uncertainties. From these results it was established that the CFD simulations predicted the lee side flow accurately and can be used as a reference for comparisons with the engineering prediction methods. Also notice that the experimental C_N indicates no Mach number dependence.

The centre-of-pressure positions X_{C_p} also show no dependence on Mach number above angles of attack of 6°. The discrepancies below 6° have been attributed to the large increase in uncertainty at very low loads. For Mach 0.1, 0.2 and 0.3 the uncertainties ΔX_{C_p} at these low angles are approximately 11.8, 5.3 and 2.5 calibers respectively. At angles of attack above 6°, ΔX_{C_p} reduces to 2, 0.2, and 0.1 for Mach 0.1, 0.2 and 0.3 respectively. The increase in uncertainty at $\alpha < 6°$ is due to the low loads experienced at these low angles: the normal force and pitching moment are in the lower 10% of the load range of the balance. Since X_{C_p} is dependent on both normal force and pitching moment, this increases the level uncertainty of X_{C_p} at these low angles of attack. Additional graphs illustrating the X_{C_p} load uncertainties may be found in Appendix A.

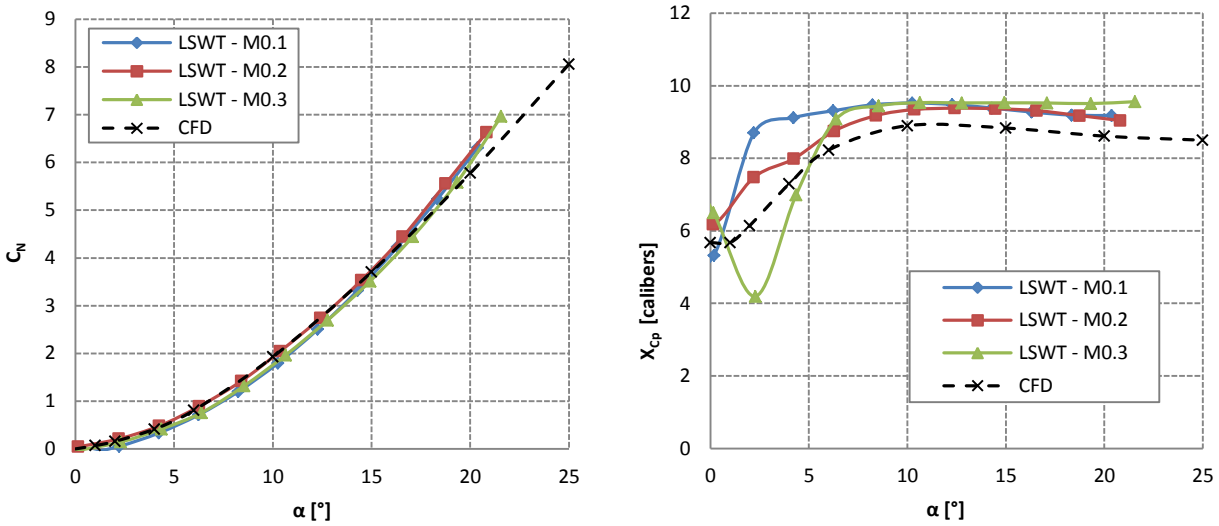

(a) (b)

Figure 42: Validation of CFD (a) C_N and (b) X_{Cp} results for s/D=1.25

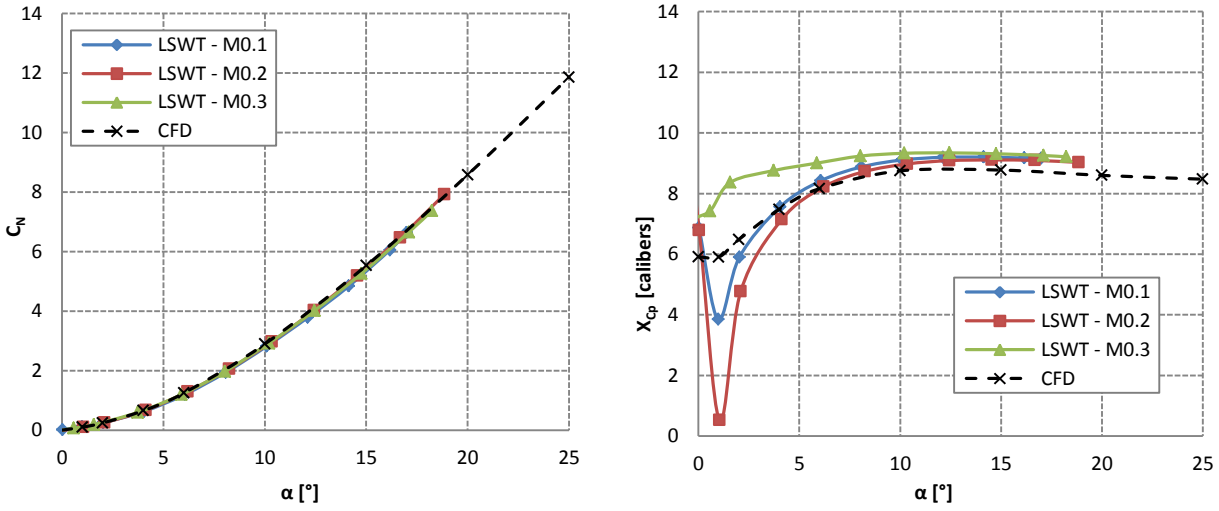

(a) (b)

Figure 43: Validation of CFD (a) C_N and (b) X_{Cp} results for s/D=1.5

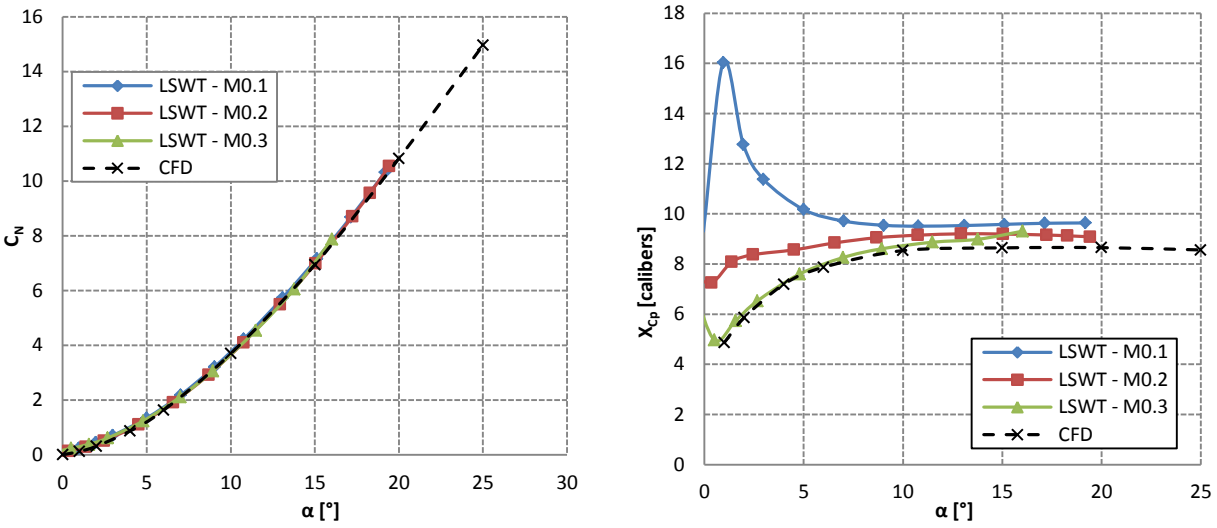

(a) (b)

Figure 44: Validation of CFD (a) CN and (b) X_{Cp} results for s/D=1.75

Flow Visualization

The flow visualization tests were limited to Mach 0.2 as the load results were already shown to have no Mach number dependence. The experimental oil flow was compared to the CFD wall shear stress (τ_w) as well as surface pathlines using the "oil flow" function in Fluent for angles of attack (α) of 10°, 15° and 20°.. The surface flow images for α = 15° are shown in this section and the additional images (for 10° and 20°) may be observed in Appendix B. A comparison of the side views are shown in Figures 45 to 47 for the three strake-body configurations and α = 15°.

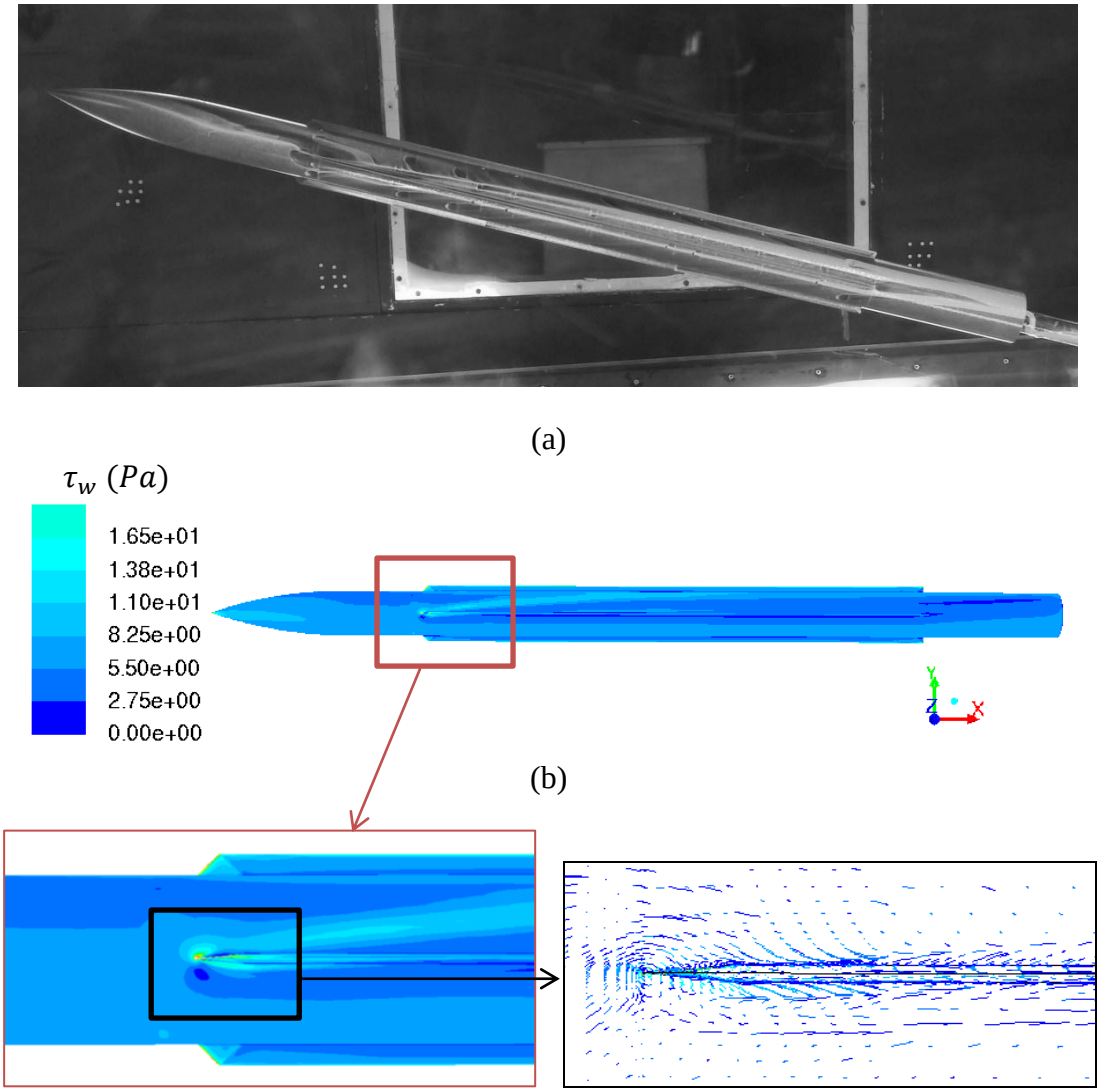

Figure 45: Side view comparison of (a) experimental surface flow and (b) CFD wall shear stress (Pa) with (c) CFD pathlines for s/D = 1.25 and α = 15°

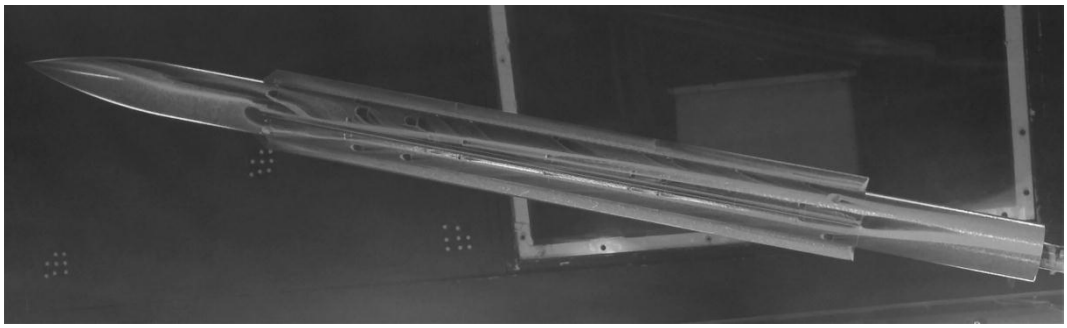

(a)

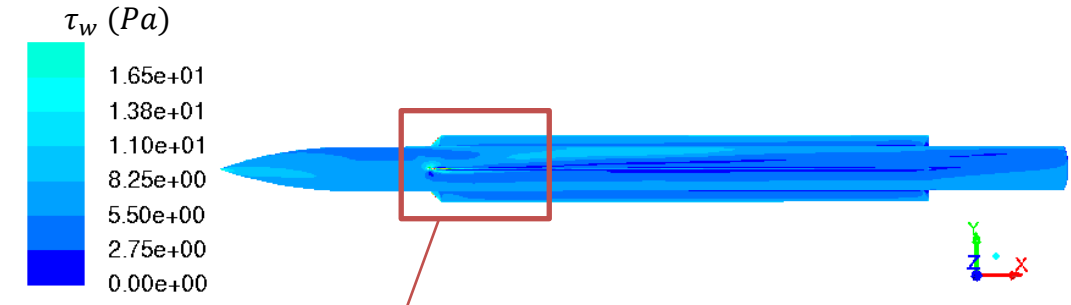

(b)

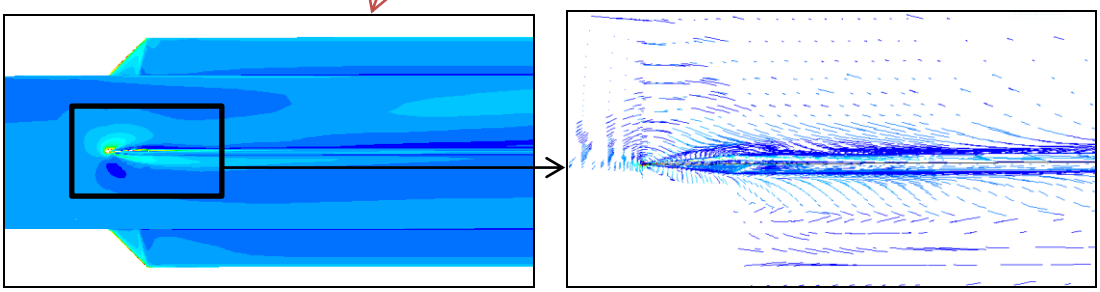

(c)

Figure 46: Side view comparison of (a) experimental surface flow and (b) CFD wall shear stress (Pa) with (c) CFD pathlines for s/D = 1.5 and α = 15°

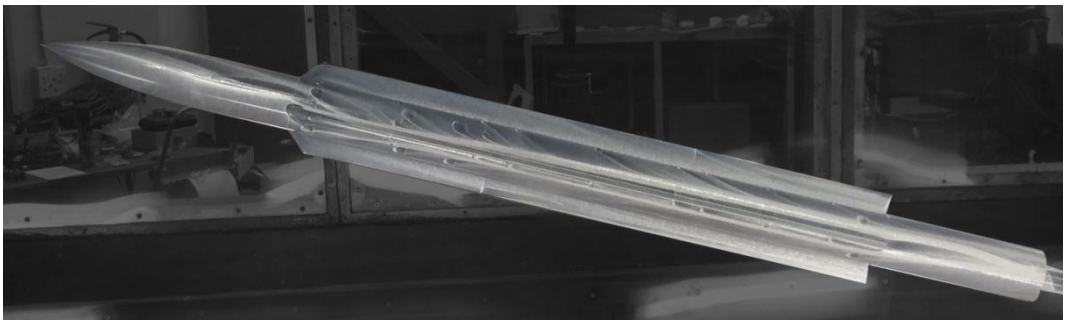

(a)

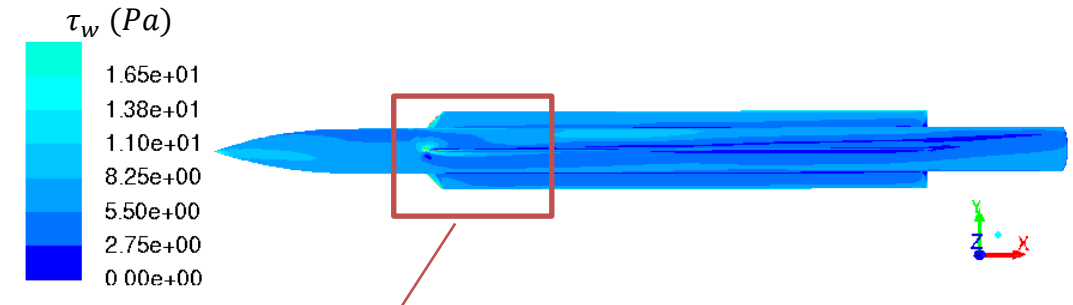

(b)

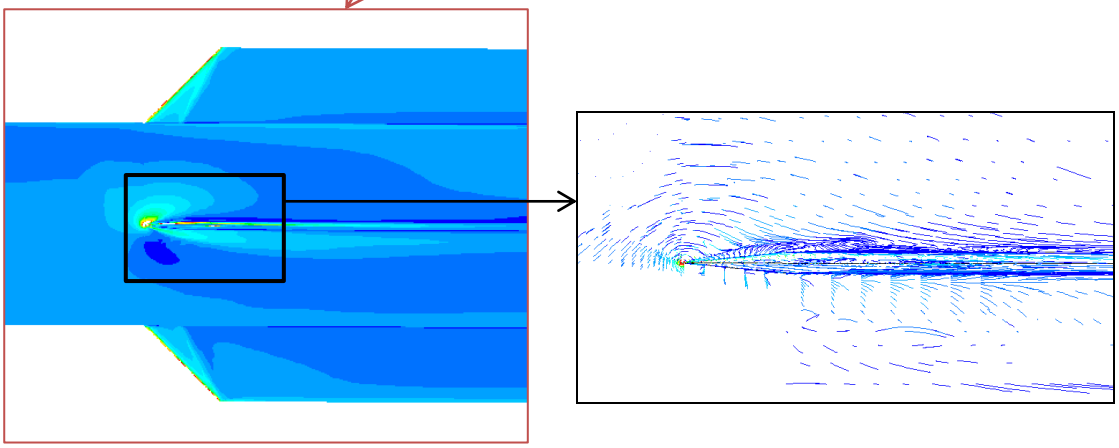

(c)

Figure 47: Side view comparison of (a) experimental surface flow and (b) CFD wall shear stress (Pa) with (c) CFD pathlines for s/D = 1.75 and α = 15°

In the experimental flow visualization, a prominent separation line is observed extending from the wing tip to the base of the body as indicated by the gathering of the titanium dioxide-oil (TDO) mixture (white contour). Intermittent cleared spots/lines are observed due to the presence of imperfections on the body surface (pin holes, screws, particles in the oil itself) which produces short wakes. These imperfections are not present in the CFD simulations, although the flow features are present in the CFD simulations as characterized by the τ_w plots. In Fluent τ_w is determined using the properties of the flow adjacent to the wall (for no-slip conditions) with the use of wall functions specific to the Spalart-Allmaras turbulence model. The contours of low shear stress ($\tau_w \approx 0$) indicate attached flow (as discussed in Section 6.2.1) which correlate well to the dark lines/contours in the experimental flow visualization that also indicate attached flow. It should be noted that the experimental photographs differ from that of the CFD images in both scale and orientation of the bodies.

Similar flow features are observed for all three configurations with slight changes in the flow separation at the nose which is as expected with the increase in angle of attack. These separation lines correspond well to that of the experimental TDO flow visualizations. Additionally, it was observed in the CFD pathlines around the strake leading edge that the separation line initially moves upward before attaching to the strake for a short distance. The separation line then travels upward along the length of the body, indicating the movement of the shed vortex sheet. This is shown in more detail in Figure 48.

To gain a better understanding of the behavior of the flow, the top views of the flow visualization are also compared. The top views of the surface flow for the three s/D configurations at $\alpha = 15°$ are given in Figures 49 to 51.

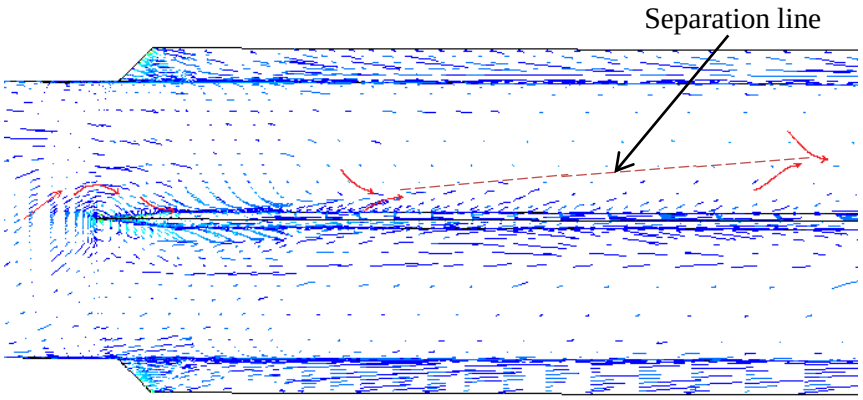

Figure 48: Separation lines indicating shed vortex sheet

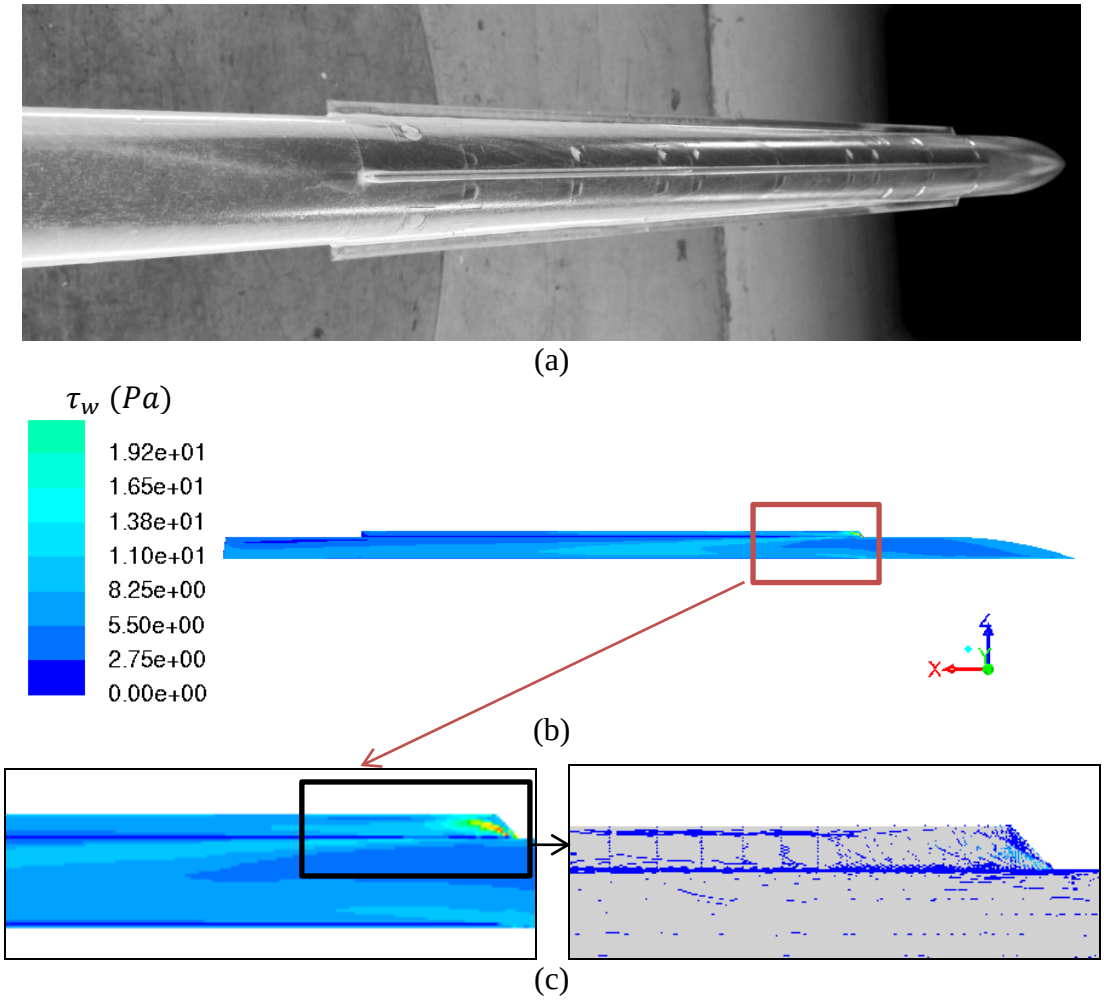

Figure 49: Top view comparison of (a) experimental surface flow and (b) CFD wall shear stress (Pa) with (c) CFD pathlines for s/D = 1.25 and α = 15°

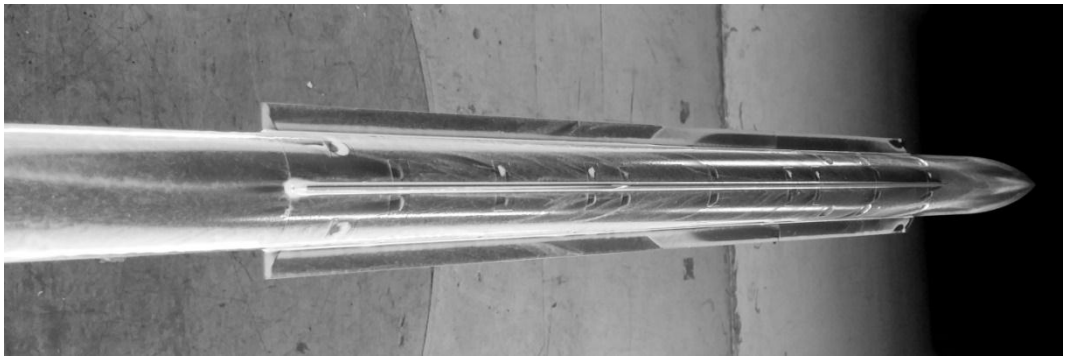

(a)

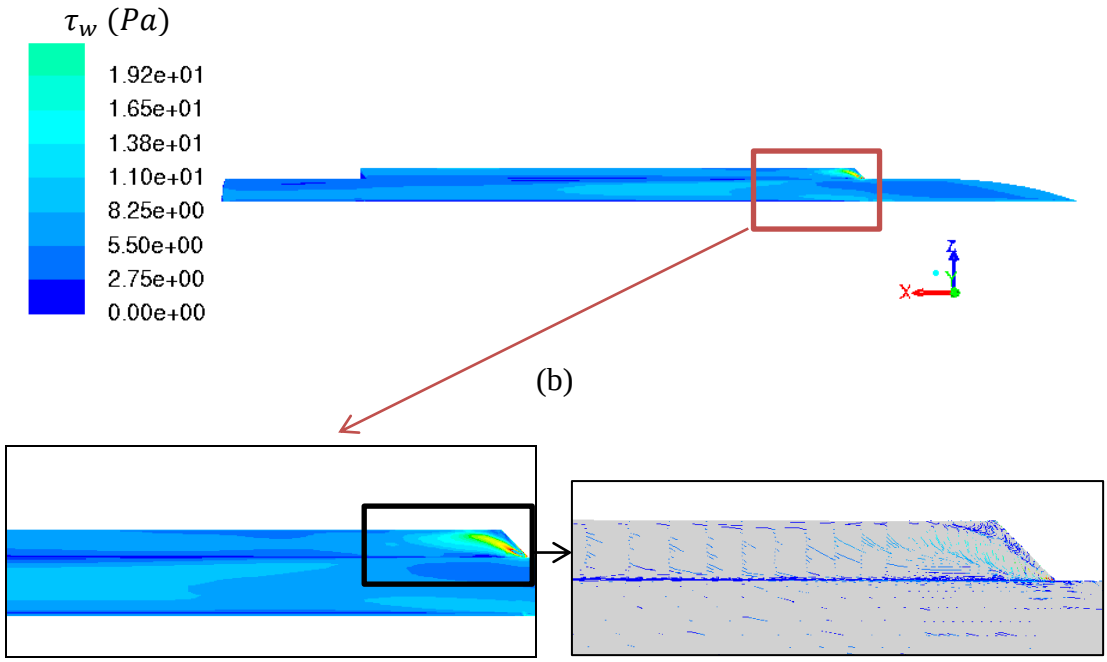

(b)

(c)

Figure 50: Top view comparison of (a) experimental surface flow and (b) CFD wall shear stress (Pa) with (c) CFD pathlines for s/D = 1.5 and α = 15°

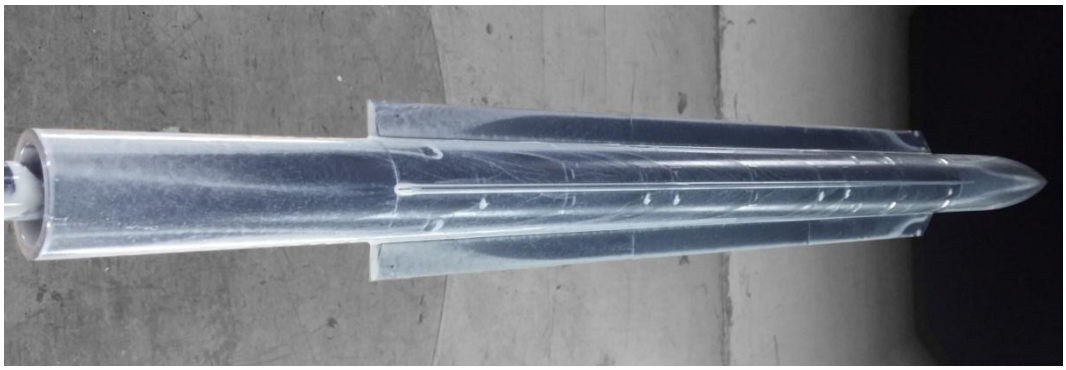

(a)

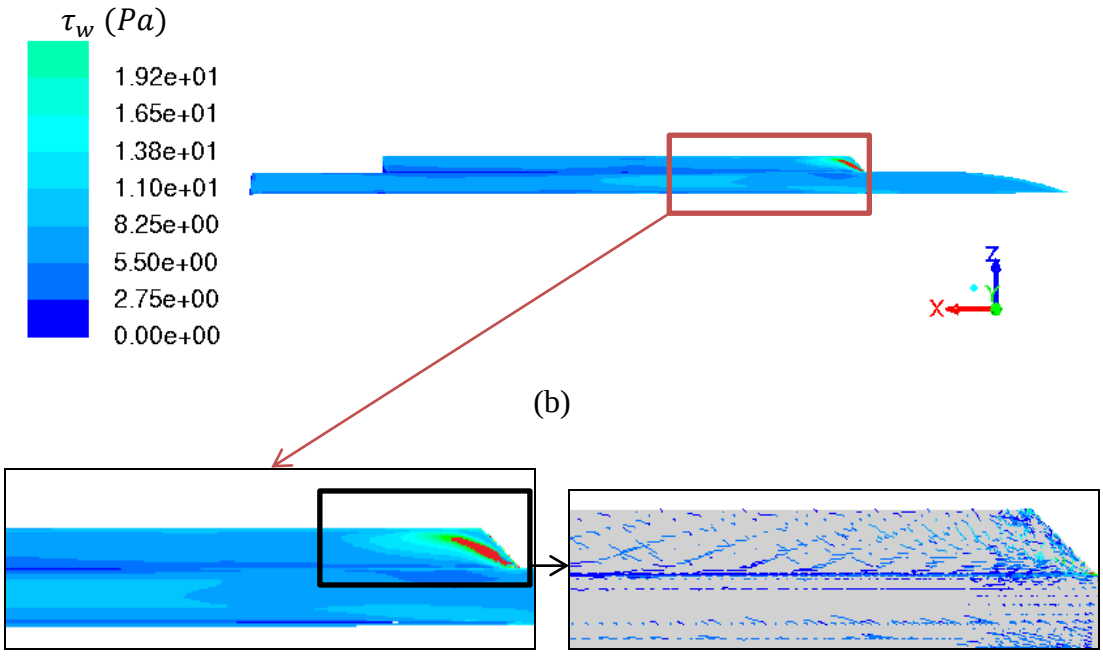

(b)

(c)

Figure 51: Top view comparison of (a) experimental surface flow and (b) CFD wall shear stress (Pa)* with (c) CFD pathlines for s/D = 1.75 and α = 15°

* Note that red filled contours represent $\tau_w > 55\ Pa$

In the experimental top view photographs the perspective of the model is significantly different from the top view plane of the CFD images. However some similarities in flow features are still observed. On the leading edge (LE) of the strakes a pattern of separation lines are observed in the experimental photographs that correspond to the CFD τ_w contours as well as the shown pathlines around the LE. These pathlines are as expected when considering wing alone theory as discussed in Section 2.2.

An interesting observation is that, in the experimental photographs, the separation lines originating at the LE move to the strake tip after the LE sweep and continues at the strake tips along the length of the strake for a distance before thickening and moving inward toward the root of the strake. As an example, the top view of the s/D=1.5 configuration at α = 15° is repeated in Figure 52 and compared to CFD pathlines at the relevant wing section with estimated separation and reattachment areas. This is typical of the results obtained at all configurations and angles of attack.

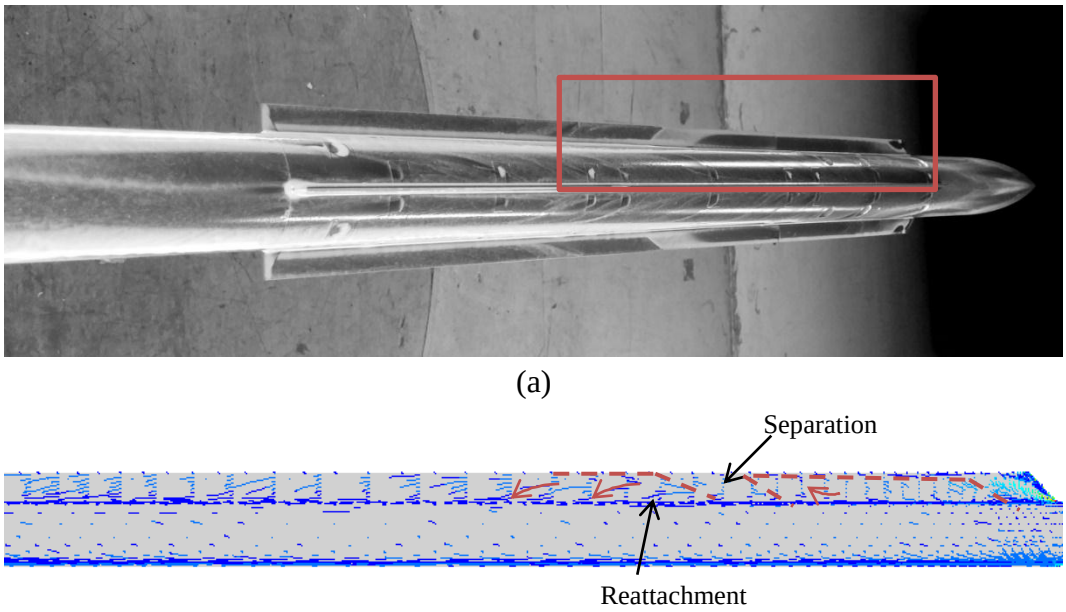

Figure 52: Top view of the (a) experimental oil flow and (b) CFD pathlines for the s/D=1.75 configuration at α = 15°

The first section of dark/cleared wing surface (Figure 52 (a)) is consistent with the forming of a primary vortex sheet where the air flows toward the strake tip away from the body and then flows upward with the flow coming from below the wing forming the visible primary separation line at the strake tip. This is demonstrated for a wing alone cross-section in Figure 11, Section 2.2.1 and Figure 53 below.

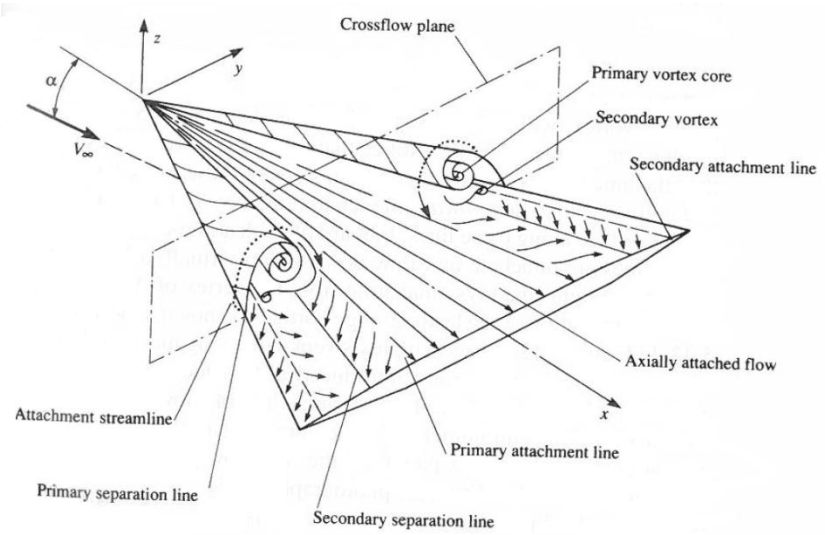

Figure 53: Leading edge separation for a delta wing [37]

In the presence of a secondary vortex, with circulation opposite to that of the primary vortex, a secondary attachment line exists with the flow moving toward the body away from the strake tip. It is thus believed that the change in separation lines on the strake surface observed in the experimental photographs can be attributed to the presence of a secondary vortex. Although the CFD τ_w contours do not demonstrate this effect as visibly, the CFD pathlines shown in Figure 52 (b) indicate a change in the surface flow direction. The air flows inward toward the body which is expected when a secondary vortex is present, although the separation and reattachment lines are not as clearly visible from the CFD oil flow as in the experimental flow visualization. The dominance of the secondary vortex flow on the strake surface

indicates that the primary vortex has separated while the secondary vortex remains attached.

The change in separation lines on the strake surface (Figure 52 (a)) for the various configurations and angles of attack, which will be referred to as the "secondary separation point", was also observed to change with increasing s/D and angles of attack:

- For a given angle of attack, the secondary separation point will move further downstream with increasing s/D and further upstream with decreasing s/D.
- For a given s/D, the secondary vortex point will move upward with increasing angle of attack. This consistent with the knowledge of flow separation with increasing angle of attack.

The additional comparisons at 10° and 20° angle of attack may be observed in Appendix B.

Vortex positions

Some experimental vortex positions were previously compiled by Tuling [1]. These tests were also conducted in the LSWT facility at the CSIR. The tests were conducted on the current wing-body combination with s/D=1.25 only, but were sufficient in validating the CFD data given that the aerodynamic loads have also been successfully validated for all three configurations. Validation of the vortex positions for s/D=1.25 is still of importance given that errors in vortex positions may occur if the vortex strengths are not correct, even though C_N and X_{C_p} are accurate. Figures 54 to 58 illustrate the comparison of the CFD vortex positions and the LSWT data for s/D=1.25.

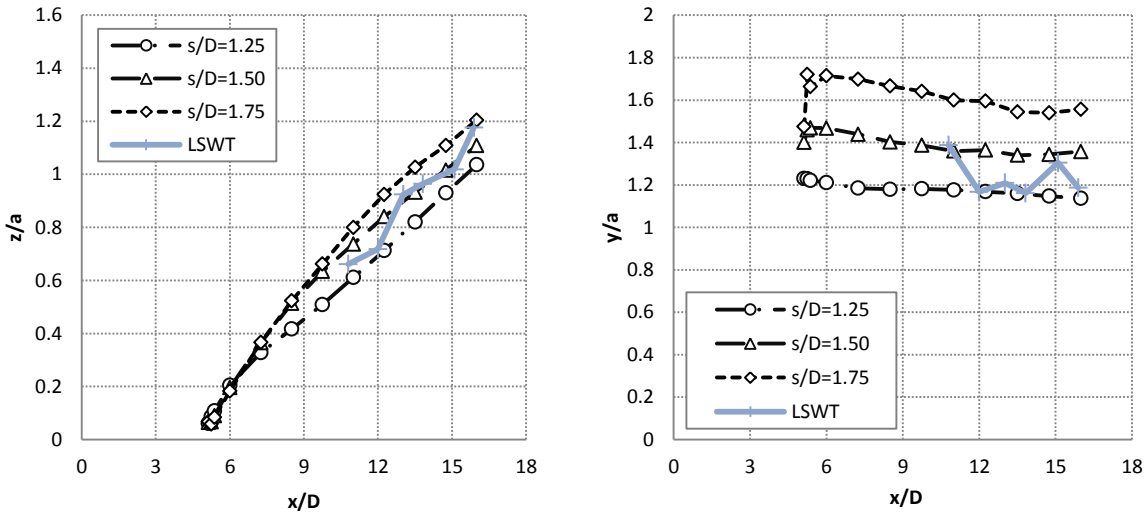

(a) (b)

Figure 54: Validation of CFD (a) vertical and (b) lateral vortex positions for α=6°

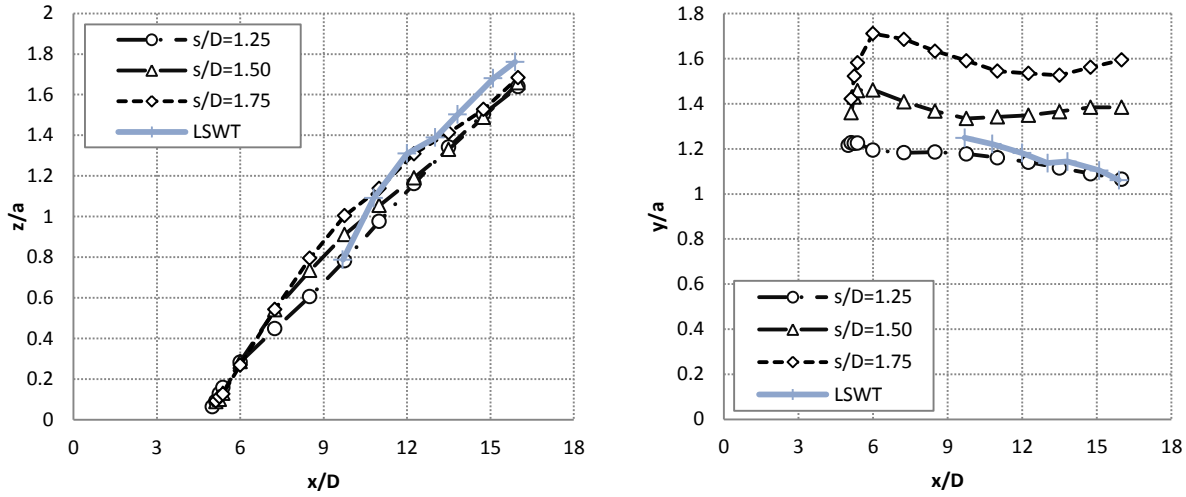

(a) (b)

Figure 55: Validation of CFD (a) vertical and (b) lateral vortex positions for α=10°

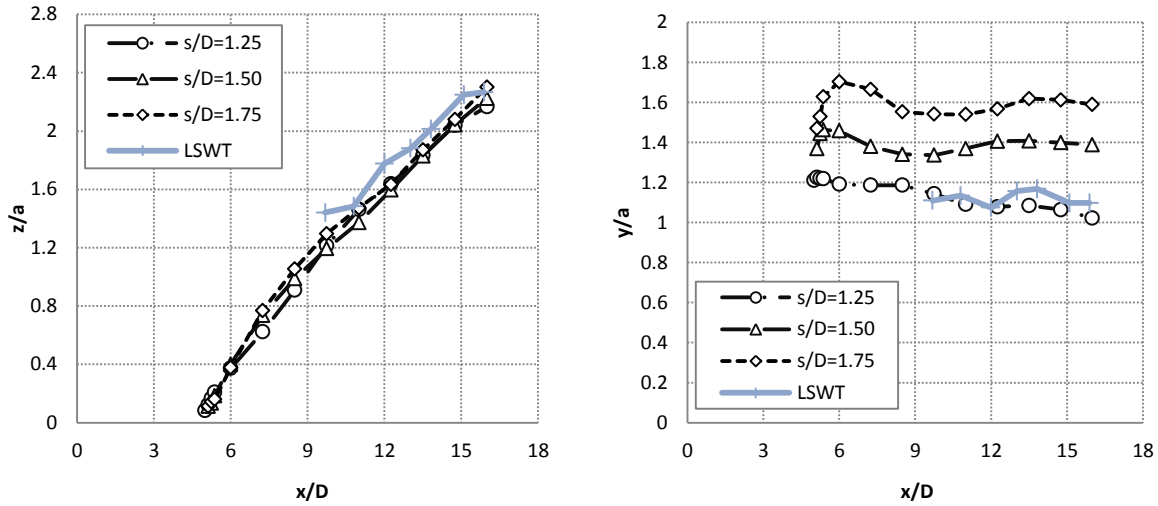

(a) (b)

Figure 56: Validation of CFD (a) vertical and (b) lateral vortex positions for α=15°

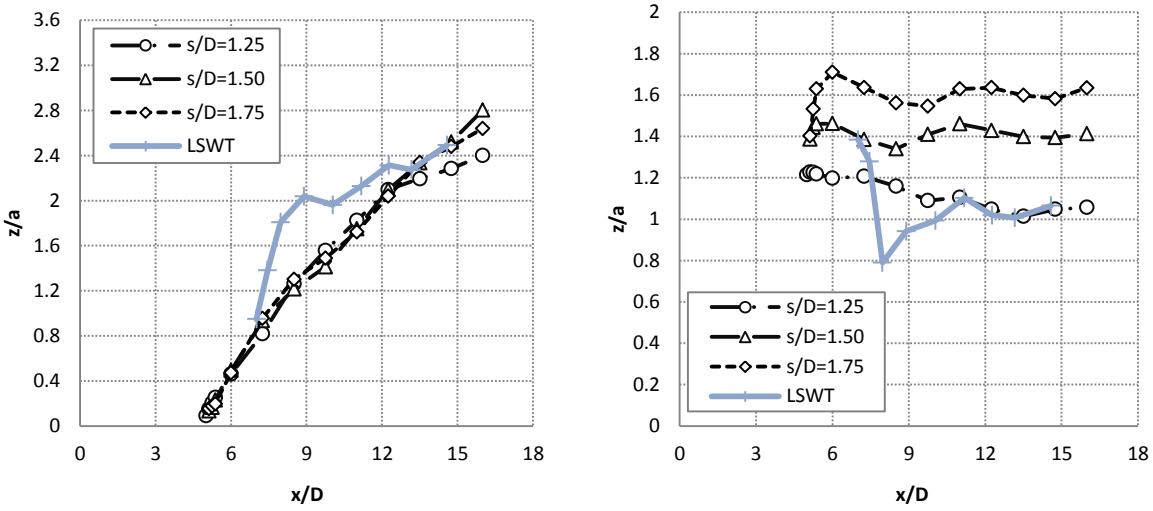

(a) (b)

Figure 57: Validation of CFD (a) vertical and (b) lateral vortex positions for α=20°

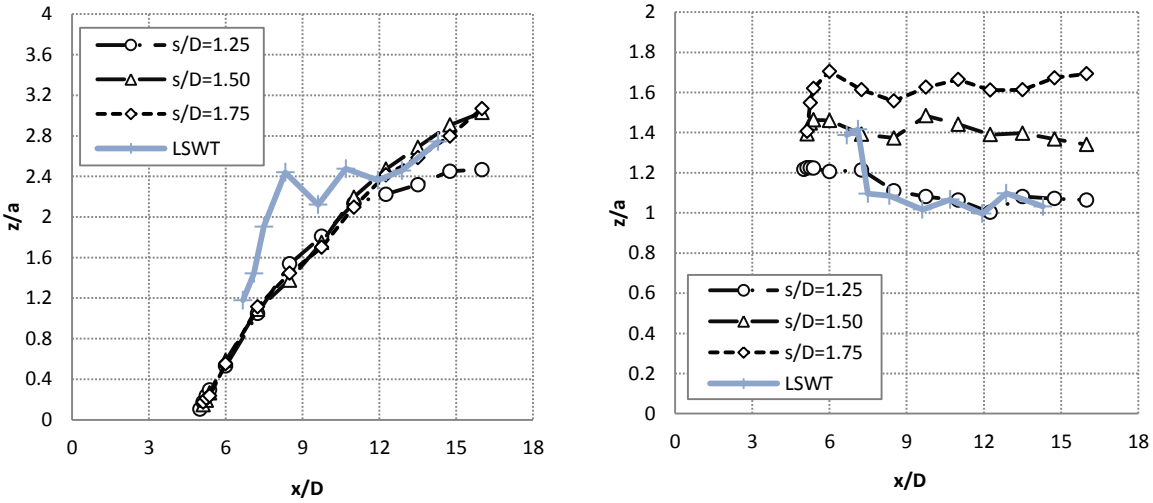

(a) (b)

Figure 58: Validation of CFD (a) vertical and (b) lateral vortex positions for α=25°

For angles of attack (α) between 6° and 15° the vertical and lateral vortex positions from the CFD simulations compare well to the LSWT data. The oscillations observed in the LSWT data at $\alpha \geq 20°$ indicates body vortex interaction, which is not captured by the CFD simulations. Despite these fluctuations, the CFD vortex positions at the higher angles of attack also correlate well to the LSWT results.

6.3. Summary

The following may be concluded for the experimental validation of CFD simulations:

- The normal force coefficients from the CFD simulations were observed to correlate very well with the experimental data.
- Despite large uncertainties in the experimental centre-of-pressure data at low angles of attack, the CFD and experimental centre-of-pressure positions showed very similar trends and good correlation of data at angles of attack above 6° for most of the test range.
- By observing surface flow visualizations from both experimental tests and CFD simulations, it was found that all the expected flow features are present in both cases.
- Despite some discrepancies between the experimental and CFD vortex positions at the higher angles of attack, good correlation was observed for the most part particularly at $\alpha \leq 10°$.

These results provided a sufficient level of confidence in the CFD data, which was considered a suitable reference for the validation of the engineering methods relevant to this study.

7. Results

As discussed previously, in the presence of body vortices, the FVM method requires an initial vortex position and strength in order to solve the relevant partial differential equations. In cases where no body vortices are present, the FVM method may be modified to exclude these vortices, therefore requiring no initial vortex input data. In this investigation both techniques were applied in order to investigate the method's dependence on these initial vortex inputs. For this study the vortex positions and strengths were extracted from the validated CFD data. It was found that body vortices occur at angles of attack from 15° to 25°, so any differences in the FVM simulations with and without external vortices are only observed at these angles of attack. In this section all the FVM method results will be compared to the validated CFD data as well as the results from the two DVM method formulations as discussed in the previous section.

It should be noted that for engineering method load predictions, the widely accepted accuracy is a percentage error of 20% or less when compared to the real loads. In this case the reference loads are represented by the validated CFD data.

7.1. Aerodynamic loads

The load results for the s/D=1.25 configuration are shown in Figure 59. The normal force coefficients (C_N) predicted by the FVM method with and without external vortices are observed to be very similar with a slight deviation at an angle of attack (α) of 20°. The DVM results show that, at $0° \leq \alpha \leq 10°$, the two DVM formulations yield very similar C_N results. Above α of 10°, the DVM method with boundary layer

(BL) modeling accurately predicts the C_N, whereas the DVM potential method shows an increase in C_N-α slope which results in the over-prediction of C_N by more than 20% compared to the CFD data.

The centre-of-pressure positions (X_{C_p}) predicted by the FVM method (both with and without body vortices) correlates very well with the CFD data, with full scale errors (hereafter referred to simply as 'error') below 10% over the α range. Above 6° the FVM method predicts that X_{C_p} is further forward (towards the nose) when compared to the CFD. For this configuration the exclusion of body vortices (at $15° \leq \alpha \leq 25°$) yields less accurate X_{C_p} results, predicting X_{C_p} further forward than the FVM simulations which include body vortices. The X_{C_p} results for the DVM potential method are well predicted up to α of 10°, while predicting that X_{C_p} lies further backward than that of the CFD data at $10° \leq \alpha \leq 25°$ with errors below 8%. The DVM method with BL modeling predicts X_{C_p} much further back (away from the nose) compared to the CFD data for $0° \leq \alpha \leq 10°$ with errors over 40%. At $\alpha > 10°$ the DVM BL method predicts the X_{C_p} slightly more forward than that of the CFD data with errors below 10%.

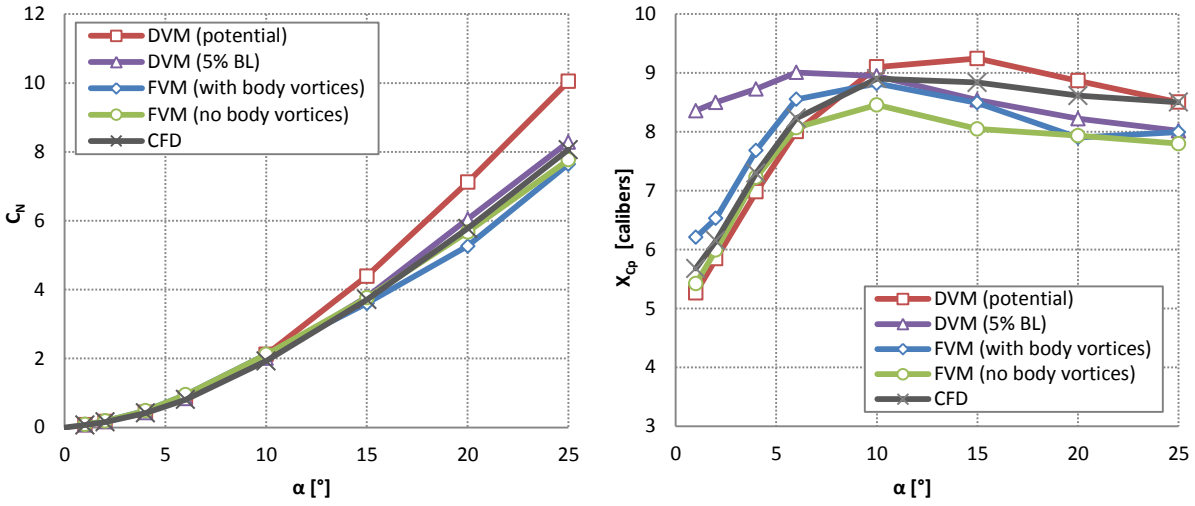

(a) (b)

Figure 59: (a) Normal force coefficient C_N and (b) centre-of-pressure position X_{Cp} comparison for prediction methods for s/D=1.25

Figure 60 shows the load results for the s/D=1.5 configuration. For all engineering calculations C_N is observed to be well predicted up to α of 10°, with the FVM method being the least accurate at $\alpha \leq 10°$. Above 10° the FVM predictions with body vortices shows a decrease in the C_N-α slope, under-predicting C_N by less than 20%. For the FVM method in the absence of body vortices C_N correlates fairly well to the CFD data with errors less than 10% at $\alpha \geq 10°$. When compared to the CFD data, the error of C_N as predicted by the DVM potential method is less than 10% for all angles of attack, making it the most accurate prediction of C_N for the s/D = 1.5 configuration. For $0° \leq \alpha \leq 20°$ the DVM method with BL modeling under-predicts C_N with an error, compared to the CFD data, of less than 10%. At 25° the C_N-α slope decreases so that the error for C_N for the DVM BL method is 17%, which falls within the acceptable error of 20% for engineering methods.

For this configuration the FVM method without body vortices predicts X_{C_p} further back for $\alpha < 4°$ and further forward for $4° < \alpha \leq 25°$ when compared to the CFD

data. The largest error for the predictions both with body vortices occurs at α of 10° with an error of 11%. The X_{C_p} predictions for the DVM potential method predicts X_{C_p} further back compared to the CFD data below α of 6°, but predict X_{C_p} further forward above 6° with a maximum error of 8%. The DVM BL modeling method does not differ significantly from the potential formulation for $0° \leq \alpha \leq 20°$. At α of 25°, X_{C_p} is predicted to be further forward compared to the potential formulation, deviating from the CFD data with an error of 12%.

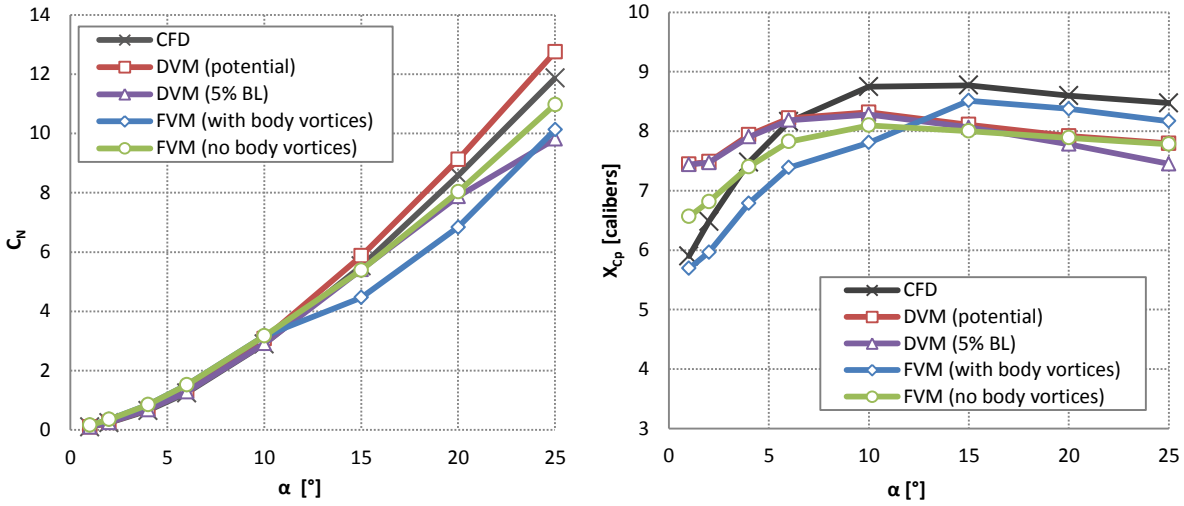

(a) (b)

Figure 60: (a) Normal force coefficient C_N and (b) centre-of-pressure position X_{Cp} comparison for prediction methods for s/D=1.5

Figure 61 shows the load results for the s/D=1.75 configuration. The two FVM simulations yield very similar C_N results with a slight deviation at α of 25°. The FVM method with and without body vortices under-predicts C_N with the only acceptable results (errors below 20%) obtained at $2° \leq \alpha \leq 15°$. The two DVM method formulations do not significantly differ from one another across the entire angle of attack range with errors below 10% compared to the CFD C_N.

For this configuration all engineering methods predict X_{C_p} further back for $\alpha < 6°$. Above 6° the FVM method without body vortices and both DVM formulations yield approximately the same X_{C_p} results. For these methods X_{C_p} is predicted further forward for $6° < \alpha \leq 25°$ when compared to the CFD data, all with errors below 10%. The most accurate X_{C_p} results are obtained with the FVM method with body vortices, which shows good correlation with CFD for $6° < \alpha \leq 25°$.

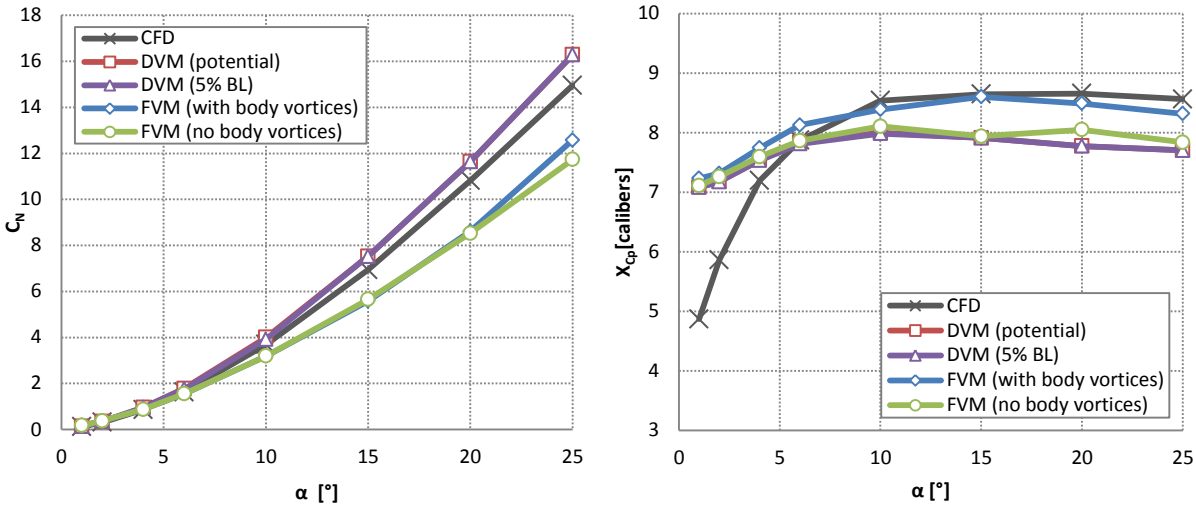

(a) (b)

Figure 61: (a) Normal force coefficient C_N and (b) centre-of-pressure position X_{Cp} comparison for prediction methods for s/D=1.75

7.2. Vortex positions

The vortex positions presented in this section are limited to two representative angles of attack namely 10° and 20°. The trends at these angles are typical for the angles assessed. The additional results are illustrated in Appendix C. The normalised vertical (z/a) and lateral (y/a) vortex positions are plotted against axial positions in calibers (x/D). Only wing vortices form part of this investigation and were investigated at angles of attack from 6° onwards. Since body vortices are only specified at $\alpha \leq 15°$,

the graphs for 6° and 10° will contain only one curve representing the FVM method. Vortex positions are presented for both the DVM potential and BL methods.

Figures 62 and 63 show the representative vortex positions for the s/D=1.25 configuration. At $\alpha \leq 10°$ the CFD vortex positions show that the vortices originate at the wing leading edge, move away from the body vertically and moves inward toward the body laterally with increasing axial position (x). The FVM method predicts the vertical vortex positions much further away from the body compared to the CFD data with errors exceeding 20%. The lateral vortex positions predicted by the FVM method correspond well to the CFD data with a maximum error of 6%. The vertical positions predicted by the DVM method are much closer to the body whilst the lateral positions show the vortex moving away from the body. The potential and boundary layer (BL) DVM formulations predict similar trends although their results differ in absolute value. While the DVM BL method seems to be the most accurate between the two formulations, errors exceed 30% at various axial stations with maximum errors of over 60%.

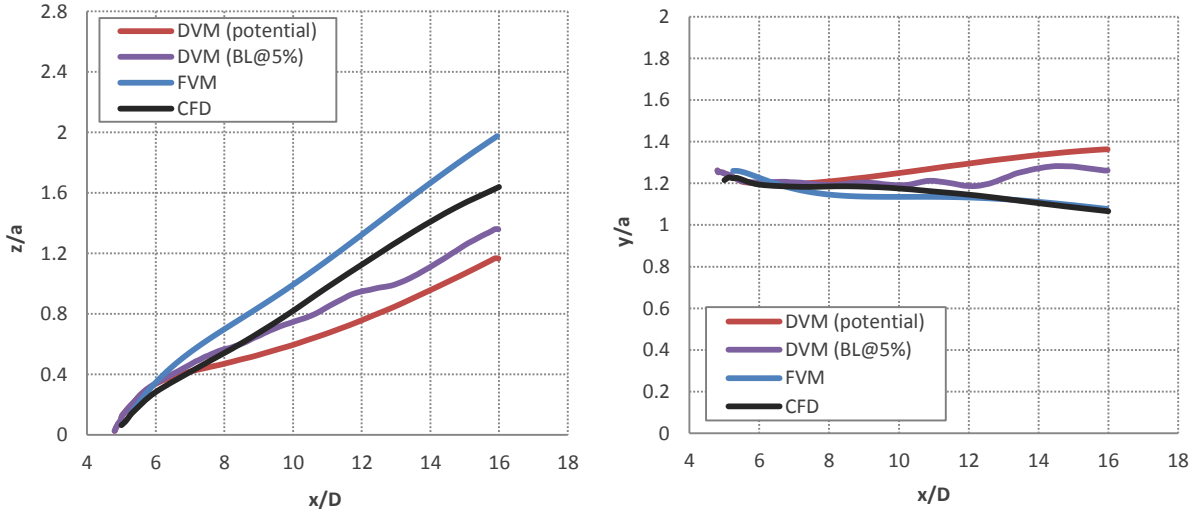

(a) (b)

Figure 62: (a) Vertical and (b) lateral vortex positions for α=10° and s/D=1.25

At $15° \leq \alpha \leq 25°$ (Figure 63) the FVM method with body vortices predicts a "corkscrew-like motion" of the vortex, illustrated by the oscillations of the vertical and spanwise (lateral) position curves with short periods and high amplitudes. This is in contrast to the CFD vortex for which oscillations with a much larger period and low amplitude is observed. This motion is due to the interaction of the body vortex; the strake and body vortex spiral around one another in this corkscrew-like fashion as shown in Figure 64. The FVM method without body vortices does not predict a corkscrew-like rotation of the wing vortex as there is no body vortex interaction. The lateral vortex position trend correlates reasonably well to that of the CFD data .

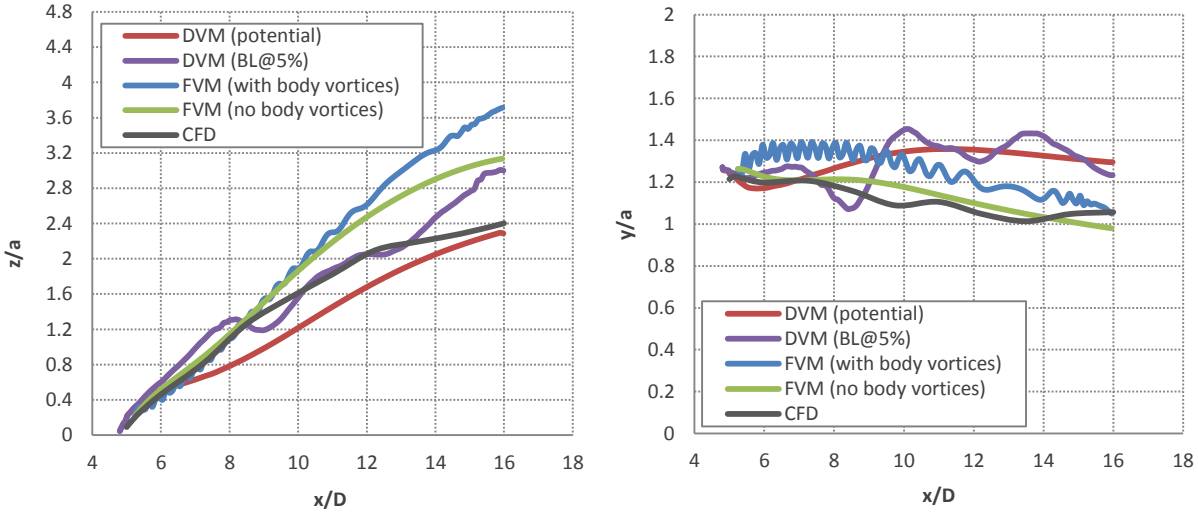

(a) (b)

Figure 63: (a) Vertical and (b) lateral vortex positions for α=20° and s/D=1.25

The DVM BL method predictions also show signs of corkscrew-like motion, although the observed oscillations are less regular than that of the FVM method. No oscillations are observed in the DVM potential method predictions and the vertical vortex positions correlate well with that of the CFD, although the lateral positions are predicted further away from the body compared to the CFD data.

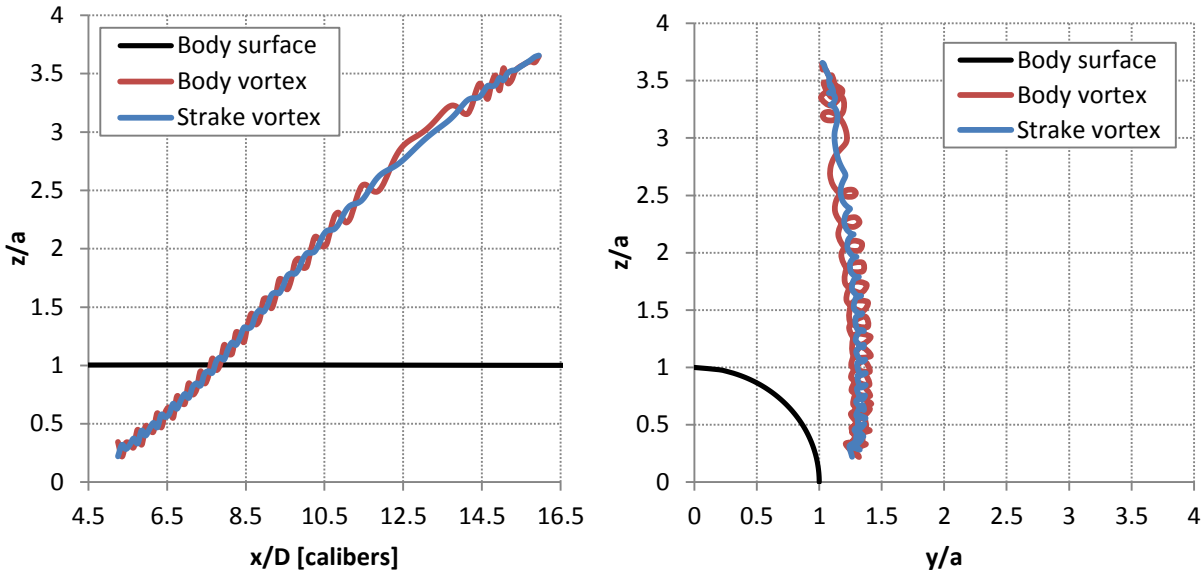

(a) (b)

Figure 64: Body and strake vortex interaction for α=20° and s/D=1.25

Figures 65 and 66 show the vortex positions for the s/D=1.5 configuration for angles of attack of 10° and 20° respectively. At $\alpha \leq 10°$, the vortex positions predicted by the FVM method do not correspond well to the CFD data. The FVM method is the least accurate with errors over 40% for the larger portion of the body length. The DVM potential and BL vertical vortex positions correlate well to the CFD data with vortices predicted to be slightly nearer to the body surface. The lateral vortex positions are predicted to be further away from the body compared to the CFD data, with errors below 20%.

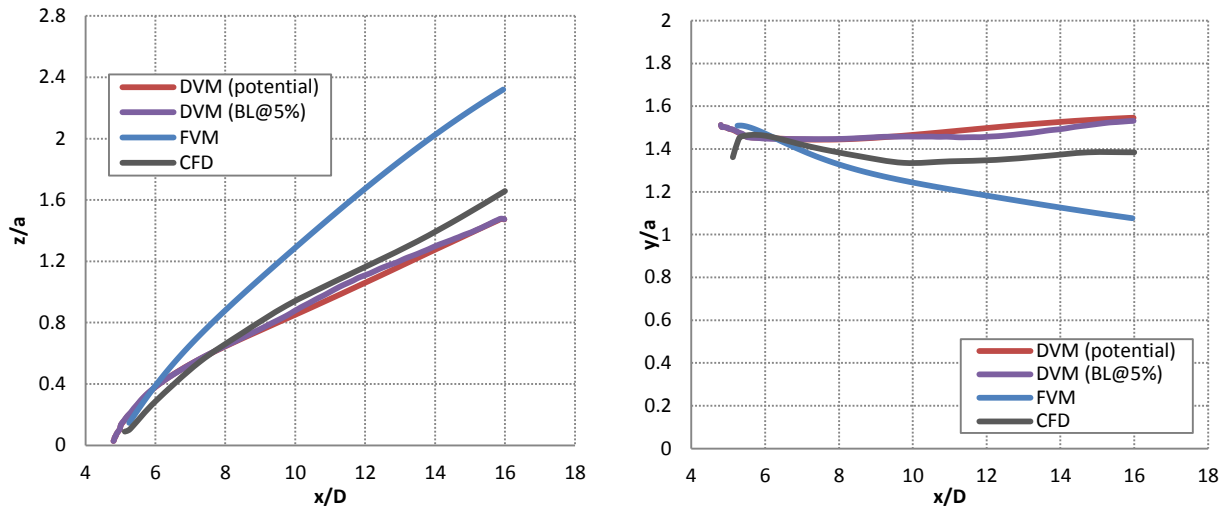

(a) (b)

Figure 65: (a) Vertical and (b) lateral vortex positions for α=10° and s/D=1.5

At $15° \leq \alpha \leq 25°$ the FVM method with body vortices again predicts a corkscrew-like motion for the interaction between the strake and body vortices and deviates the most from the CFD data. At this s/D ratio the observed oscillations, especially for positions in the spanwise direction, have an increased period as well as amplitude when compared to the smaller ratio of 1.25. Again no corkscrew-like motion is observed for the FVM method without body vortices, although the predicted vortex positions do not correlate well with the CFD data. As with the lower angles of attack, the DVM method gives a more accurate prediction of the vortex trajectories, deviating from the CFD data by less than 16% at $x/D \geq 6$. For the lateral vortex positions the DVM BL seems most accurate although the DVM potential method also yields results with errors less than 20% compared to the CFD data.

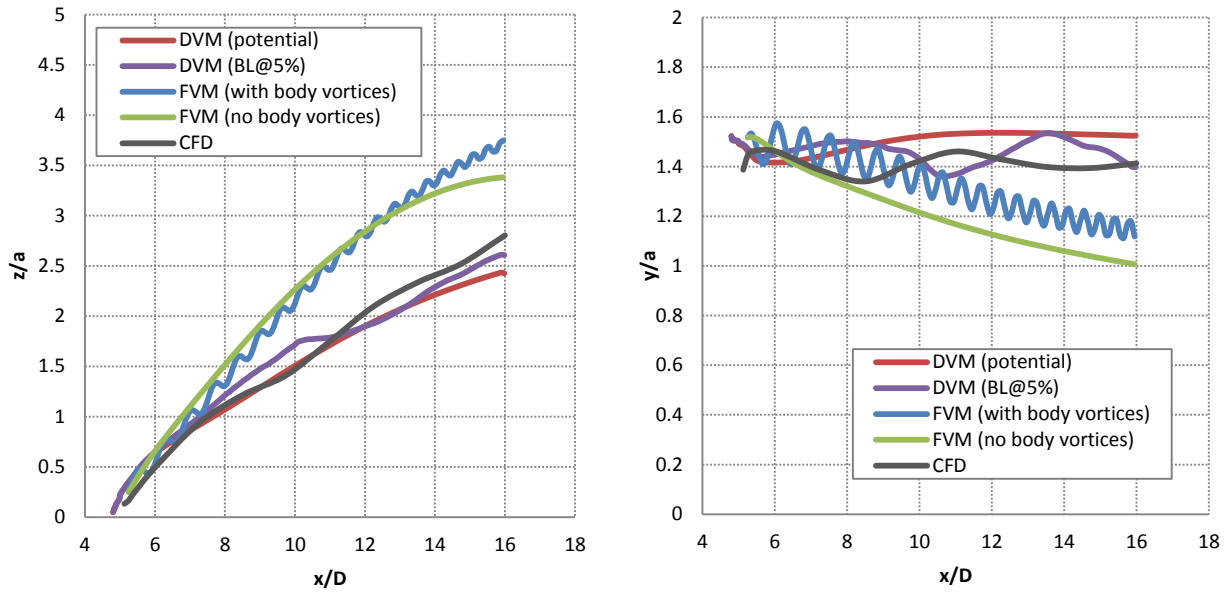

(a) (b)

Figure 66: (a) Vertical and (b) lateral vortex positions for α=20° and s/D=1.5

The vortex positions for s/D = 1.75 and α of 10° and 20° are shown in Figures 67 and 68 respectively. The FVM method again predicts the vertical vortex positions to be much further away from the body compared to the CFD data for $\alpha \leq 10°$. The DVM potential and BL vertical vortex positions for this configuration also correlate well to the CFD. As with the previous configuration, the lateral vortex positions are predicted to be further away from the body compared to the CFD data with errors over 40% at $x/D \geq 6$. These large errors occur due to the CFD vortex originating much closer to the body in the spanwise direction (y/a) at approximately 1.4 calibers. The DVM method instead predicts that the vortex originates at the strake tip which is at 1.75 calibers.

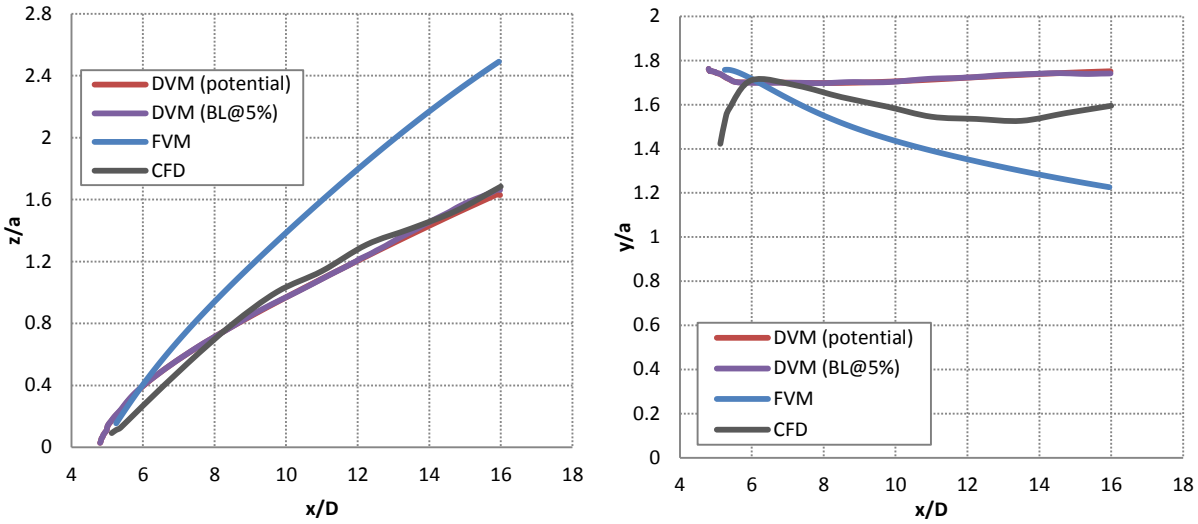

(a) (b)

Figure 67: (a) Vertical and (b) lateral vortex positions for α=10° and s/D=1.75

Similarly to the previous configuration, the FVM method with body vortices at $15° \leq \alpha \leq 25°$ and s/D=1.75 predicts a corkscrew-like interaction between the body and strake vortices. The corkscrew structure again has an increased period and amplitude at this higher s/D ratio for the FVM method with body vortices. The FVM method without body vortices predict vortex trajectories that are similar to that without body vortices. For this configuration the FVM method does not predict the vortex centre with acceptable accuracy. The vertical vortex trajectories are well predicted by the DVM potential method. The DVM BL method predicts a rotational-type motion of the vortices that is less regular than that of the FVM method, but correlates better to the CFD data.

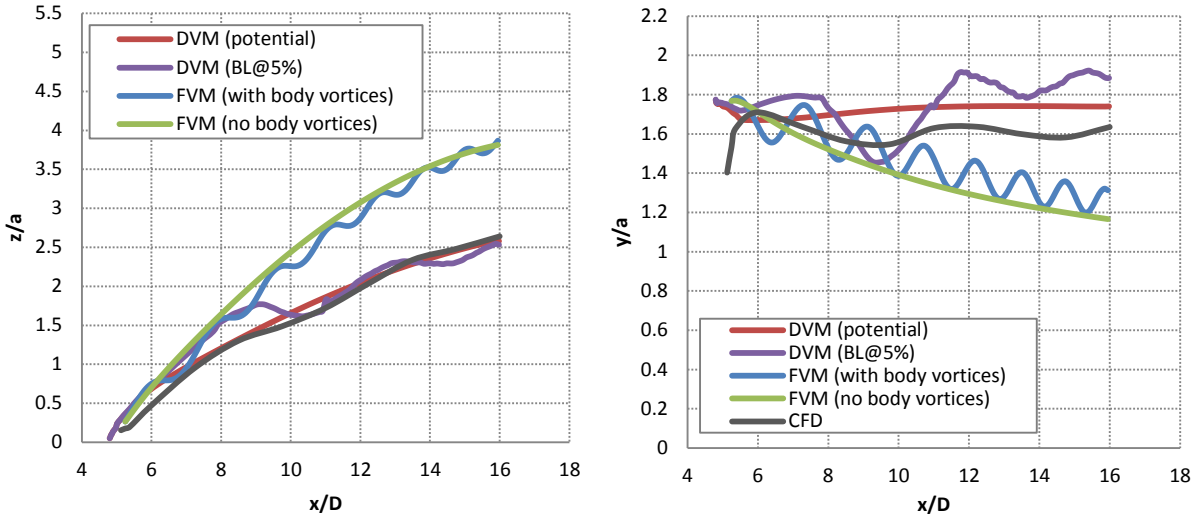

(a) (b)

Figure 68: (a) Vertical and (b) lateral vortex positions for α=20° and s/D=1.75

8. Discussion

FVM Method

The main purpose of this investigation was to evaluate the applicability of the FVM method to incompressible subsonic flows with the intent of extending the method to this speed range. The method was developed and applied to supersonic flow by reference [1] for a tangent ogive slender body with strakes in a '+' orientation. The span to body diameter ratio (s/D) of 1.25 formed part of the main application (Case A in reference [1]) and the results obtained showed that the normal force coefficient (C_N) was well predicted by the method. It was found however that the centre-of-pressure position predictions are a limitation of the method at supersonic speeds. These supersonic predictions are compared to the subsonic predictions in this study in Figures 69 and 70 for s/D=1.25.

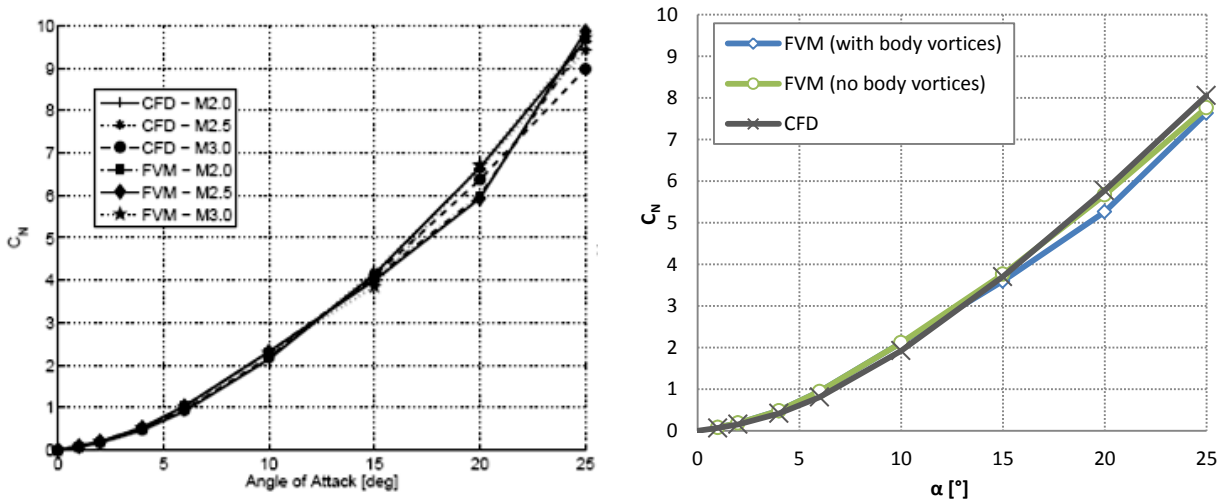

Figure 69: FVM predicted C_N results for (a) supersonic [1] and (b) subsonic flow

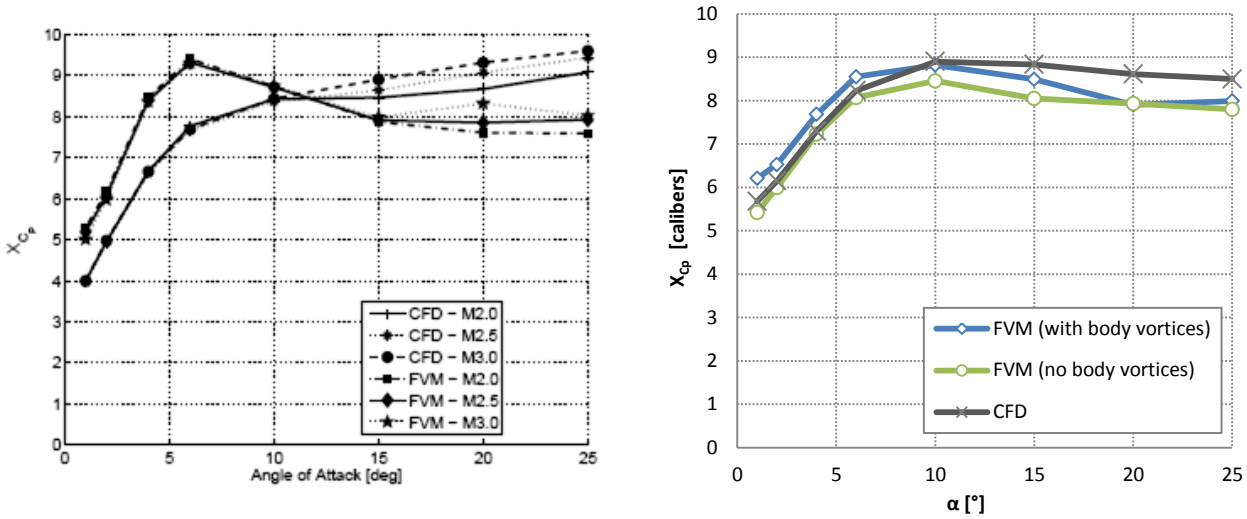

Figure 70: FVM predicted X_{Cp} results for (a) supersonic [1] and (b) subsonic flow

For the supersonic and subsonic C_N predictions with s/D=1.25 the curves show very similar trends, particularly the slight reduction in slope at α of 20°. At supersonic speeds X_{C_p} was not predicted well, although the X_{C_p} predictions improved at subsonic speeds where no compressibility effects exist.

The vortex positions for $6° \leq \alpha \leq 15°$ are well predicted by the FVM method when applied at supersonic speeds, whereas the subsonic predictions are poorer at the same angles of attack, predicting the vortices further away from the body in the vertical direction. The corkscrew-like motion of the vortices predicted by the FVM method (with body vortices) at higher angles of attack was also present in the supersonic results (see Figure 71) although to a lesser extent.

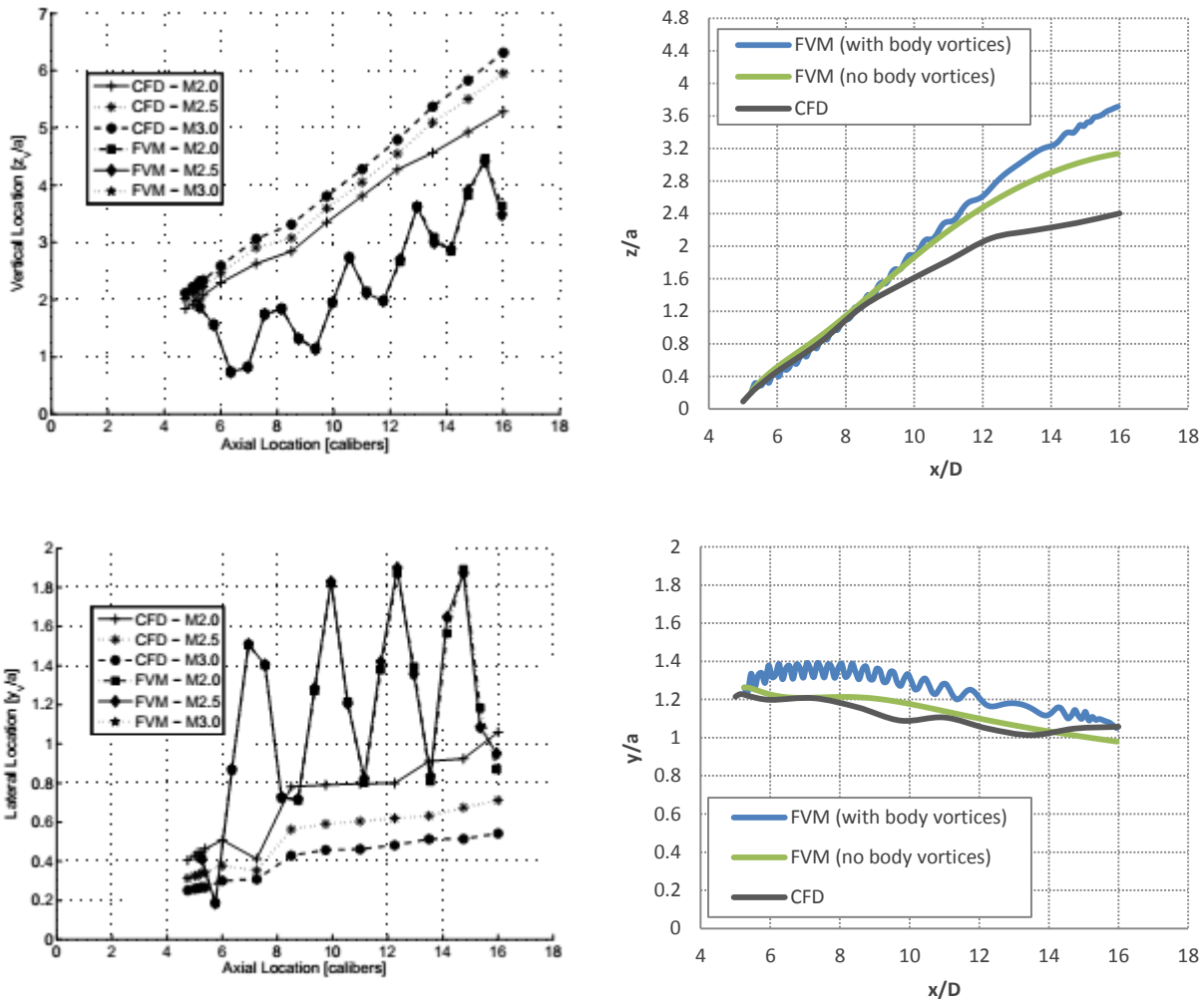

(a) (b)

Figure 71: Comparison of (a) supersonic [2] and (b) subsonic vortex positions for s/D=1.25 and α=20°

The current hypothesis as to the cause of this corkscrew motion is that the FVM method incorrectly predicts that the body vortex physically interacts with the wing vortex in this way. The simulation of body vortices are discussed in further detail later in this section.

The investigation by references [1] and [2] included four additional cases with varying configurations taken from different references. One particular case from taken from a NASA Technical Memorandum [66] has a span to body diameter ratio of 1.745, which is approximate to the 1.75 case applied in this study. The configuration

is said to represent a USA standard missile and is shown in Figure 72. The FVM method was applied at Mach 0.9 and 1.18, which is lower than the initial range developed in references [1] and [2].

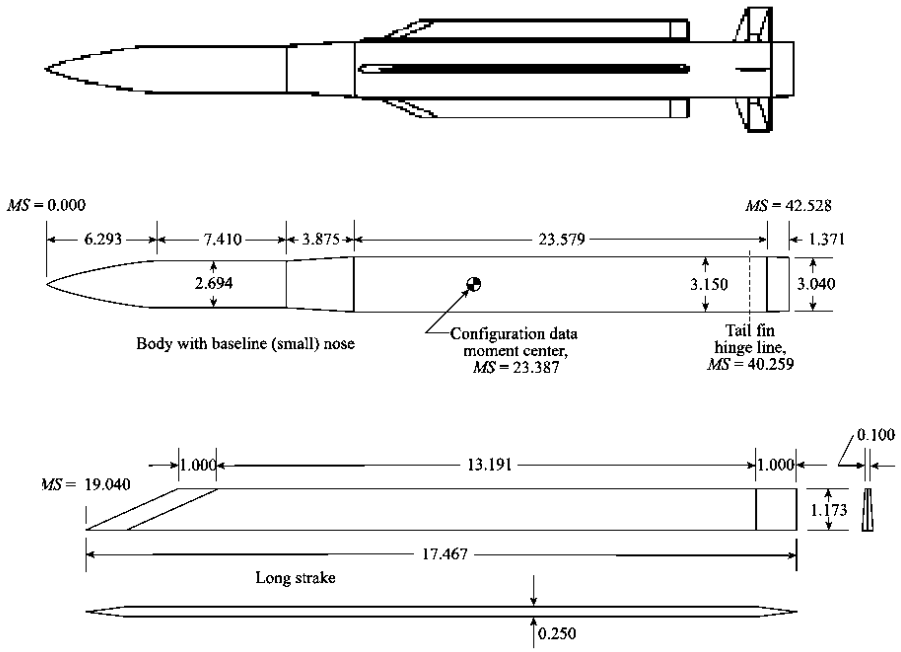

Figure 72: NASA TM-2005-213541 Triservice model configuration, dimensions in inches

It was shown that the normal force was under-predicted by the FVM method at the higher angles of attack for the NASA Triservice configuration. The centre-of-pressure was predicted to be further forward compared to the available experimental data. The results are compared to the s/D=1.75 case from this study in Figures 73 and 74.

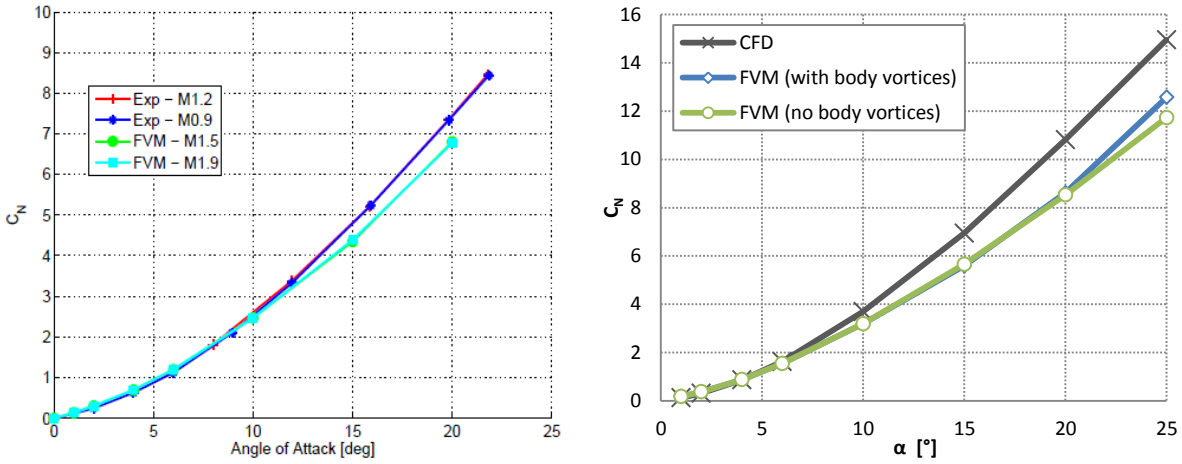

(a) (b)

Figure 73: FVM normal force predictions for (a) Mach 0.9 and 1.18 [2] and (b) Mach < 0.3 with s/D=1.75

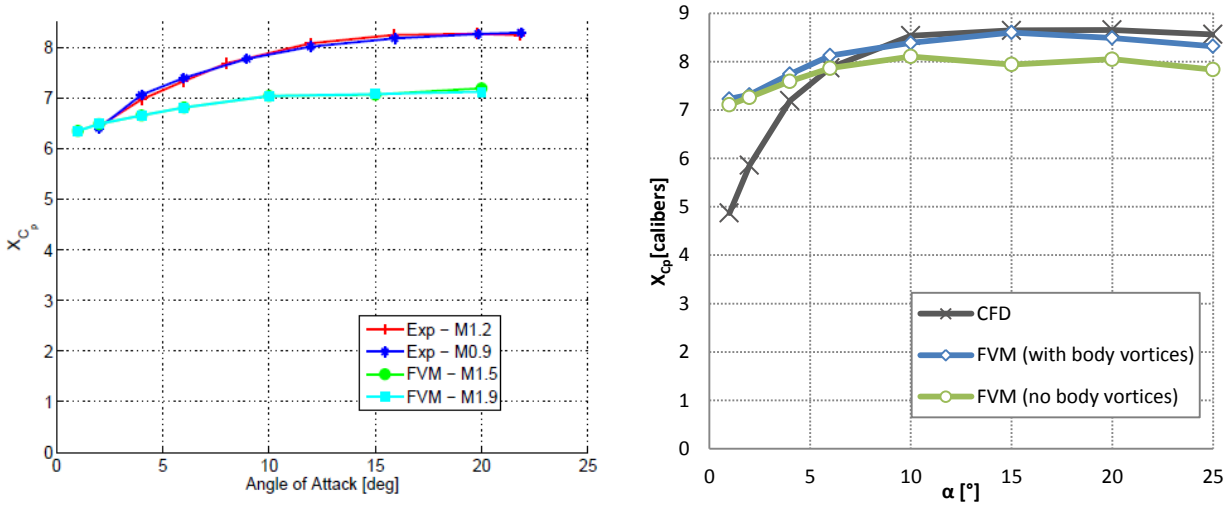

(a) (b)

Figure 74: FVM centre-of-pressure position predictions for (a) Mach 0.9 and 1.18 [2] and (b) Mach < 0.3 with s/D=1.75

From Figure 73 it was observed that the FVM method again under-predicts the C_N for the incompressible Mach numbers and s/D=1.75 configuration related to this study. The difference in C_N appears larger at the incompressible Mach numbers. The X_{C_p} predictions however show significant improvement at incompressible Mach numbers for the FVM method at $\alpha > 6°$ when body vortices are specified. For predictions with and without body vortices X_{C_p} is predicted further back when compared to the validation data. Consequently it may be stated that, for s/D of around 1.75, the FVM

prediction of C_N decreases in accuracy with decreasing Mach number. The predictions of X_{C_p} may be improved with the specification of body vortices given that the initial positions and strengths are available.

In this study it was shown that the accuracy with which the FVM method predicts the loads deteriorates as s/D increases. The vortex positions are also poorly predicted at the higher s/D ratios and angles of attack. For all three configurations analyzed in this study, some variation was observed in the FVM predictions that excluded body vortices, compared to the predictions when body vortices were specified. The y-z plane positions and strengths of the body vortices at the axial positions of the strake leading edges (x/D = 4.75) were extracted from the validated CFD simulations and specified in the FVM code for angles of attack of 15°, 20° and 25°. It was found that, if the method of extracting the vortex positions and strengths from the CFD data yield results that vary slightly with each attempt; both C_N and X_{C_p} will be influenced by this change in input data. This is demonstrated in Figure 75 for an angle of attack of 25°. For a certain initial body vortex position and strength, at any α, a variation of double the strength will result in an increase of C_N by a factor of 1.2 and X_{C_p} will be reduced by a factor of 0.96 compared to the original load (denoted by subscript 'o' in Figure 75). Halving the strength will result in a decrease of C_N by a factor of 0.97 and an increase in X_{C_p} by a trivial factor of 1.008.

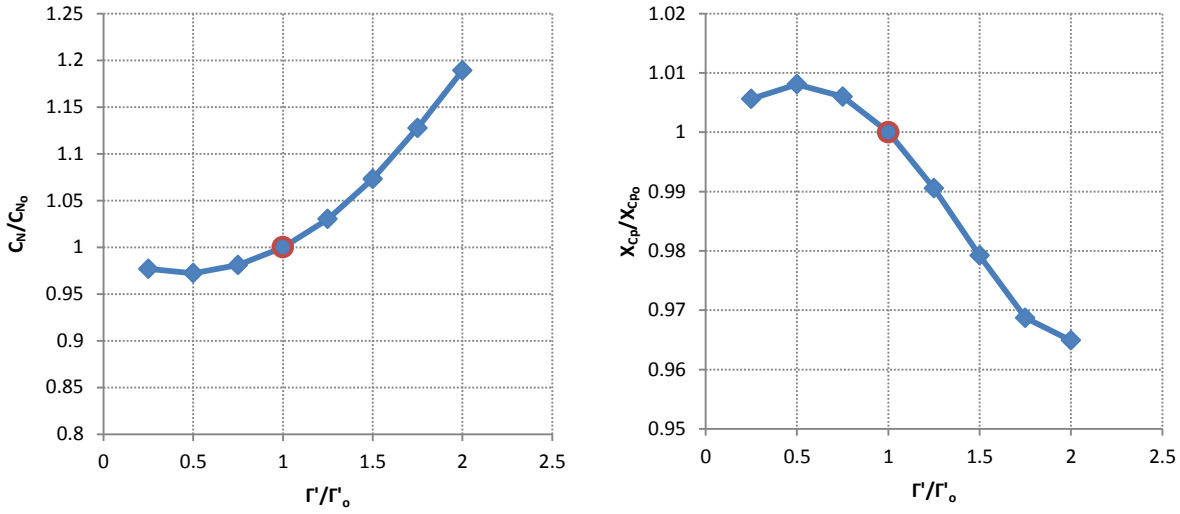

Figure 75: Factors of variation for (a) normal force and (b) centre-of-pressure position for a change in input body vortex strength at α=25°.

The strake vortex trajectories are also influenced by changes in initial body vortex strength; vortex trajectories show less interaction with the body vortex and a reduction in the corkscrew-like motion with decrease in initial vortex strength. If the corkscrew motion is in fact a result of body vortex interaction simulated by the FVM method, this reduction in the corkscrew motion with decrease in initial vortex strength is then expected as the influence of the body vortex will decrease if the vortex strength is decreased. Also, since the method does not account for the physical merging of the body and wing vortices as is expected in these types of flow (which was also captured in the CFD simulations), the continued presence of the body vortex separate from the wing vortex will also result in poor predictive capability of vortex positions.

It was found that for a certain initial body vortex position and strength at any α, a variation in the vortex positions with a constant strength where the vortices move away from the body, will result in a negligible change in both C_N and x_{Cp}. However, if the initial vortex positions were specified closer to the body, this will result in

sudden increases or decreases (depending on angle of attack) in the loads. It is therefore essential to use accurate data for the initial body vortex positions and strengths in order to ensure accurate load predictions for the FVM method. In the present study the data obtained from the CFD simulations were shown to be accurate and therefore the specified initial positions and strengths of the body vortices are acceptable.

DVM Method

The differences observed in the DVM potential and BL method load predictions (Figures 59 to 61) are significant at s/D=1.25. These differences are however observed to decrease with increasing s/D:

- At s/D=1.25, the large differences exist between the two formulations for C_N at $\alpha \geq 10°$. For X_{C_p} the potential and BL formulations yield different results across the α-range.
- At s/D=1.5, these large differences for both C_N and X_{C_p} occur later at $\alpha \geq 15$.
- At s/D=1.75, both formulations yield the same results for both C_N and X_{C_p}.

In reference [27] the DVM method (with no secondary vortex predictions) was applied to supersonic Mach numbers. These supersonic results are compared to the results from the present study in Figure 76 (SCV method results are included in the supersonic results, but the focus here is on the DVM method). It was shown that the normal force was over-predicted by the DVM method at the higher angles of attack for the s/D=1.25 configuration. In this study, at incompressible speeds, the normal

force was also over-predicted by the DVM method, with the BL formulation producing the best results.

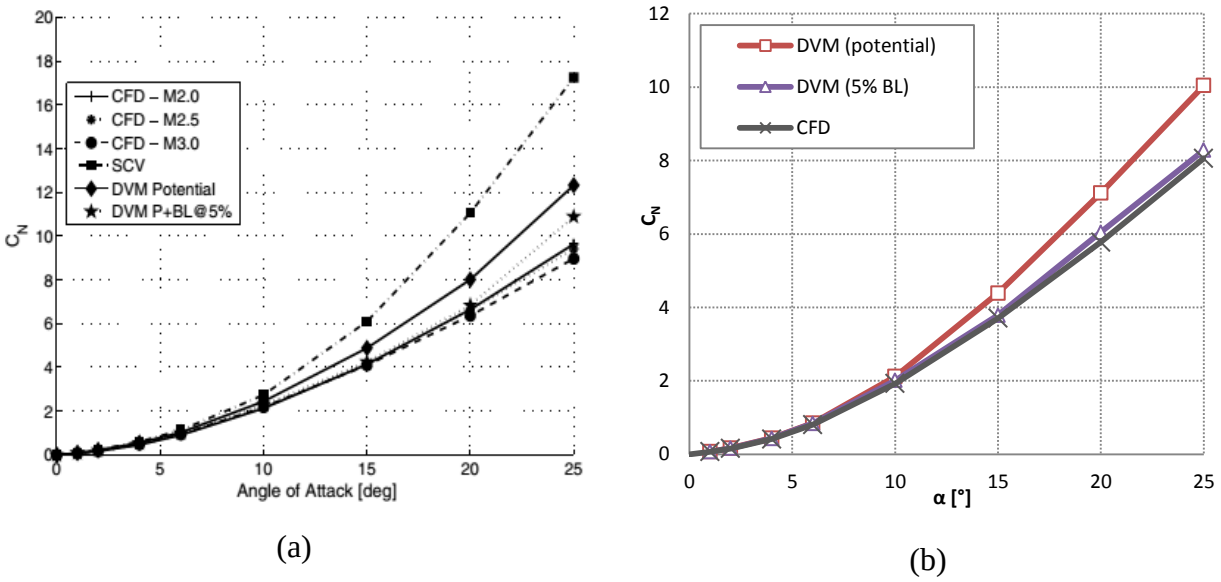

(a) (b)

Figure 76: DVM predicted C_N results for (a) supersonic [27] and (b) subsonic flow for s/D=1.25

At supersonic speeds the DVM method predicted the centre-of-pressure positions to be further downstream compared to the presented CFD data at the relevant Mach numbers. In this study, at incompressible Mach numbers, the DVM BL method predictions for s/D = 1.25 are less accurate (see Figure 77) for the centre- of-pressure positions, particularly at low angles of attack. The DVM potential method is more suitable to the prediction of centre-of-pressure positions for s/D=1.25.

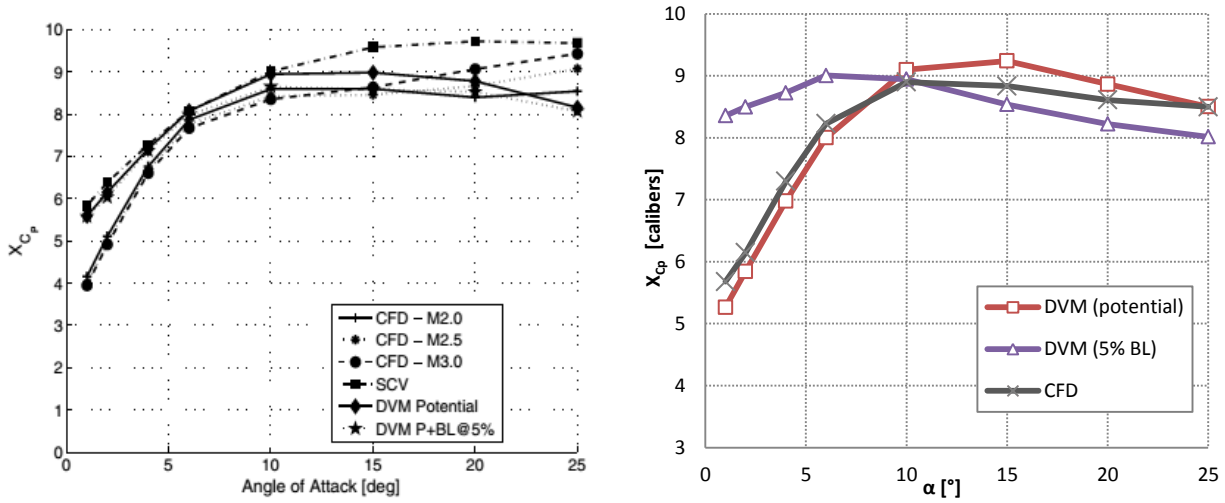

(a) (b)

Figure 77: DVM predicted X_{Cp} results for (a) supersonic [27] and (b) subsonic flow for s/D=1.25

The vortex positions predicted by the DVM method in reference [27] are poorly predicted compared to the CFD vortex positions above angles of attack of 6°. Similar results were obtained in this study as discussed in the previous section. The accuracy of the vortex position predictions tends to increase with increasing span to body diameter ratio. The loads are also predicted less accurately at the span to body diameter ratios above 1.25.

9. Conclusions and Recommendations

9.1. Conclusions

In this study the FVM method was successfully extended to subsonic incompressible speeds for applications with a span to body diameter ratio of 1.25. The method is currently limited to wing-body combinations with very low aspect ratio wings in the '+' orientation. The DVM method was added to the investigation as it is an established method with which to compare the recently developed FVM method. The following can be concluded:

- Both the FVM and DVM BL methods predict the normal force coefficient with acceptable accuracy (percentage error $\leq$ 20%) for the s/D=1.25 configuration. The centre-of-pressure positions are poorly predicted at angles of attack below 10° for the DVM BL method. The centre-of-pressure positions are, however, predicted well by both the FVM and DVM potential methods.
- Despite errors in the centre-of- pressure predictions, the FVM method showed better correlation at subsonic speeds, where compressibility effects are negligible, than the supersonic predictions in references [1] and [2].
- The FVM method load predictions decrease in accuracy at the higher span to body diameter ratios and are therefore not applicable at s/D > 1.25.
- The FVM vortex position predictions are only reasonable at $\alpha \leq 10°$ given that the vertical positions are predicted with errors over 20%, but lateral positions are very accurate with errors below 6%. Above 15° vortex positions are predicted in a corkscrew-like motion which does not accurately simulate wing vortex and is a current limitation of the method.

- The DVM method is more suitable at higher span to body diameter ratios for the prediction of loads and vortex positions.

As an engineering application, the FVM method is more suitable when compared to the DVM method for s/D=1.25 and incompressible speeds, as it has the advantage of low calculation costs whilst producing loads with acceptable accuracy (errors < 20%).

9.2. Recommendations

For the continued development of the FVM the following is recommended:

- Include compressibility effects to improve supersonic centre-of-pressure predictions.
- Improve vortex position prediction capability.
- Extending the method to higher subsonic and transonic speeds.
- Extend the method to non-zero roll angles.
- Extend the method to additional wing-body configurations.
- The numerical simulations in this study may be compared to simulations in other programs such as OpenFOAM.

10. References

1. Tuling, S. (2012) *An Engineering Method for Modeling the Interaction of Circular Bodies and Very Low Aspect Ratio Cruciform Wings at Supersonic Speeds.* PhD. Thesis submitted to the Faculty of Environment and Technology, University of the West of England. Bristol.

2. Tuling, S, Dala, L. and Toomer, C.(2013) *An Engineering Method for Modeling the Interaction of Circular Bodies and Very Low Aspect Ratio Cruciform Wings at Supersonic Speeds.* 31st Applied Aerodynamics Conference, AIAA-2.13-2823.

3. Nielsen, JN. (1988) Missile Aerodynamics. USA, NEAR Inc.

4. Vukelich, Steven R., et al. (1988) "Missile Datcom Volume 1 - Final Report." McDonnell Douglas Missile Systems Company. Ohio, AFWAL Flight Dynamics Laboratory.

5. Blake, WB. (1989) *MISSILE Datcom: Applications to Projectiles.* AIAA 89-3370. pp. 212-221.

6. Lesieutre, D., Love, J. and Dillenius, M. (1996) *High Angle of Attack Missile Aerodynamics Including Rotational Rates - Program M3HAX.* AIAA 96-3392. San Diego..

7. Lesieutre, D., et al. (2002) *Recent Applications and Improvements to the Engineering-Level Aerodynamic Prediction Software.* AIAA 2002-0275. Reno.

8. Sorrento, DP. (1998) *ONERA's Aerodynamic Prediction Code - MISSILE.* RTO MP-5.

9. *Item 86009.* Royal Aeronautical Society, ESDU. 1986.

10. *Item 89008.* Royal Aeronautical Society, ESDU. 1989.

11. *Item 83039.* Royal Aeronautical Society, ESDU. 1983.

12. Moore, FG., McInville, RM. and Hymer, T. (1995) *The 1995 Version of the NSWC Aeroprediction Code: Part I - Summary of New Theoretical Methodology.* Naval Surface Warfare Center. NSWCDD/TR-94/379. Dahlgren, Virginia.

13. Moore, FG.(1993) *State-of-the-art Engineering Aeroprediction Methods with Emphasis on New Semiempirical Techniques for Predicting Nonlinear Aerodynamics on Complete Missile Configurations.* Naval Surface Warfare Center. NSWCDD-TR-93-551. Dahlgren, Virginia.

14. Baker, WB. (1988).*Use of Semiempirical Aerodynamic Methods for Preliminary Design.* NEAR Conference on Missile Aerodynamics.

15. Krieger, RJ., Williams, JE. and Hood, RF. (1983) *A Component Buildup Aerodynamic Prediction Approach for Airbreathing Missiles.* AIAA 83-0461. Reno, Nevada.

16. Jorgensen, Leland Howard. (1977) *Prediction of Statc Aerodynamic Characteristics for Slender Bodies Alone and with Lifting Surfaces to Very High Angles of Attack.* Ames Research Center. NASA-TM-X-73,123.

17. Bryson, A. E. (1959) *Symmetric vortex separation on circular cylinders and cones.* Journal of Applied Mechanics, pp. 643-648.

18. Mendenhall, MR., Spanglor, SB. and Perkins, SC. (1979) *Vortex shedding from circular and noncircular bodies at high angles of attack.* AIAA-79-0026.

19. White, Frank M**.** (2008) Fluid Mechanics. 6th Edition. McGraw-Hill.

20. Nielsen, JN. and Kaattari, GE. (1951) *Method for estimating lift interference of wing-body combinations at supersonic speeds.* NACA RM A51J04.

21. Lugt, Hans J. (1996) Introduction to vortex theory. Maryland. Vortex Flow Press, Inc.

22. Allen, HJ**.** (1949) *Estimation of the forces and moments acting on inclined bodies of revolution of high fineness ratio.* NACA RM A9I26.

23. Mendenhall, MR. (1981) *Predicted vortex shedding from noncircular bodies in supersonic flow.* Journal of Spacecraft and Rockets, Vol. 18, pp. 385-392.

24. Allen, HJ. and Perkins, EW. (1951) *Characteristics of flow over inclined bodies of revolution.* NACA RM A50L07.

25. Hopkins, EJ. (1951) *A semiempirical method for calculating the pitching moment of bodies of revolution at low Mach numbers.* NACA RM A51C14.

26. Marshall, FJ. and Deffenbaugh, FD. (1974) *Separated flow over bodies of revolution using an unsteady discrete-vorticity cross wake.* NASA CR-2414.

27. Tuling, S., Dala, L. and Toomer, C. (2013) *Two-dimensional potential method simulations of a body-strake configuration.*, Journal of Spacecraft and Rockets. Vol. 51, No. 2, pp 468-477.

28. Jorgensen, LH. and Perkins, EW. (1955) *Investigation of some wake vortex characteristics of an inclined ogive-cylinder bodyat Mach number 2.* NACA TR 1371, pp. 857-875.

29. Jones, RT. (1946) *Properties of Low-Aspect-Ratio Pointed Wings at Speeds Below and Above the Speed of Sound.* Langley Memorial Aeronautical Laboratory.. NACA Report 835.

30. Bollay, W. (1939) *A Non-Linear Wing Theory and its Application to Rectangular Wings of Small Aspect ratio.*, Z. Angew. Math. Mech., Vol. 19, pp. 21-35.

31. Stallings, RL. Jr. (1986) *Low Aspect Ratio Wings at High Angle of Attack.* [ed.] Hemsch, MJ. and Nielsen, JN. Tactical Missile Aerodynamics.Vol. 104. American Institute of Aeronautics and Astronautics, Inc.

32. Stahl, WH. (1979). *Aerodynamcs of Low Aspect Ratio Wings.* AGARD LS-98.

33. Stallings RL. Jr. and Lamb, M. (1981) *Wing-Alone Aerodynamic Characteristics for High Angles of Attack at Supersonic Speeds.* NASA TP-1889.

34. Flax, AH. and Lawrence, HR. (1951) *The Aerodynamics of Low-Aspect_ratio Wings and Wing-Body Combinations.* Third Anglo-American Aeronautical Conference.

35. Peake, DJ. and Tobak, M**.** (1980) *Three-Dimensional Interactions and Vortical Flows with Emphasis on High Speeds.* NASA TM-81169.

36. Munk, MM. (1924) *Elements of the Wing Section Theory and of the Wing Theory.* NACA Rep. 191.

37. Anderson, JD. Jr. (2007) Fundamentals of Aerodynamics. 4th. New York. McGraw-Hill.

38. Munk, MM. (1924). *The Aerodynamic Forces on Airship Hulls.* NACA Rep. 184.

39. Nielsen, JN. and Pitts, WC. (1952) *Wing-body interference at supersonic speeds with an application to combinations with rectangular wings.*, NACA TN 2677.

40. Ferrari, C. (1948) *Interference between wing and body at supersonic speeds - theory and numerical application.* Journal of the Aeronautical Sciences, pp. 317-336.

41. Hemsch, MJ. *Semi-empirical methods for conventional and unconventional missiles.* PRC Kentron. Hampton, Virginia.

42. Pitts, WC., Nielsen, JN. and Kaattari, GE. (1957) *Lift and center of pressure of wing-body-tail combinations at subsonic, transonic and supersonic speeds.* NACA Report 1307.

43. Nelson, HF. (1989) *Wing-body interferance lift for supersonic missiles with elliptical cross-section fuselages.* Journal of Spacecraft and Rockets. Vol. 26, No. 5, pp. 322 - 329.

44. Vukelich, SR. and Williams AR. Jr. (1981) *Wing-Body Carryover at Supersionic Speeds with Finite Afterbodies.*, AIAA 81-4113. Vol. 19, pp. 661-664.

45. Vira, NR. and Fan, D**.** (1982) *Closed-Form Solutions of Supersonic Wing-Body Interference.,* AIAA 82-4146. Vol. 20, pp. 855-857.

46. Vira, NR. and Fan, D**.** (1982) *Supersonic Wing-Body Centre of Pressure with Finite Afterbodies.*, AIAA 82-4189. Vol. 20, pp. 1144-1146.

47. Nelson, HF. and Bossi, BW. (1995) *Aerodynamic interference for supersonic low-aspect-ratio missiles.*, Journal of Spacecraft and Rockets. Vol. 32, No. 2, pp. 270-278.

48. Est, BE. and Nelson, HF. (1995) *Wing-body carryover for noncircular missiles.*, Journal of Spacecraft and Rockets. pp. 426-432.

49. Hemsch, MJ., et al. (1977) *Component aerodynamic characteristics of banked cruciform missiles with arbitrary control deflection.* AIAA Paper 77-1153. pp. 288 - 299.

50. Hemsch, MJ. and Nielsen, JN. (1986) *Equivalent Angle of Attack Concept*. [ed.] Hemsch, MJ. and Nielsen, JN. Tactical Missile Aerodynamics, Vol. 104. American Institute of Aeronautics and Astronautics, Inc., pp. 487-518.

51. Hemsch, MJ. and Nielsen, JN. (1983) *Equivalent Angle of Attack Method for Estimating Nonlinear Aerodynamics of Missile Fins.* Journal of Spacecraft and Rockets. Vol. 20, pp. 356-362.

52. Morikawa, G. (1951) *Supersonic Wing-Body Lift.*, Journal of the Aeronautical Sciences. Vol. 18, pp. 217-228.

53. Ward, G. N. (1949), *Calculation of Downwash behind a Supersonic Wing.* The Aeronautical Quarterly. Vol. 1.

54. Edwards, RH. (1954) *Leading Edge Separation from Delta Wings.* Journal of the Aeronautical Sciences (Readers Forum). Vol. 21, pp. 134-135.

55. Sacks, AH. (1952) *Behaviour of vortex systems behind cruciform wings - motions of fully rolled-up vortices.* NACA TN 2605.

56. Spahr, JR. (1961) *Theoretical Prediction of the Effects of Vortex Flows on the Loading, Forces and Moments of Slender Aircraft.*. NASA TR R-101.

57. Sacks, AH. (1955) *Vortex Interference on Slender Airplanes.*. NACA TN 3525.

58. Mendenhall, MR. and Perkins, SC. Jr. (1986) *Vortex Cloud Model for Body Vortex Shedding and Tracking*. [ed.] Hemsch, MJ. and Nielsen, JN. Tactical Missile Aerodynamics, Vol. 104. American Institute of Aeronautics and Astronautics, Inc. pp 519-564.

59. Sacks, AH., Lundberg, RE. and Hanson, CW. (1967) *A Theoretical Investigation of the Aerodynamics of Slender Wing-Body Combinations Exhibitinh Leading Edge Separation.*. NASA CR-719.

60. Stratford, BS. (1954) *Flow in the Laminar Boundary Layer near Separation.* Aeronautical Research Council Reports and Memoranda No. 3002.

61. Stratford, BS. (1958) *The Prediction of Separation of the Turbulent Boundary Layer.* Journal of Fluid Mechanics. Vol. 5.

62. Mendenhall, MR. and Lesieutre, DJ. (1987) *Prediction of Vortex Shedding from Circular and Noncircular Bodies in Subsonic Flow*. NASA CR-4037.

63. Ericsson, L. E. and Reding, J. P. (1986) *Asymmetric Vortex Shedding from Bodies of Revolution*. [ed.] Hemsch, MJ. and Nielsen, JN. Tactical Missile Aerodynamics, Vol. 104. American Institute of Aeronautics and Astronautics, Inc. pp 243-286.

64. Goethert, BH. (1961) Transonic Wind Tunnel Testing. Pegramon Press.

65. Lombardi, G. and Morelli, M. (1995) *Analysis of Some Interference Effects in a Transonic Wind Tunnel.* Journal of Aircraft. Vol. 32.

66. Allen, JM. (2005) *Aerodynamics of an Axisymmetric Missile Concept Having Cruciform Strakes and In-Line Tail Fins from Mach 0.60 to 4.673.* NASA TM-2005-213541.

67. Chong, MS., Perry, AE. and Cantwel, BJ. (1990) A general classification of three-dimentional flow field. pp. 765 - 777.

68. Schafer, M. (2006) Computational Engineering: Introduction to numerical methods. Germany, Springer.

69. Chin, SS. (1961) Missile Configuration Design. New York, McGraw-Hill.

70. Mirels, H. and Haefeli, RC. (1949) *Line-vortex theory for calculation of supersonic downwash.* NACA TN 1925.

71. Deffenbaugh, FD. and Marshall, FJ. (1976) *Time developement of the flow about an impulsively started cylinder.* AIAA Journal, Vol. 14, pp. 908-913.

72. Alksne, AY. (1956) *Determination of vortex paths by series expansion technique with application to cruciform wings.* NACA TR 1311, pp. 693-707.

73. Rosenhead, L. (1931) *The formation of vortices from a surface of discontinuity.* Proceedings of the Royal Society of London, Vol. 134, pp. 170-192.

74. Mendenhall, MR. and Lesieutre, DJ. (1990) *Prediction of Subsonic Vortex Shedding from Forebodies with Chines.* NASA CR-4323.

75. Lamont, PJ. (1980) *Pressure Measurements of an Ogive-cylinder st High Angles of Attack with Laminar, Transitional or Turbulent Separation.*. AIAA 80-1556.

Appendix A

Experimental Setup

A grounding strip was installed utilizing a multimeter as shown in the diagram in Figure 78. The circuit is created so that a short circuit is created over the multimeter, which emits a warning sound when in the "Diode Test" mode (see Figure 79). The detailed design for the sting extension utilized in the LSWT tests is given in Figure 80 on the following page.

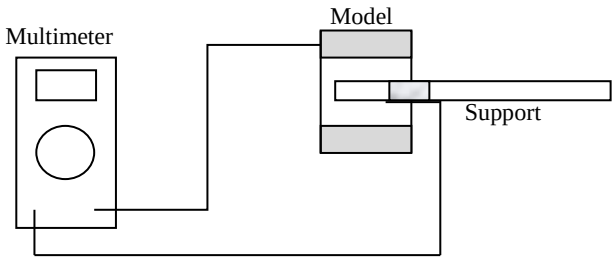

Figure 78: Grounding Strip Circuit

Figure 79: Diode Test Mode on Multimeter

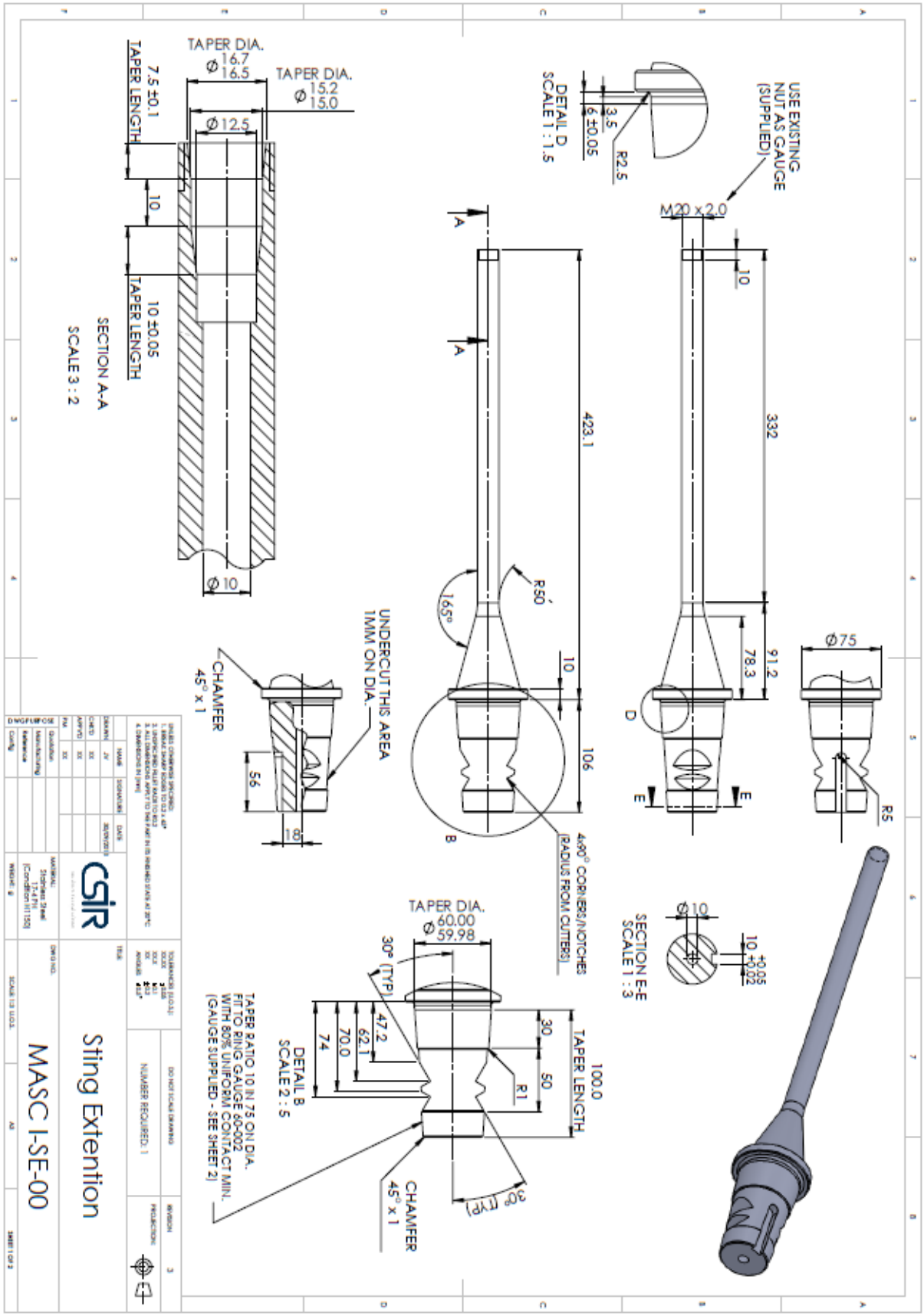

Figure 80: Sting Extension Detailed Design

Data Reduction

An internal strain gauge balance produces a Volt output representing the six different aerodynamic loads, namely normal force, pithing moment, side force, yawing moment, rolling moment and axial force. A matrix is used to convert a millivolt output to engineering units in the method of AIAA Standard R-091-2003. The forces and moments are denoted by the following abbreviations:

Normal force – NF

Pitching moment – PM

Side force – SF

Yawing moment – YM

Rolling moment – RM

Axial force – AF

The order of the output loads in millivolts (mV) may be demonstrated by the following vector:

$$\bar{V} = V_i = \begin{Bmatrix} NF \\ PM \\ SF \\ YM \\ RM \\ AF \end{Bmatrix}$$

A 2nd order 6x27 matrix converts the mV output V_i into engineering units F_i as follows:

$$F_i = \sum_{j=1}^{n} a_{i,j}\, V_j + \sum_{j=1}^{n}\sum_{k=j}^{n} b_{j,k}\, V_j V_k$$

where n is the number of loads (in this case 6), $a_{i,j}$ and $b_{j,k}$ represent the balance matrix that has been split into two separate matrices for mathematical convenience. Thus

$$\tilde{a} = B_{i,j} \begin{cases} j \leq 6 \\ 1 \leq i \leq 6 \end{cases}$$

and

$$\tilde{b} \rightarrow B_{i,j} \begin{cases} 7 \leq j \leq 27 \\ 1 \leq i \leq 6 \end{cases}$$

such that

$$b_{j,k} = \begin{bmatrix} B_{i,7} & B_{i,8} & B_{i,9} & B_{i,10} & B_{i,11} & B_{i,12} \\ 0 & B_{i,13} & B_{i,14} & B_{i,15} & B_{i,16} & B_{i,17} \\ 0 & 0 & B_{i,18} & B_{i,19} & B_{i,20} & B_{i,21} \\ 0 & \cdots & 0 & B_{i,22} & B_{i,23} & B_{i,24} \\ \vdots & \ddots & \vdots & 0 & B_{i,25} & B_{i,26} \\ 0 & \cdots & 0 & 0 & 0 & B_{i,27} \end{bmatrix} for\ 1 \leq i \leq 6$$

As an example the NF (represented by $i = 1$) in Newtons (N) will be calculated as follows:

For $n = 6, and\ i = 1$:

$$F_1 = \sum_{j=1}^{6} a_{1,j}\, V_j + \sum_{j=1}^{6}\sum_{k=j}^{6} b_{j,k}\, V_j V_k$$

$$= \left[a_{1,1}V_1 + a_{1,2}V_2 + \cdots + a_{1,6}V_6\right]$$

$$+\left[b_{1,1}V_1V_1 + b_{1,2}V_1V_2 + \cdots + b_{1,6}V_1V_6\right]$$

$$+\left[b_{2,2}V_2V_2 + b_{2,3}V_2V_3 + \cdots + b_{2,6}V_2V_6\right]$$

$$+\left[b_{3,3}V_3V_3 + b_{3,4}V_3V_4 + \cdots + b_{3,6}V_3V_6\right]$$

$$+\left[b_{4,4}V_4V_4 + b_{4,5}V_4V_5 + b_{4,6}V_4V_6\right]$$

$$+\left[b_{5,5}V_5V_5 + b_{5,6}V_5V_6\right]$$

$$+\left[b_{6,6}V_6V_6\right]$$

Thus

$$F_1 = \left[B_{1,1}V_1 + B_{1,2}V_2 + \cdots + B_{1,6}V_6\right]$$

$$+\left[B_{1,7}V_1V_1 + B_{1,8}V_1V_2 + \cdots + B_{1,12}V_1V_6\right]$$

$$+\left[B_{1,13}V_2V_2 + B_{1,14}V_2V_3 + \cdots + B_{1,17}V_2V_6\right]$$

$$+\left[B_{1,18}V_3V_3 + B_{1,19}V_3V_4 + \cdots + B_{1,21}V_3V_6\right]$$

$$+\left[B_{1,22}V_4V_4 + B_{1,23}V_4V_5 + B_{1,24}V_4V_6\right]$$

$$+\left[B_{1,25}V_5V_5 + B_{1,26}V_5V_6\right]$$

$$+\left[B_{1,27}V_6V_6\right]$$

The loads are also converted to the following body axes coefficients:

Normal force coefficient – C_N

Pitching moment coefficient – C_m

Side force coefficient – C_Y

Yawing moment coefficient – C_n

Rolling moment coefficient – C_l

Axial force coefficient – C_A

The reference areas, lengths used are listed in Table 7.

Table 7: Non-dimensionalisation constants

Parameter	Value	Unit
D	0.045	m
S	0.00159	m^2
mrc	0	mm from nose

The term "mrc" refers to the moment reference centre and the term "brc" is generally used for the balance reference centre. The non-dimensionalisation formulae for the aerodynamic coefficients are as follows

$$C_N = \frac{F_N}{\frac{1}{2}\rho V^2 S}$$

$$C_m = \frac{M_m}{\frac{1}{2}\rho V^2 S D}$$

$$C_Y = \frac{F_Y}{\frac{1}{2}\rho V^2 S}$$

$$C_n = \frac{M_n}{\frac{1}{2}\rho V^2 S D}$$

$$C_l = \frac{M_l}{\frac{1}{2}\rho V^2 S D}$$

$$C_A = \frac{F_A}{\frac{1}{2}\rho V^2 S}$$

Sample calculation:

Given

$$\bar{V} = \begin{Bmatrix} 0.099514 \\ -0.0115941 \\ -2.074375 \\ 0.153201 \\ 0.034863 \\ 0.018310 \end{Bmatrix} (mV)$$

The 2nd order matrix *B* is given by

B =	36.9446	-0.0158	0.9152	-0.0507	0.4960	0.2287	0	
	0.0162	-0.7472	-0.0006	-0.0102	-0.0229	-0.0220	0	
	-2.8755	-0.2913	37.6165	0.2617	1.4201	-0.0949	0	
	-0.0120	0.0066	-0.0077	-0.7751	0.0130	0.0048	0	
	-0.4513	-0.0014	-0.0116	-0.0113	0.4281	0.0281	0.0053	0.0001
	-0.1803	0.0491	0.5205	0.2946	-0.1373	24.9896	0.0438	

…	-0.026	0.000	0.000	0.048	0.000	-0.010	0.000	0.000	…
…	0.000	0.000	0.000	-0.005	0.000	0.000	0.000	0.000	…
…	0.000	-0.002	0.000	0.051	0.000	0.017	0.000	0.009	…
…	0.000	0.000	0.000	0.000	0.000	0.001	0.000	0.000	…
…	0.005	0.000	0.000	-0.003	0.000	0.000	0.001	0.000	…
…	0.029	0.015	0.000	0.466	0.007	0.049	0.000	0.000	…

…	0.000	0.000	0.000	0.000	0.000	-0.011	0.000	0.000	…
…	0.000	0.000	0.000	0.000	0.000	0.001	0.000	0.000	…
…	0.000	0.000	-0.012	0.000	0.000	0.000	0.000	0.000	…
…	0.000	0.000	0.000	0.000	0.000	0.000	0.000	0.000	…
…	0.000	0.000	0.000	0.000	0.000	0.000	0.000	0.000	…
…	0.000	0.000	-0.051	0.000	0.000	0.065	0.000	0.000	…

…	0.000	0.000	0.000
…	0.000	0.000	0.000
…	0.007	0.000	0.000
…	0.000	0.000	0.000
…	0.000	0.000	0.000
…	0.013	0.000	0.000

Matrix B is separated into

$$\tilde{\alpha} = \begin{vmatrix} 36.9446 & -0.0158 & 0.9152 & -0.0507 & 0.4960 & 0.2287 \\ 0.0162 & -0.7472 & -0.0006 & -0.0102 & -0.0229 & -0.0220 \\ -2.8755 & -0.2913 & 37.6165 & 0.2617 & 1.4201 & -0.0949 \\ -0.0120 & 0.0066 & -0.0077 & -0.7751 & 0.0130 & 0.0048 \\ -0.4513 & -0.0014 & -0.0116 & -0.0113 & 0.4281 & 0.0281 \\ -0.1803 & 0.0491 & 0.5205 & 0.2946 & -0.1373 & 24.9896 \end{vmatrix}$$

and

$$\tilde{b} = \begin{vmatrix} 0 & 0 & -0.026 & 0 & 0 & 0.048 \\ 0 & 0 & -0.010 & 0 & 0 & 0 \\ 0 & 0 & 0 & 0 & 0 & 0 \\ 0 & 0 & 0 & -0.011 & 0 & 0 \\ 0 & 0 & 0 & 0 & 0 & 0 \\ 0 & 0 & 0 & 0 & 0 & 0 \end{vmatrix}$$

Thus

$$NF = F_1 = \sum_{j=1}^{6} a_{1,j}\, V_j + \sum_{j=1}^{6}\sum_{k=j}^{6} b_{j,k}\, V_j V_k$$

$$= \left[a_{1,1}V_1 + a_{1,2}V_2 + \cdots + a_{1,6}V_6\right]$$

$$+\left[b_{1,3}V_1V_3 + b_{1,6}V_1V_6\right] + \left[b_{2,3}V_2V_3\right] + \left[b_{4,4}V_4V_4\right]$$

$$\therefore F_1 = [36.9446(0.099514) \pm 0.0158(-0.0115941) + \cdots + 0.2287(0.018310)]$$

$$+[-0.026(0.0995)(-2.0744) + 0.048(0.0995)(0.0183)]$$

$$+[-0.010(-0.01159)(-2.0744) - 0.011(0.1532)^2]$$

$$= 1.683\ N$$

Given the following flow properties:

$$V = 33\frac{\mathrm{m}}{\mathrm{s}}$$

$$\rho = 1\ {}^{\mathrm{kg}}/_{\mathrm{m}^3}$$

$$\mathrm{S} = \frac{1}{2}\pi \mathrm{r}^2 = 2.513 \times 10^{-3}\ \mathrm{m}^2$$

The normal force coefficient C_N is then

$$C_N = \frac{F_1}{\frac{1}{2}\rho V^2 S}$$

$$= \frac{1.683}{\frac{1}{2}(1)(33)^2(2.513 \times 10^{-3})}$$

$$= 1.230$$

Flow angularity

The flow angularity for the facility was calculated at all Mach numbers using the upright and inverted polars. The flow angularity needs to be added to the reported angle of attack to obtain the corrected angle of attack and similarly the coefficient offset needs to be added to the reported normal force coefficient to obtain the corrected value. For each curve in the linear region ($\alpha < 4°$) the formulas are

$$y_1 = mx_1 + c_1$$

$$y_2 = mx_2 + c_2$$

Flow angularity δα is then

For $y_1 = y_2 = 0$,

$$x_1 = -\frac{c_1}{m}, \quad x_2 = -\frac{c_2}{m}$$

$$\delta\alpha = \frac{x_2 - x_1}{2}$$

The offsets are then determined to be

$$\delta C_N = \frac{c_1 + c_2}{2}$$

For example, given a set of data with the following properties in the linear range

$$m = 0.0538$$

$$c_1 = -0.1157, \quad c_2 = -0.2232$$

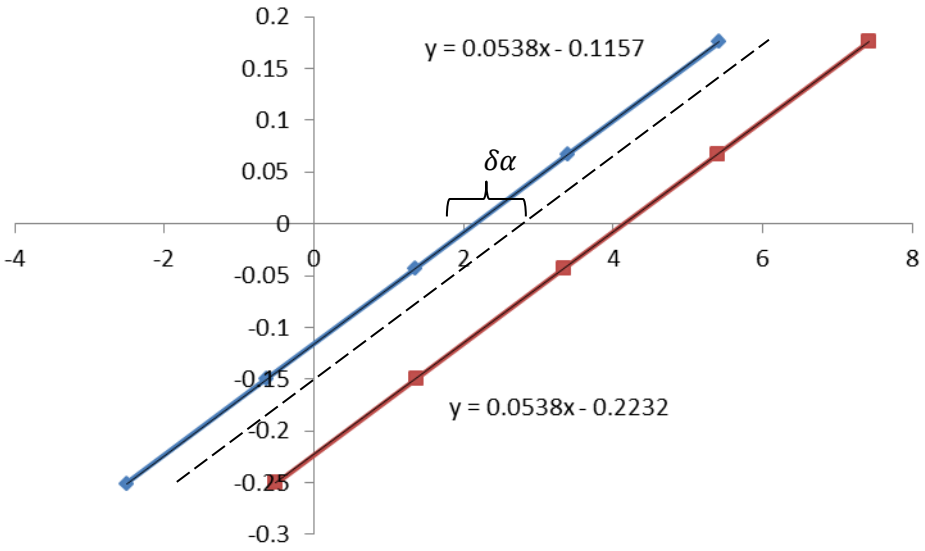

Thus

$$x_1 = -\frac{c_1}{m} = -\frac{-0.1157}{0.0538} = 2.15$$

$$x_2 = -\frac{c_2}{m} = -\frac{-0.2232}{0.0538} = 4.15$$

$$\delta\alpha = \frac{x_2 - x_1}{2} = \frac{4.15 - 2.15}{2} = 1°$$

$$\delta C_N = \frac{c_1 + c_2}{2} = \frac{-0.1157 - (-0.2232)}{2} = 0.054$$

The flow angularity and offsets as calculated from the data are given in Table 8.

Table 8: Flow Angularity and Offsets

Configuration	Mach No.	Flow angularity	Offsets
s/D = 1.25	0.1	0.10509449	0.02026835
	0.2	0.04993097	0.03873343
	0.3	0.11956691	-0.0130713
s/D = 1.5	0.1	0.29763916	0.07919894
	0.2	0.29211622	0.0615801
	0.3	0.01295183	0.03999609
s/D = 1.75	0.1	0.72119835	0.18055145
	0.2	0.11208269	0.02559908
	0.3	0.18035523	0.03843736

Examples of the data for Mach 0.2 LSWT tests with applied flow angularities and corrected offsets are shown in Figure 81.

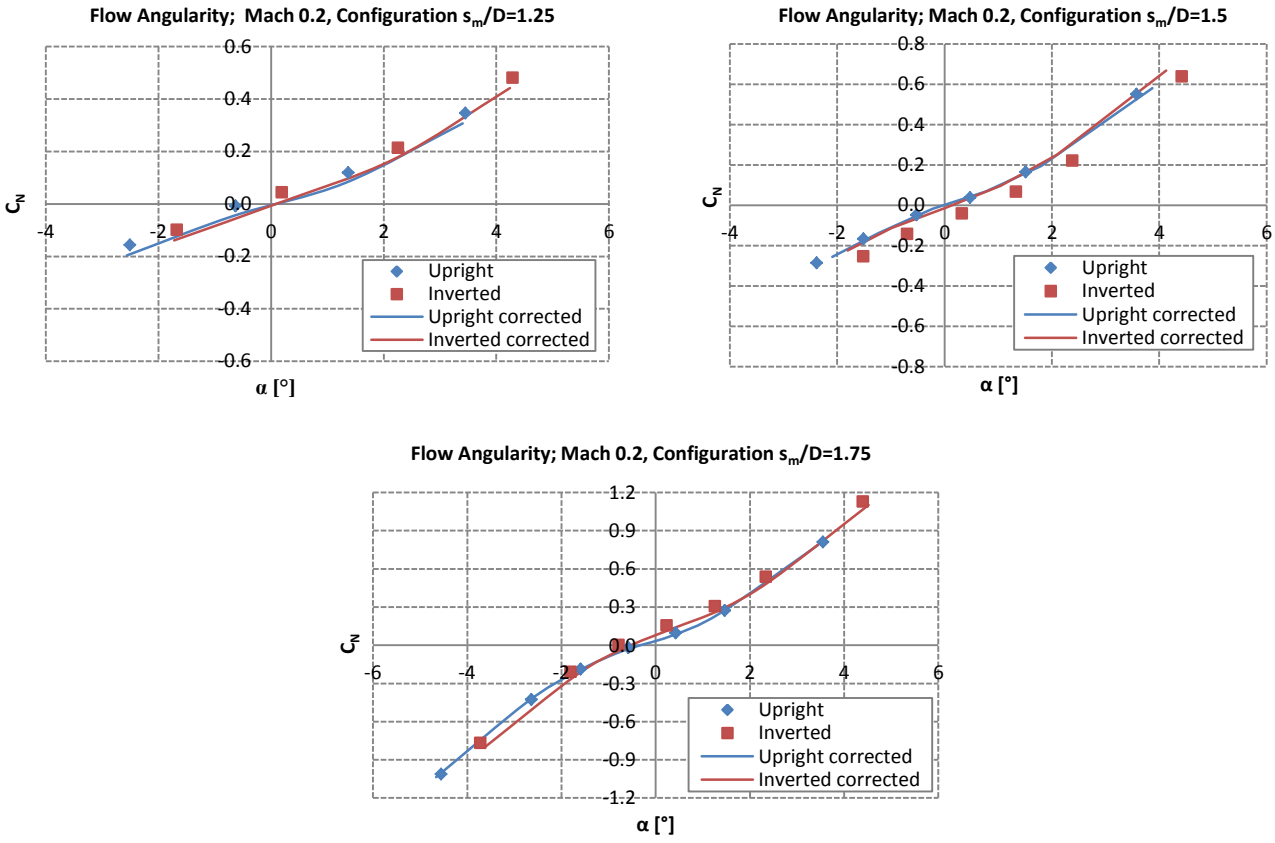

Figure 81: Flow Angularity and Offset Corrections

Uncertainties

The balance uncertainties are determined during balance calibration. The balance uncertainties for normal force and pitching moment coefficient uncertainties are given as

$$\Delta N = 0.263$$

$$\Delta M = 0.0214$$

The load coefficient uncertainties are calculated using the method of Coleman & Steele which utilises a Fouries series expansion of the coefficient formula. For the normal force coefficient

$$C_N = \frac{N}{\frac{1}{2}\rho V^2 S}$$

where N is the normal force in Newtons (N), ρ is the density (kg/m3), V is the free stream velocity (m/s) and S is the reference area. The uncertainty would then be calculated as

$$\Delta {C_N}^2 = \left(\frac{\partial C_N}{\partial N}\Delta N\right)^2 + \left(\frac{\partial C_N}{\partial \rho}\Delta \rho\right)^2 + \left(\frac{\partial C_N}{\partial V}\Delta V\right)^2 + \left(\frac{\partial C_N}{\partial S}\Delta S\right)^2$$

where ρ and V are measured and S is constant, therefore Δρ, ΔV and ΔS are zero. Thus

$$\Delta {C_N}^2 = \left(\frac{\partial C_N}{\partial N}\Delta N\right)^2$$

$$= \left(\frac{2}{\rho V^2 S}\right)^2 \Delta N^2$$

For the non-dimensionalised centre-of-pressure position

$$X_{C_p} = \frac{C_m}{C_N} = \frac{M}{ND}$$

where D is the body diameter (m) and M is the pitching moment (N.m). The uncertainty would be

$$\Delta X_{C_p}{}^2 = \left(\frac{\partial X_{C_p}}{\partial \mathrm{M}}\Delta \mathrm{M}\right)^2 + \left(\frac{\partial X_{C_p}}{\partial \mathrm{N}}\Delta \mathrm{N}\right)^2 + \left(\frac{\partial X_{C_p}}{\partial \mathrm{D}}\Delta \mathrm{D}\right)^2$$

Since D is constant ΔD is zero, thus the uncertainty is only dependent on N and M which vary with angle of attack:

$$\Delta X_{C_p}{}^2 = \left(\frac{\partial X_{C_p}}{\partial M}\Delta M\right)^2 + \left(\frac{\partial X_{C_p}}{\partial N}\Delta N\right)^2$$

$$= \frac{1}{N^2 D^2}(\Delta M)^2 + \frac{M^2}{N^4 D^2}(\Delta N)^2$$

Sample calculation:

With the following flow properties

$$V = 33\frac{m}{s}$$

$$\rho = 1\ {}^{kg}/_{m^3}$$

$$S = \frac{1}{4}\pi D^2$$

$$= \frac{1}{4}\pi(0.045^2)$$

$$= 3.181 \times 10^{-3}\ m^2$$

$$\therefore \Delta C_N = \left(\frac{2}{\rho V^2 S}\right)\Delta N$$

$$= \left(\frac{2}{(1)(33)^2(3.181 \times 10^{-3})}\right)(0.263)$$

$$= 0.1518$$

With D=0.045m and At α = 10°

- N = 2.636 N
- M = 1.877 Nm

$$\Delta X_{C_p}{}^2 = \frac{1}{N^2 D^2}(\Delta M)^2 + \frac{M^2}{N^4 D^2}(\Delta N)^2$$

$$\Delta X_{C_p}{}^2 = \frac{1}{(2.636)^2(0.045)^2}(0.0214)^2 + \frac{(1.877)^2}{(2.636)^4(0.045)^2}(0.263)^2$$

$$\Delta X_{C_p}{}^2 = 2.525$$

$$\therefore \Delta X_{C_p} = 1.589$$

The following graphs show C_N and X_{C_p} experimental results with the uncertainties as calculated for each different Mach number:

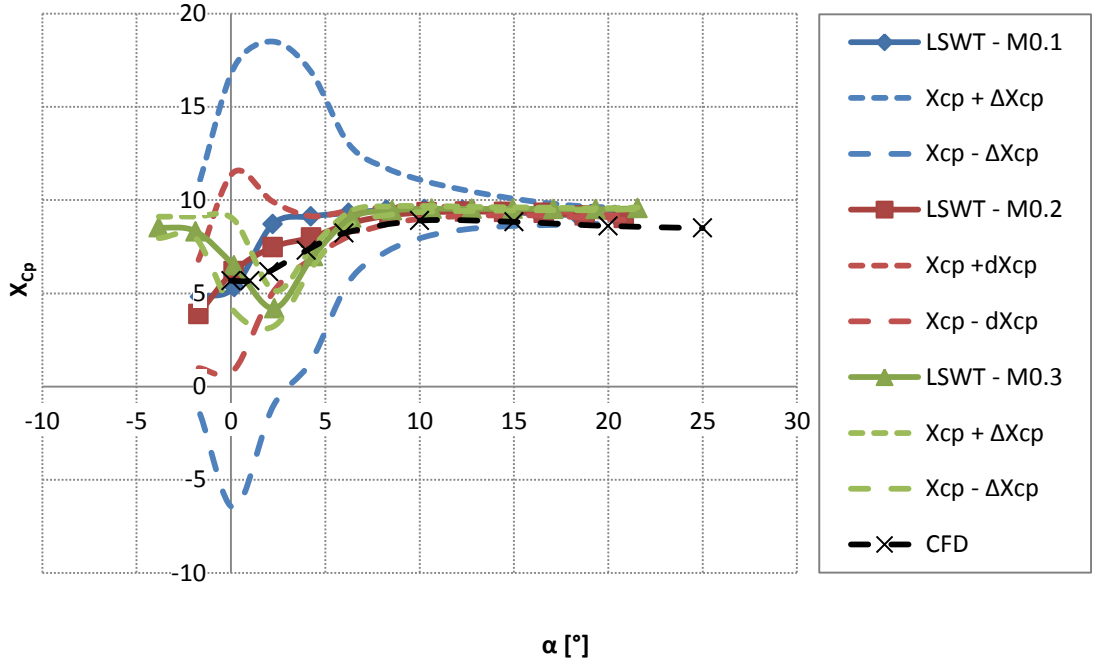

Figure 82: Experimental uncertainties for centre-of-pressure measurements for s/D=1.25

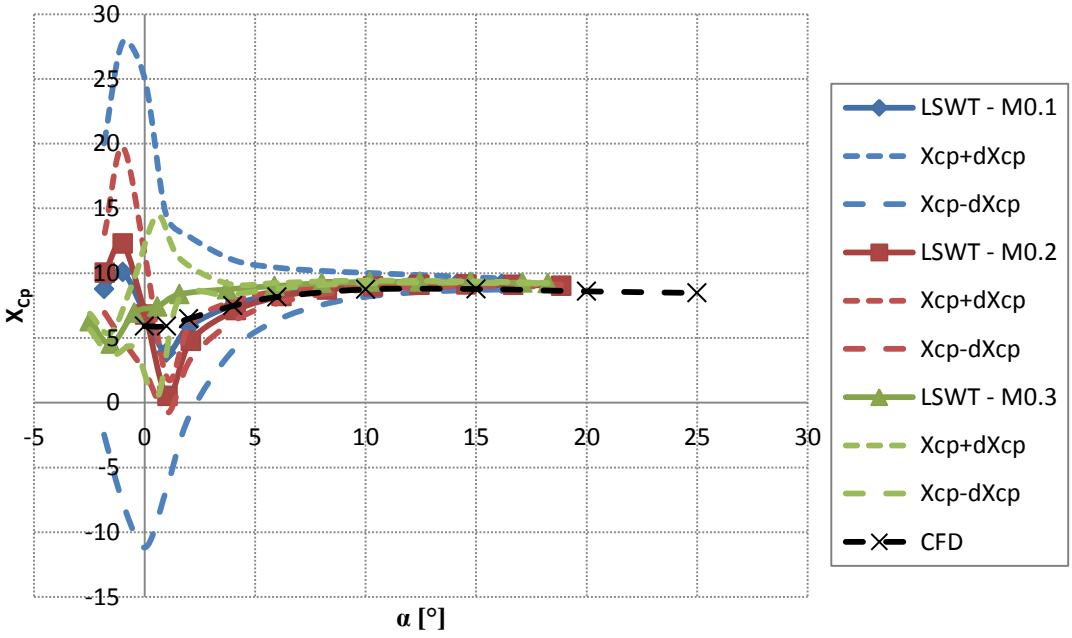

Figure 83: Experimental uncertainties for centre-of-pressure measurements for s/D=1.5

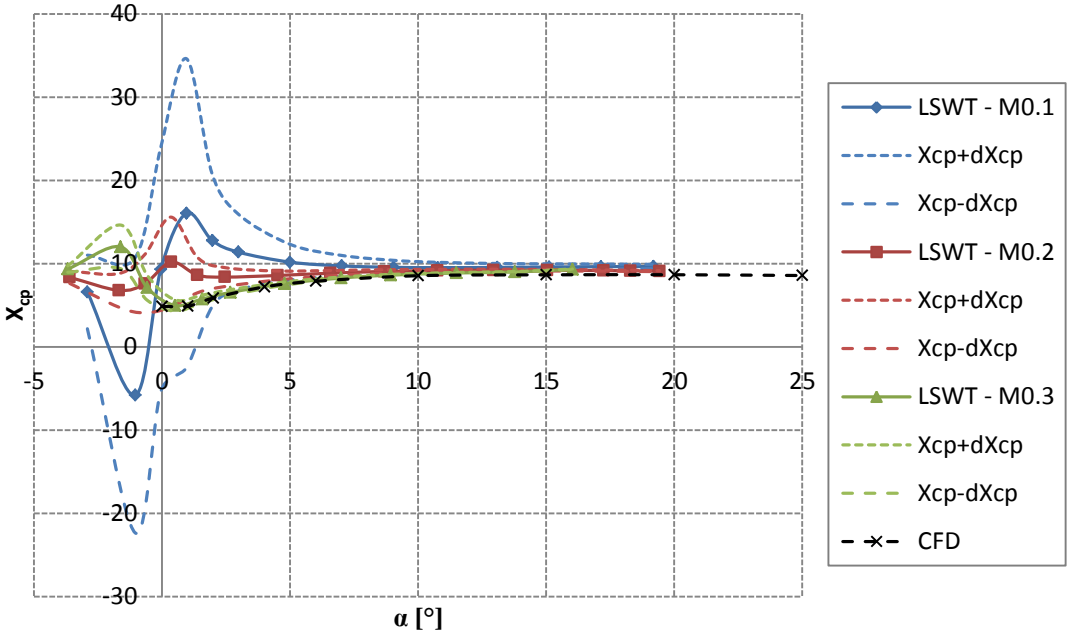

Figure 84: Experimental uncertainties for centre-of-pressure measurements for s/D=1.75

Appendix B

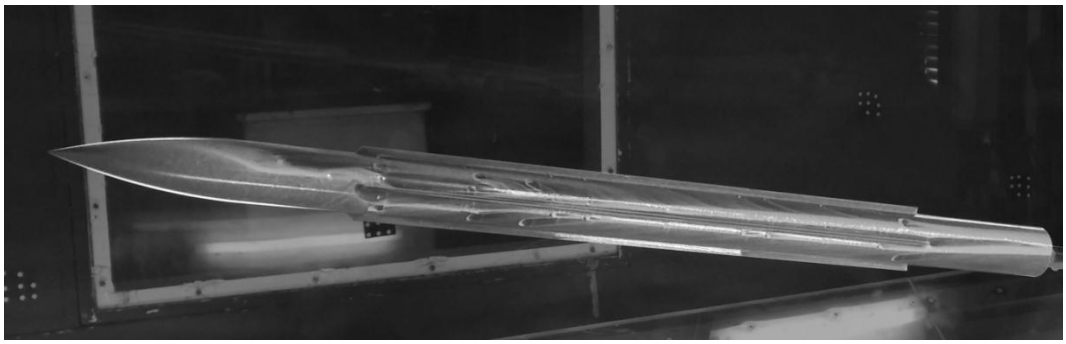

(a)

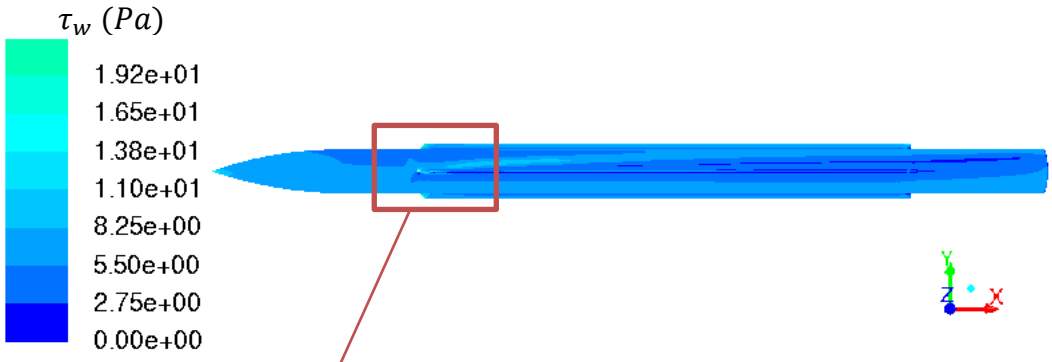

(b)

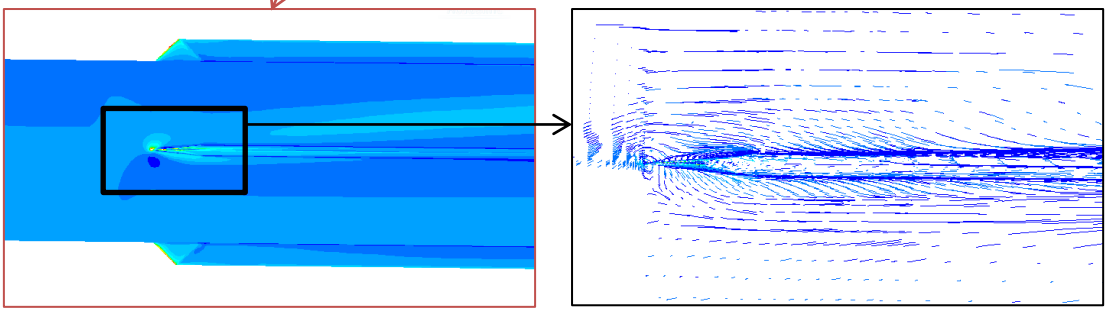

(c)

Figure 85: Side view comparison of (a) experimental surface flow and (b) CFD wall shear stress (Pa) with (c) CFD pathlines for s/D = 1.25 and α = 10°

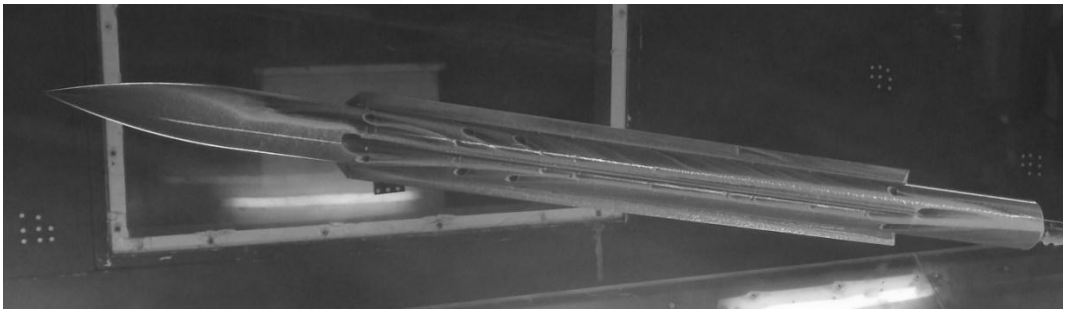

(a)

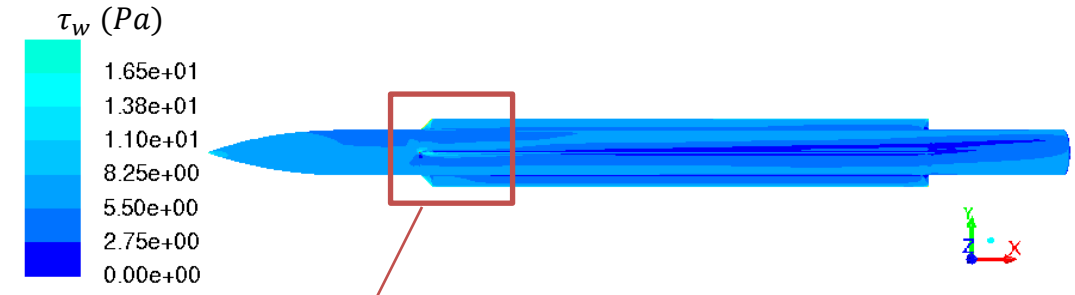

(b)

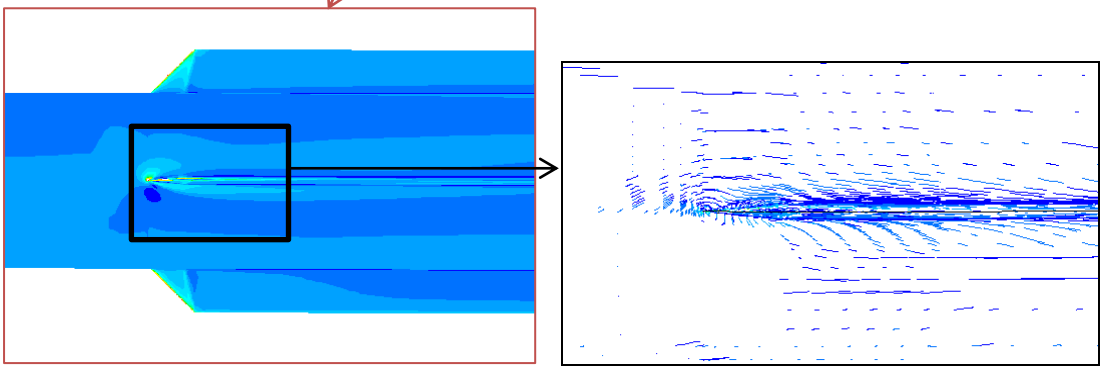

(c)

Figure 86: Side view comparison of (a) experimental surface flow and (b) CFD wall shear stress (Pa) with (c) CFD pathlines for s/D = 1.5 and α = 10°

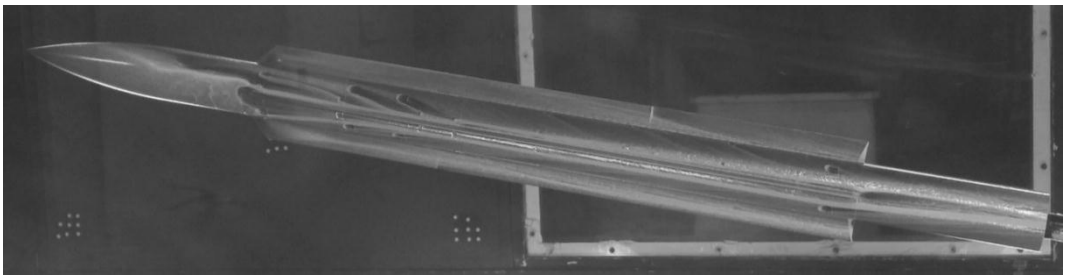

(a)

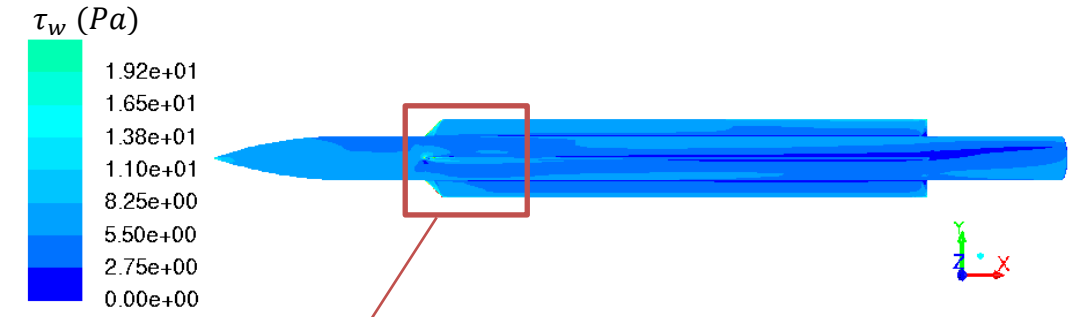

(b)

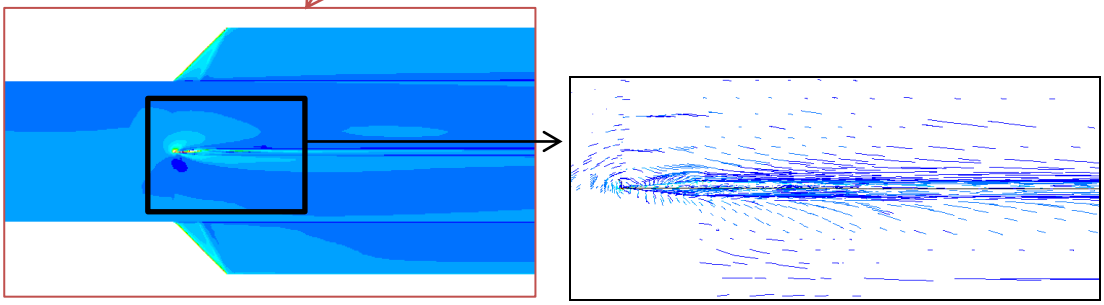

(c)

Figure 87: Side view comparison of (a) experimental surface flow and (b) CFD wall shear stress (Pa) with (c) CFD pathlines for s/D = 1.75 and α = 10°

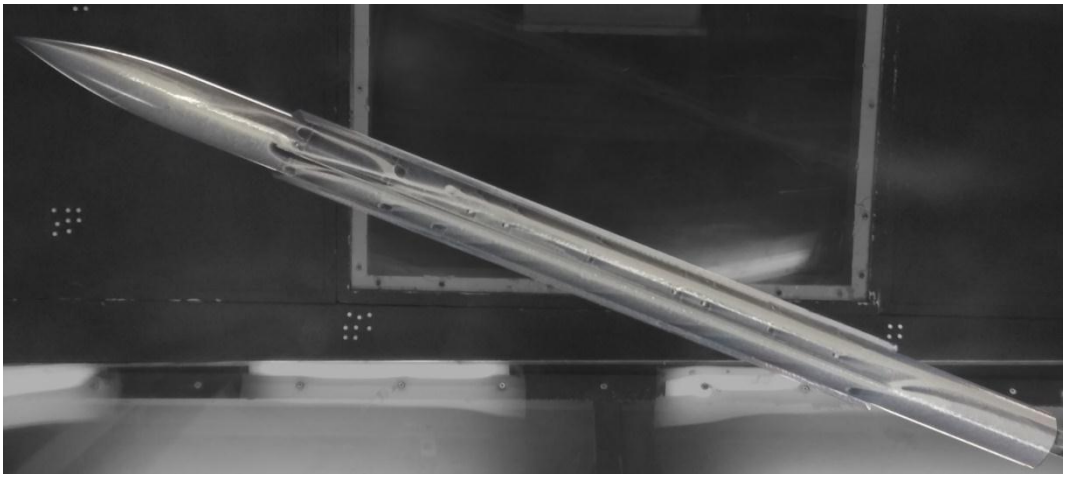

(a)

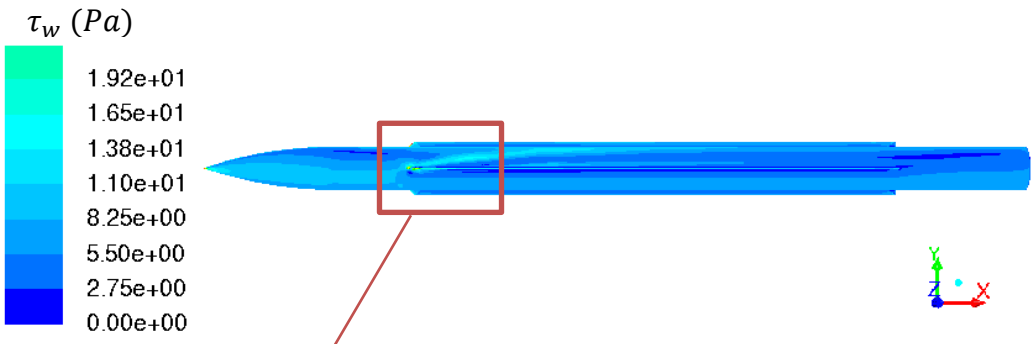

(b)

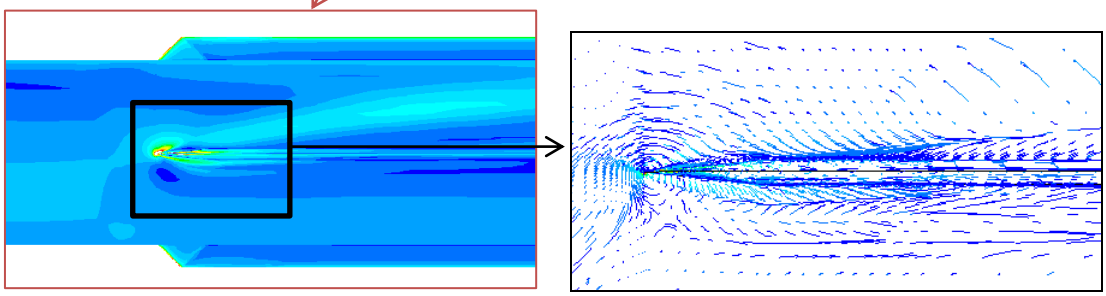

(c)

Figure 88: Side view comparison of (a) experimental surface flow and (b) CFD wall shear stress (Pa) with (c) CFD pathlines for s/D = 1.25 and α = 20°

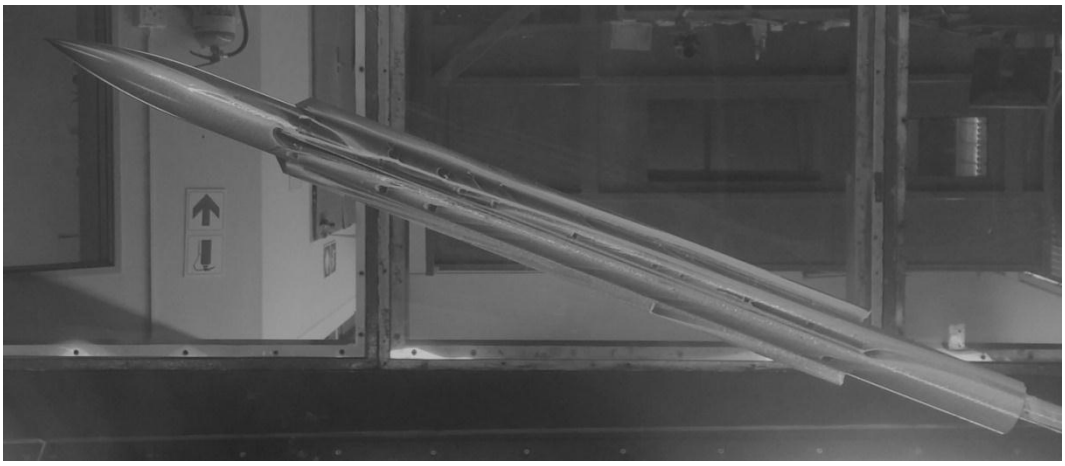

(a)

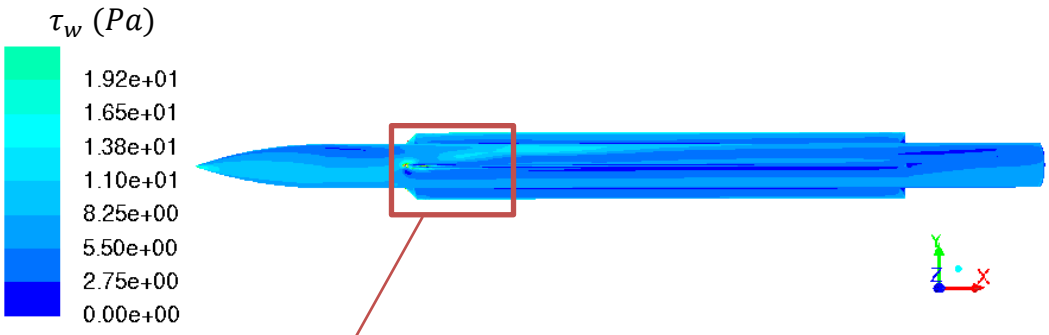

(b)

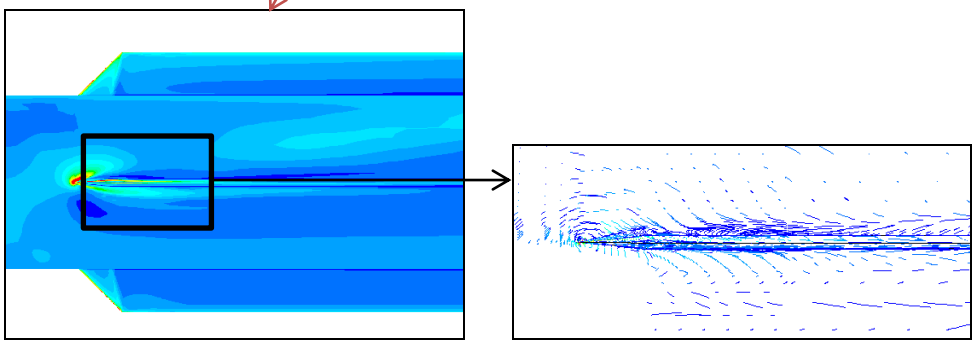

(c)

Figure 89: Side view comparison of (a) experimental surface flow and (b) CFD wall shear stress (Pa) with (c) CFD pathlines for s/D = 1.5 and α = 20°

s/D=1.75, alpha = 20deg

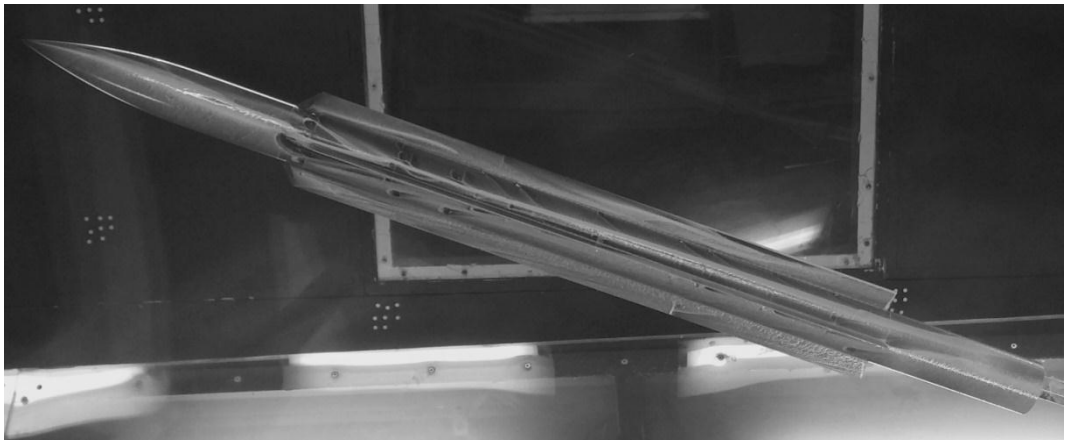

(a)

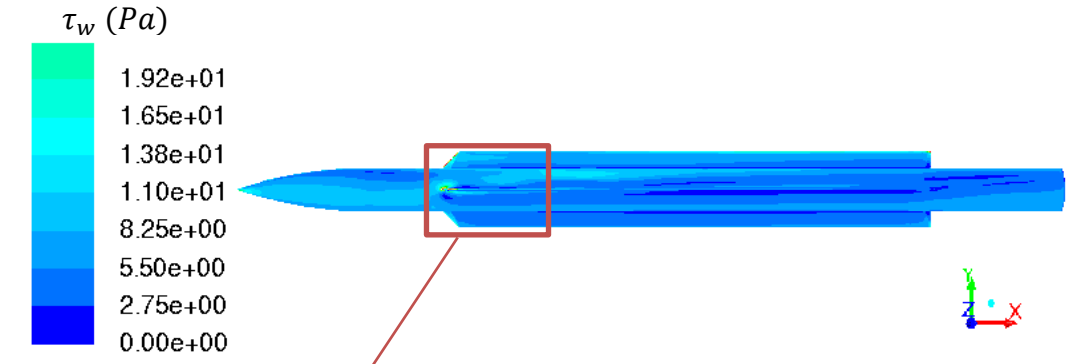

(b)

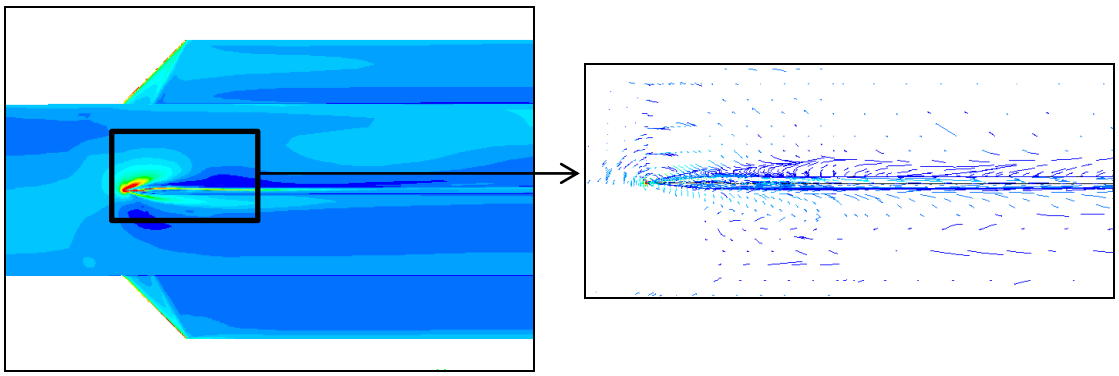

(c)

Figure 90: Side view comparison of (a) experimental surface flow and (b) CFD wall shear stress (Pa) with (c) CFD pathlines for s/D = 1.75 and α = 20°

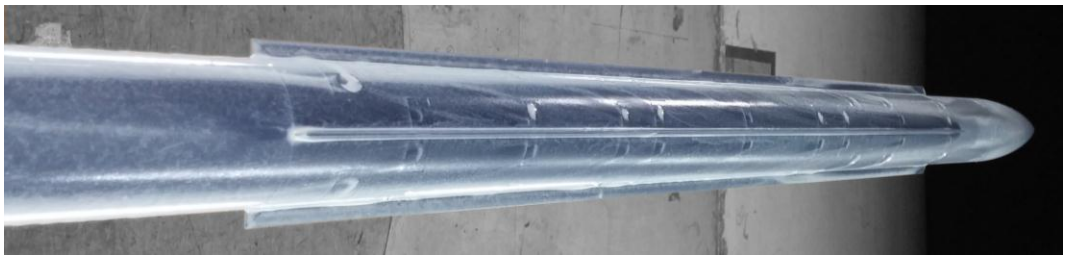

(a)

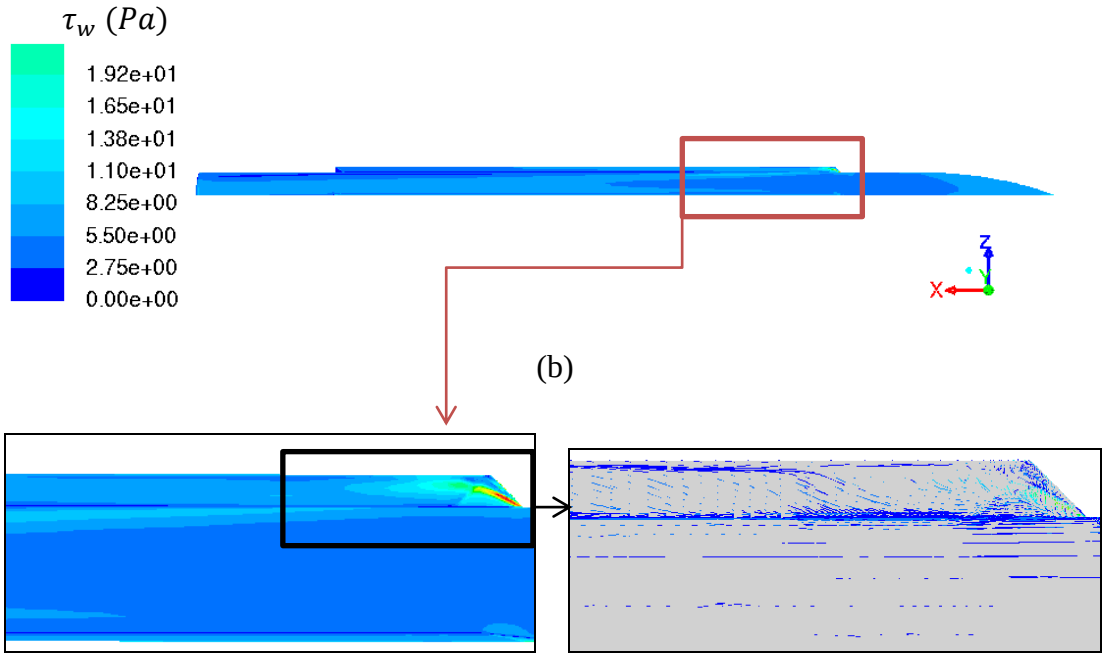

(b)

(c)

Figure 91: Top view comparison of (a) experimental surface flow and (b) CFD wall shear stress (Pa) with (c) CFD pathlines for s/D = 1.25 and α = 10°

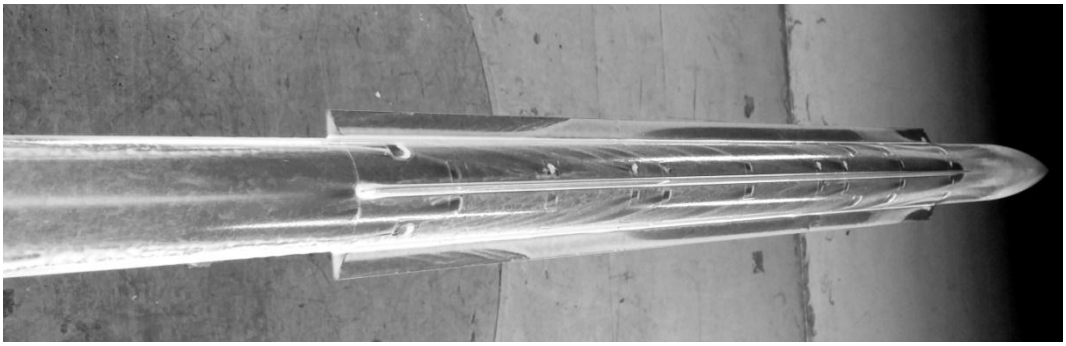

(a)

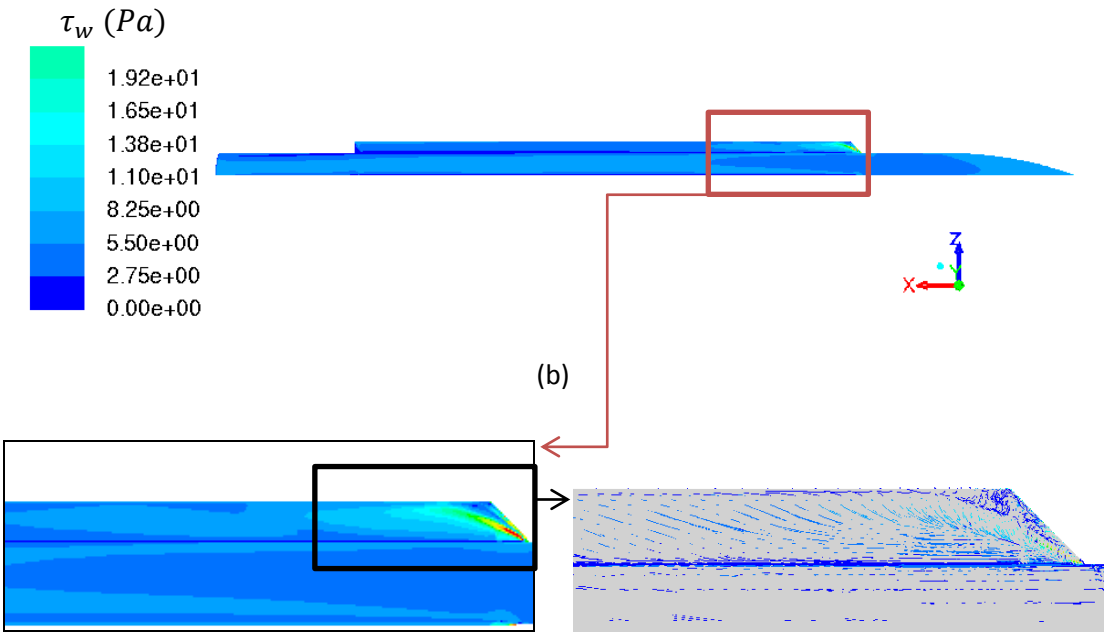

(b)

(c)

Figure 92: Top view comparison of (a) experimental surface flow and (b) CFD wall shear stress (Pa) with (c) CFD pathlines for s/D = 1.5 and α = 10°

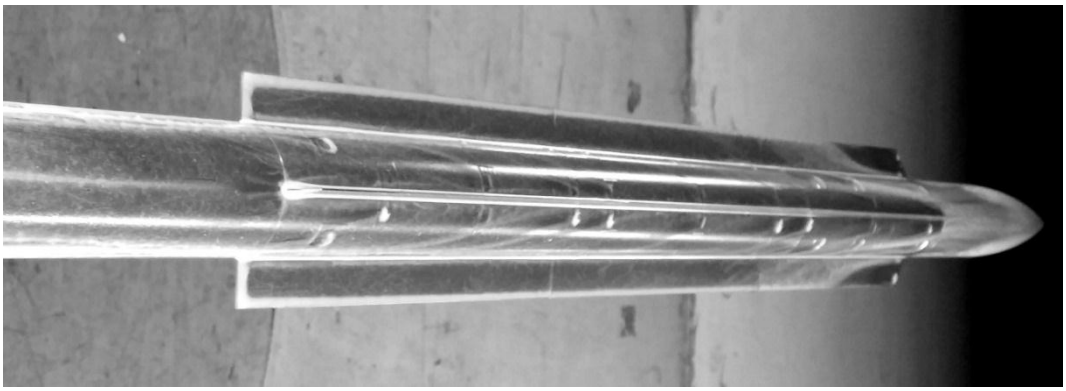

(a)

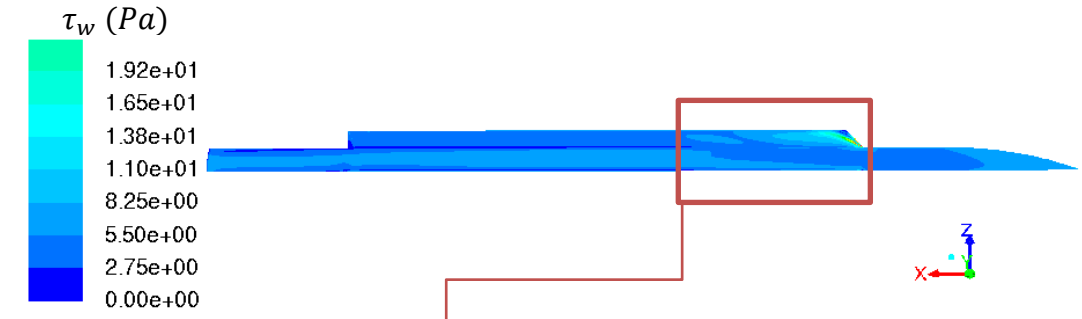

(b)

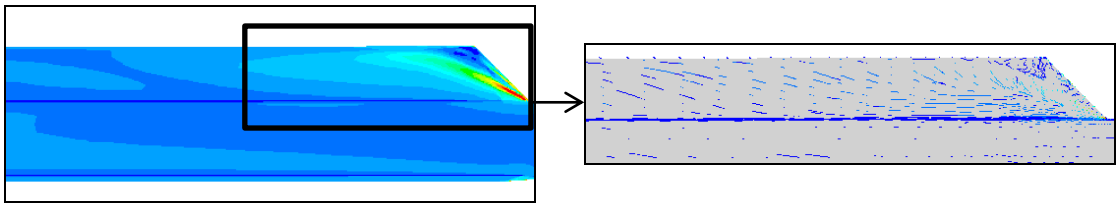

(c)

Figure 93: Top view comparison of (a) experimental surface flow and (b) CFD wall shear stress (Pa) with (c) CFD pathlines for s/D = 1.75 and α = 10°

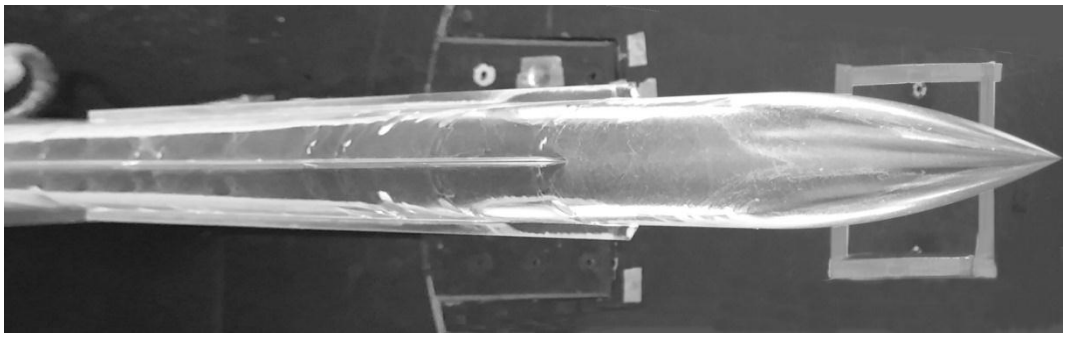

(a)

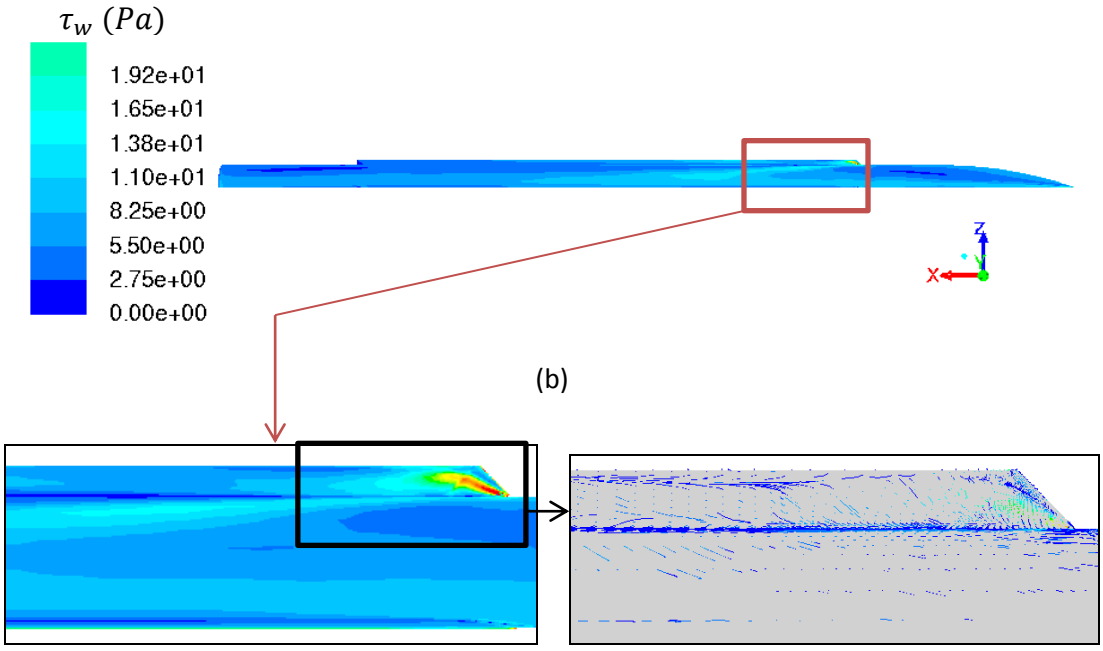

(b)

(c)

Figure 94: Top view comparison of (a) experimental surface flow and (b) CFD wall shear stress (Pa) with (c) CFD pathlines for s/D = 1.25 and α = 20°

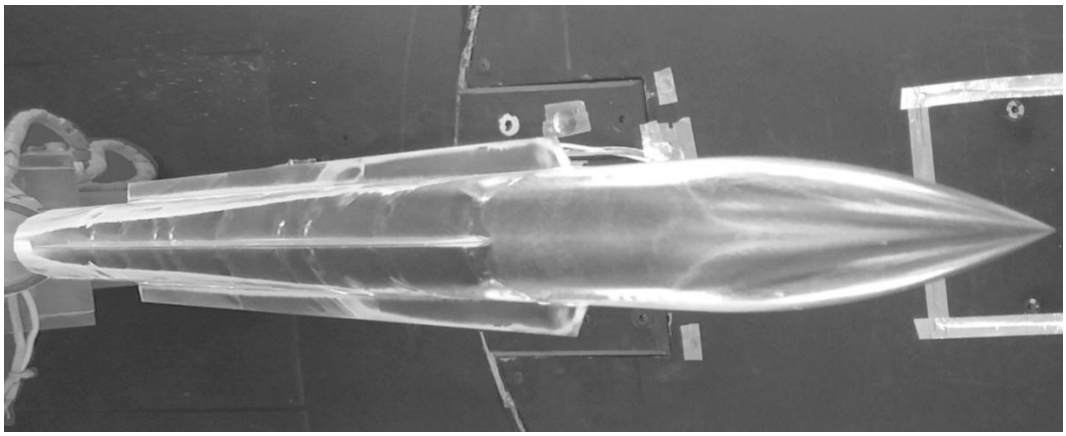

(a)

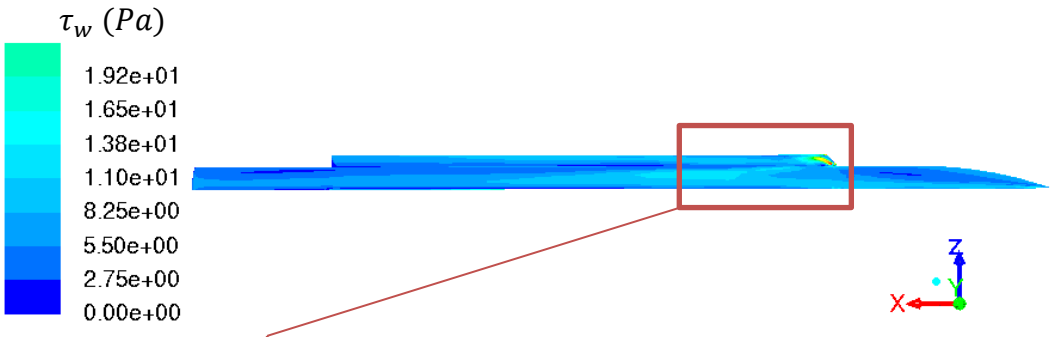

(b)

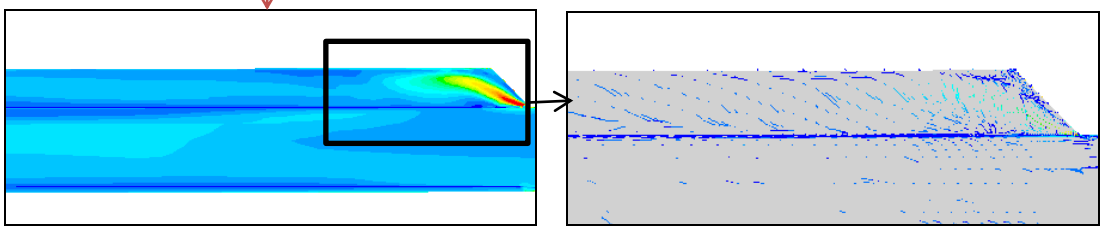

(c)

Figure 95: Top view comparison of (a) experimental surface flow and (b) CFD wall shear stress (Pa) with (c) CFD pathlines for s/D = 1.5 and α = 20°

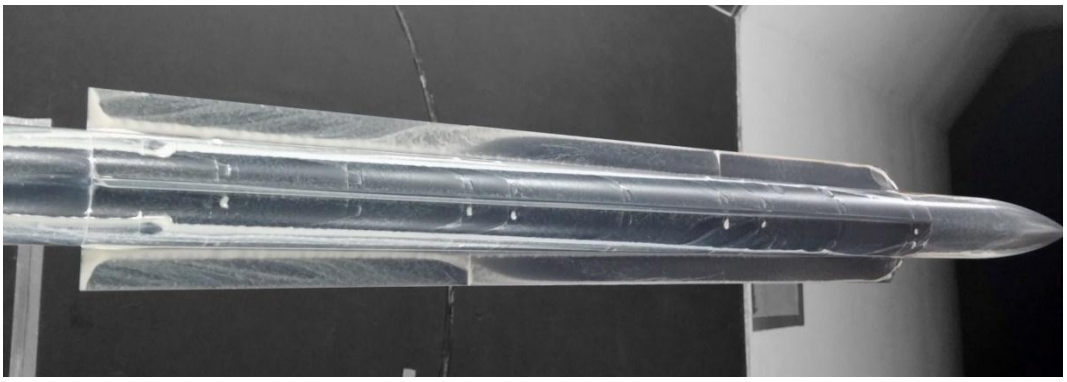

(a)

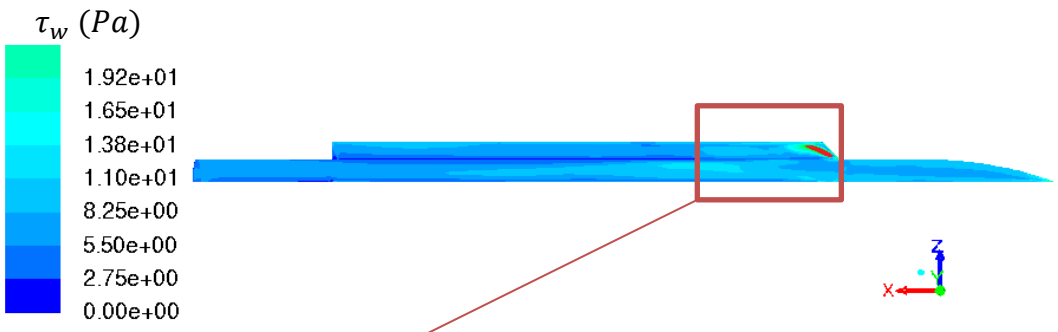

(b)

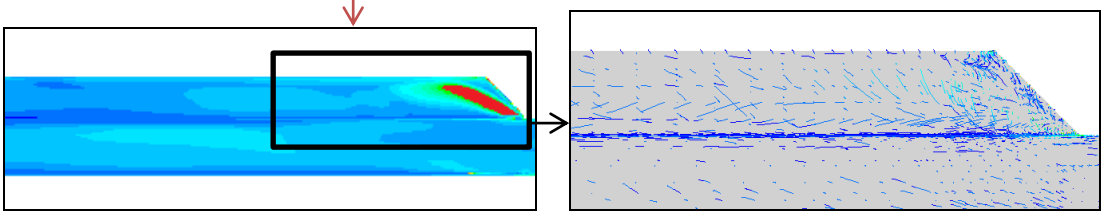

(c)

Figure 96: Top view comparison of (a) experimental surface flow and (b) CFD wall shear stress (Pa) with (c) CFD pathlines for s/D = 1.75 and α = 20°

Appendix C

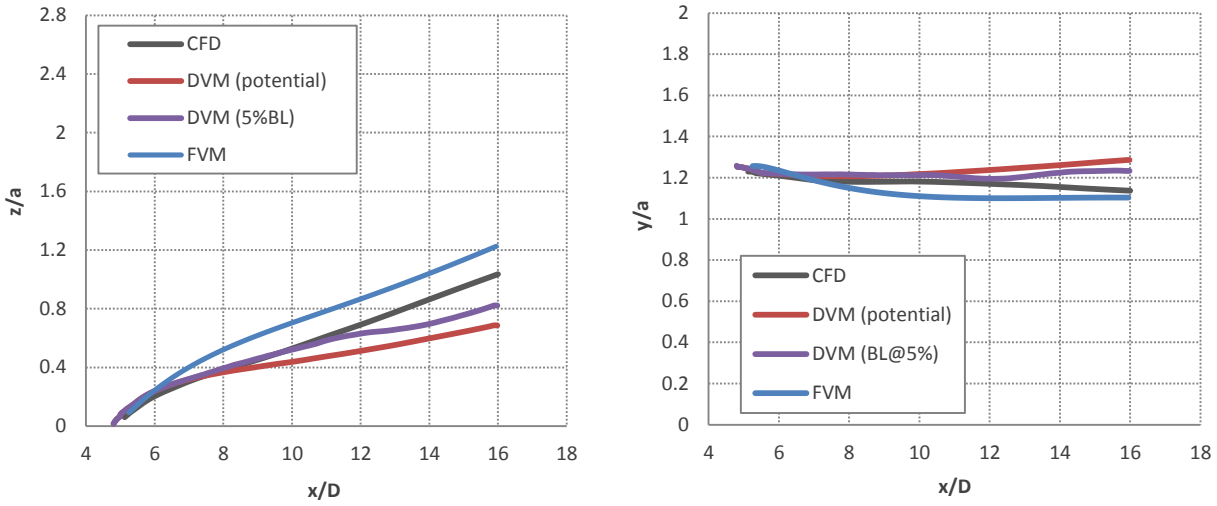

(a) (b)

Figure 97: (a) Vertical and (b) lateral vortex positions for α=6° and s/D=1.25

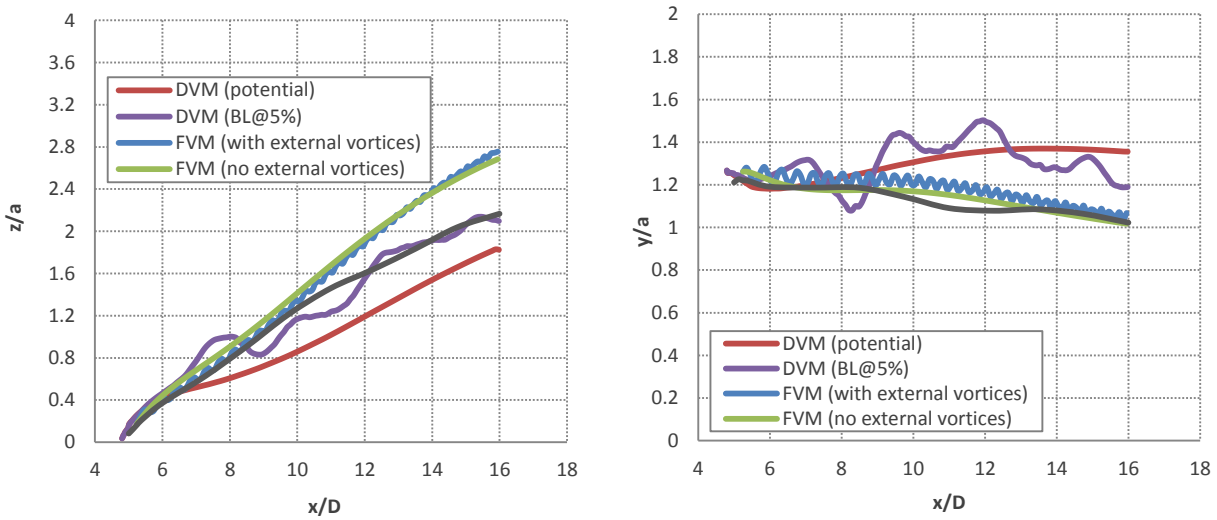

(a) (b)

Figure 98: (a) Vertical and (b) lateral vortex positions for α=15° and s/D=1.25

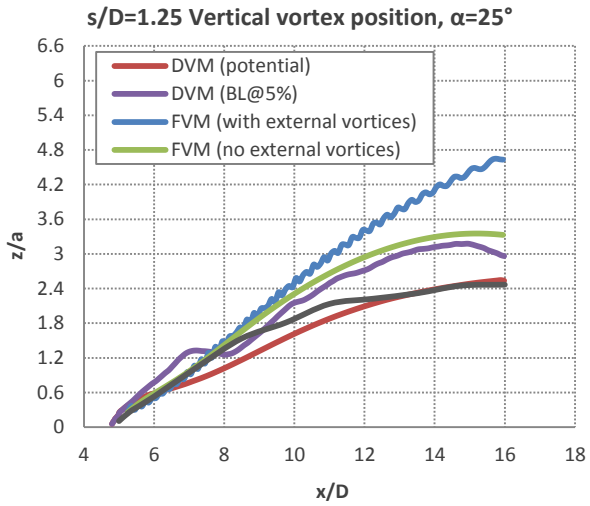

(a)

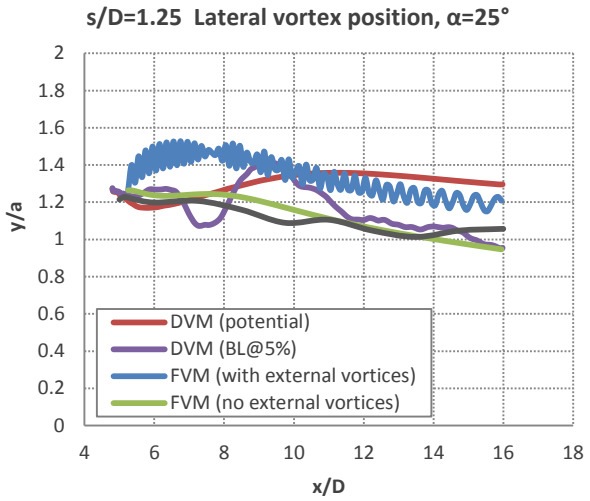

(b)

Figure 99: (a) Vertical and (b) lateral vortex positions for α=25° and s/D=1.25

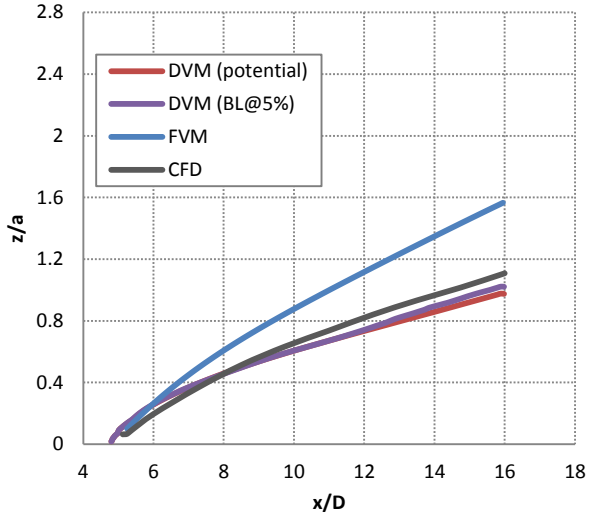

(a)

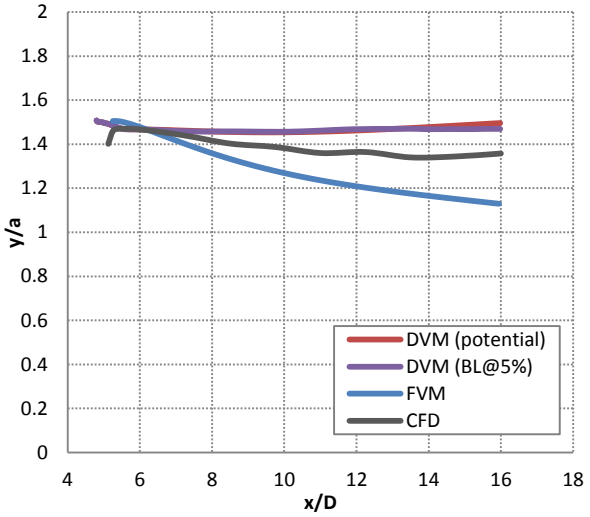

(b)

Figure 100: (a) Vertical and (b) lateral vortex positions for α=6° and s/D=1.5

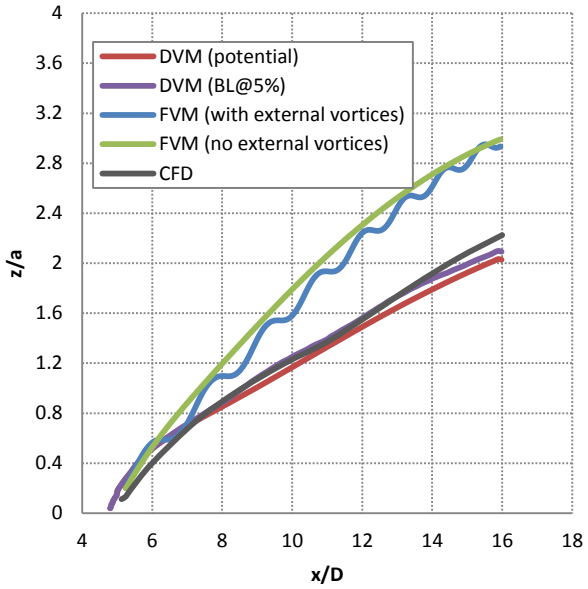

(a)

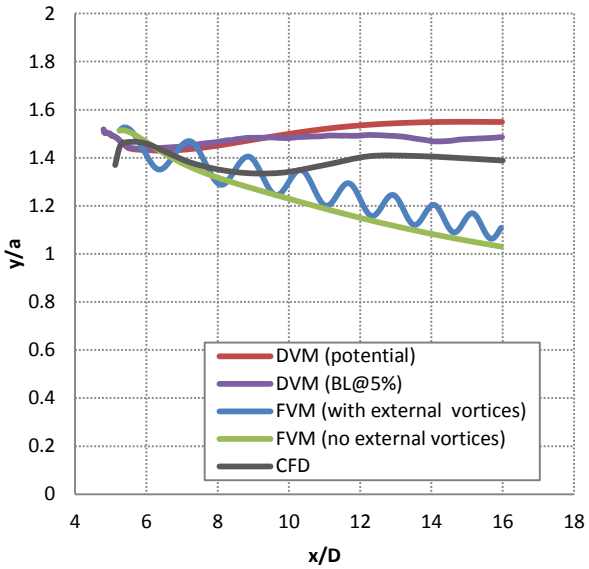

(b)

Figure 101: (a) Vertical and (b) lateral vortex positions for α=15° and s/D=1.5

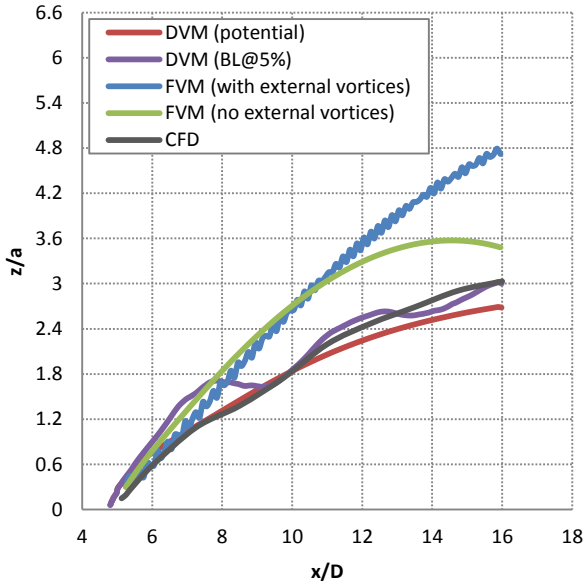

(a)

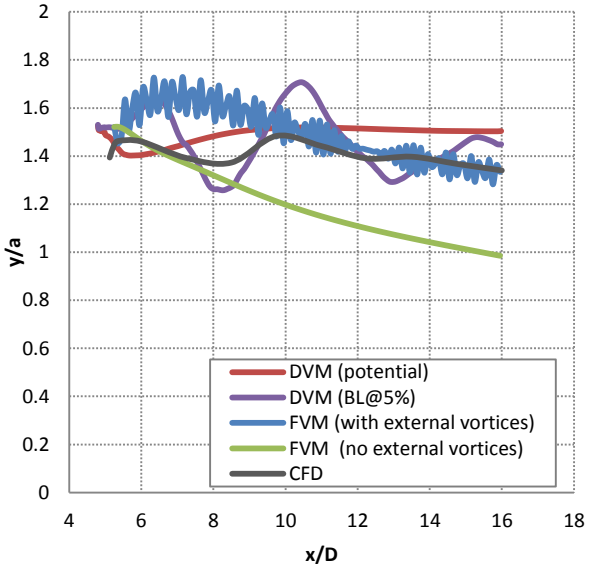

(b)

Figure 102: (a) Vertical and (b) lateral vortex positions for α=25° and s/D=1.5

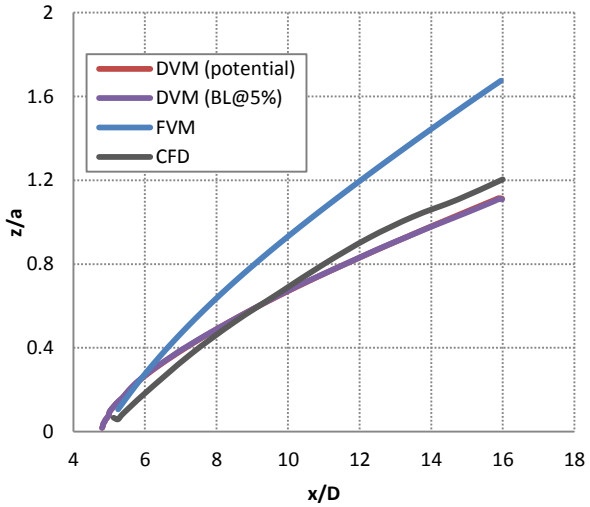

(a)

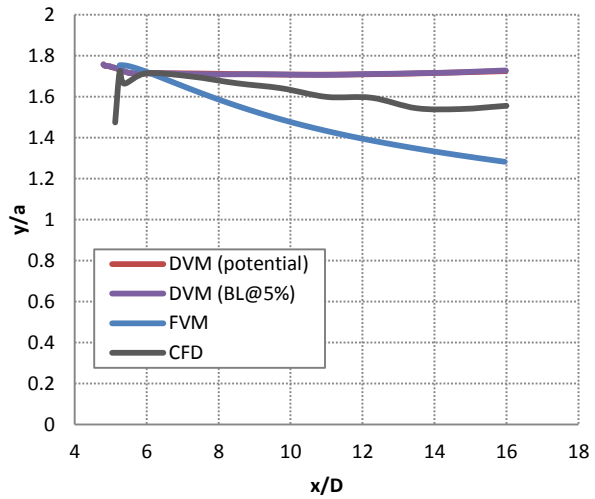

(b)

Figure 103: (a) Vertical and (b) lateral vortex positions for α=6° and s/D=1.75

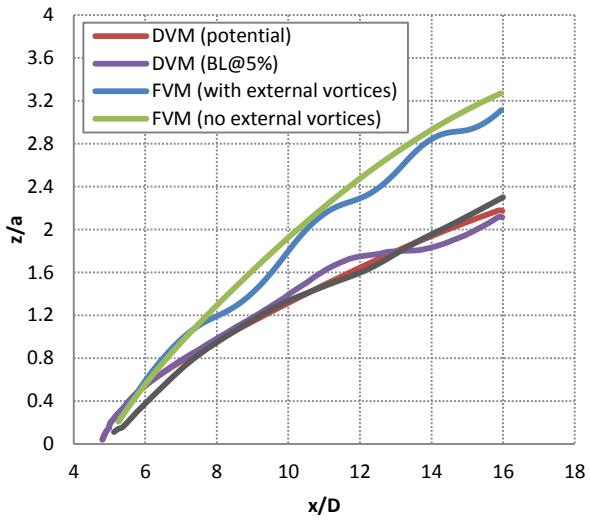

(a)

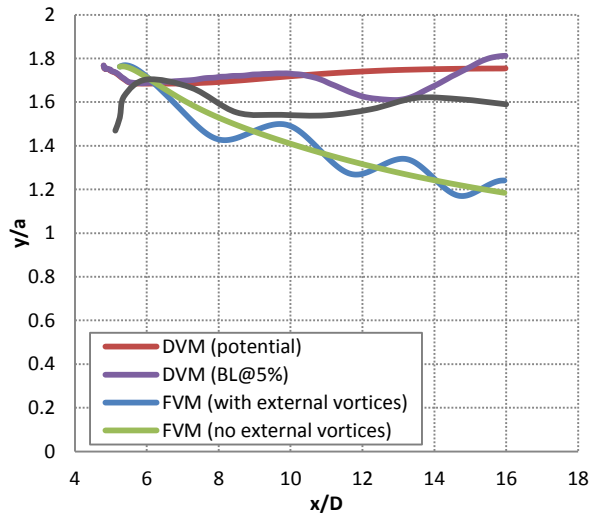

(b)

Figure 104: (a) Vertical and (b) lateral vortex positions for α=15° and s/D=1.75

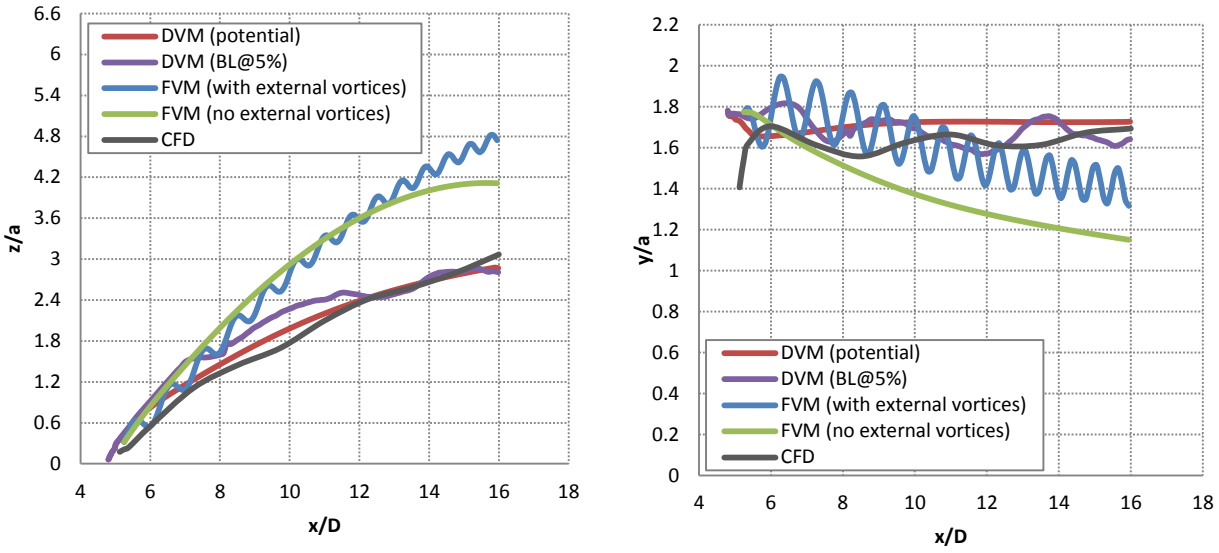

Figure 105: (a) Vertical and (b) lateral vortex positions for α=25° and s/D=1.75